2005

Electrodeposition of AuCo alloys and multilayers

Maoshi Guan
Louisiana State University and Agricultural and Mechanical College, mguan1@lsu.edu

ELECTRODEPOSITION OF AuCo ALLOYS AND MULTILAYERS

A Thesis

Submitted to the Graduate Faculty of the
Louisiana State University and
Agricultural and Mechanical College
in partial fulfillment of the
requirements for the degree of
Master of Science in Chemical Engineering

in

The Department of Chemical Engineering

By
Maoshi Guan
B.S., University of Petroleum (East China), 1999
May, 2005

To my dear family…

ACKNOWLEDGEMENTS

I would like to thank Dr. E. J. Podlaha for her insightful guidance, continued inspiration and support, and great patience throughout the duration of this project, which make this study possible.

Many thanks to Dr. A. B. Corripio and Dr. R. W. Pike to be my graduate committee.

I would like to thank Dr. X. Xie in Geology Department and Mr. V. Singh in CAMD for SEM analysis, Dr. D. P. Young and Dr. Moldovan in Physics Department for GMR analysis, Ms. C. Henk in Department of Biological Science for TEM analysis and Dr. J. Jiang in Mechanical Department for XPS analysis.

I would also acknowledgement my colleagues, Dr. Q. Huang (IBM), Mr. Y. Li, Ms. D. Davis, Mr. R. Mishra and all the other group members for their advice and assistance, and the peaceful environment they provided in the lab.

This work was financially supported by NIRT-NSF (#CTS-0210832).

TABLE OF CONTENTS

DEDICATION…… ii

ACKNOWLEDGEMENTS……..…... iii

LIST OF TABLES…….. vi

LIST OF FIGURES…… vii

ABSTRACT……...……. x

CHAPTER 1 INTRODUCTION…… 1
1.1 Introduction……... 1
1.2 Goal of Study…… 5

CHAPTER 2 LITERATURE REVIEW……..… 6
2.1 Basic Concepts of Electrodeposition ……... 6
2.2 Electrodeposition of Au/Co…….. 8
2.2.1 Single Bath/ Dual Bath ……..…. 8
2.2.2 Single Sulfite-Thiosulfate Electrolyte ……... 10
2.2.3 Electrodeposition of AuCo ……..… 11
2.3 Physical Mechanism of GMR …….. 14
2.4 MR of Au/Co System …….. 19
2.5 Nanolithography …….. 26

CHAPTER 3 EXPERIMENTAL ……... 28
3.1 Thin Films Electrodeposition ……..….. 28
3.1.1 Electrolyte ……..…….……. 28
3.1.2 Rotating Disk Electrode (RDE)…….. 29
3.1.3 Substrate Preparation…….. 30
3.1.4 Cell Set-up…….. 30
3.2 Nanowire Fabrication ……..…… 32
3.2.1 Electrolyte …….……..... 32
3.2.2 Working Electrodes ……..…….. 33
3.2.3 Cell Set-up…….. 35
3.3 Methods ……..……. 37
3.3.1 Polarization ……..……..…….. 37
3.3.2 Impedance Analysis ……..……..…… 38
3.3.3 Current Efficiency and Partial Current Density……. 38
3.3.4 Alloys and Multilayer Plating…….…… 39
3.4 Deposit Characterization ……..……..……... 40
3.4.1 XRF ……..……..…… 40
3.4.2 SEM…… 41

3.4.3 XPS…… 42
3.4.4 TEM…… 42
3.4.5 GMR…… 43

CHAPTER 4 RESULTS AND DISCUSSIONS……. 44
4.1 Au-Co Alloy Electrodeposition…… 44
4.1.1 Polarization Curves……. 44
4.1.2 Effects of Citric Acid…….. 46
4.1.3 Effects of Ph…… 50
4.2 Multilayer Thin Films Electrodeposition…….. 54
4.2.1 Electrodeposition Parameters……. 54
4.2.2 XPS……. 54
4.2.3 GMR…… 55
4.2.4 Nanoimprint Molds……. 58
4.3 Nanowires Electrodeposition ……..…….. 64
4.3.1 Au/Co Multilayer Nanowire - Galvanostatic Control……. 65
4.3.2 Au/Co Multilayer Nanowire - Potentiostatic Control……. 69
4.3.3 AuCo Alloy Nanotube…… 73

CHAPTER 5 CONCLUSIONS…… 76

REFERENCES…… 78

VITA…….…….. 85

LIST OF TABLES

Table 2-1 Standard Equilibrium Potentials (V vs. NHE)[35] 9

Table 3-1 Composition of AuCo bath for thin films plating 28

Table 3-2 Composition of AuCo bath for nanowire electroplating 32

Table 4-1 Composition of $K_2Cr_2O_7$ etching solution 60

Table 4-2 Coefficient of linear thermal expansion (CTE) 64

LIST OF FIGURES

Figure 2-1 Schematic of an electrochemical cell. 6

Figure 2-2 Schematic illustrations of kinetic and mass transport control 8

Figure 2-3 Schematic representation of the GMR effect. 16

Figure 2-4 Schematic illustration of electron transport in a multilayer for antiparallel (a) and parallel (b) magnetizations of the successive ferromagnetic layers.[56] .. 18

Figure 3-1 Schematic of the cell for thin film electrodeposition 31

Figure 3-2 Schematic, cross-sectional drawing of the recessed rotating disk electrode.. 33

Figure 3-3 The stagnant holder for nanowires electrodeposition 34

Figure 3-4 Nanowire growth procedure in AAO/polycarbonate membrane templates ... 35

Figure 3-5 Electroplating cell for recessed rotating disk electrode 36

Figure 3-6 Schematic cell for nanowires electrodeposition 37

Figure 3-7 Schematic of DC (top) and square-wave pulse (bottom) plating 40

Figure 3-8 Transverse MR measurement 43

Figure 4-1 AuCo polarization curve which shows the Au plateau, 1600 rpm 45

Figure 4-2 Au-Co polarization curves with different Au concentrations, 1600 rpm 45

Figure 4-3 Au concentration change in galvanostatic deposited alloys at different citric acid concentrations, 1600 rpm 47

Figure 4-4 Co concentration change in galvanostatic deposited alloys at different citric acid concentrations, 1600 rpm 47

Figure 4-5 Current efficiency of the DC plated alloys at different citric acid concentrations 48

Figure 4-6 Au and Co partial current densities at different citric acid concentrations 49

Figure 4-7 Side reaction partial current density at different citric acid concentrations ... 49

Figure 4-8 Au concentration change in galvanostatic deposited alloys at different pH values 51

Figure 4-9 Co concentration change in galvanostatic deposited alloys at different pH values 51

Figure 4-10 Current efficiency of the DC plated alloys at different pH levels..... 52

Figure 4-11 Au and Co partial current densities at different pH levels 53

Figure 4-12 Side reaction partial current density at different pH levels 53

Figure 4-13 Schematic of XPS analysis of Au/Co multilayer films 55

Figure 4-14 Schematic of GMR on Cu foil substate..... 56

Figure 4-15 GMR results of Au/Co multilayer films on Cu foil substrate, with variable Co layer thickness 57

Figure 4-16 GMR results of Au/Co multilayer films on Cu foil substrate, with variable Au layer thickness..... 57

Figure 4-17 GMR variation with layer thickness..... 58

Figure 4-18 Six steps of the nanoimprint mold preparation from the Au/Co multilayers electrodeposition and then selective etching of Co layers 60

Figure 4-19 Overview of cross-section multilayers on RDE after mounting, cutting, polishing and etching 61

Figure 4-20 SEM micrograph of a multilayer with constant Au layer of 200 nm and variable Co layer thicknesses of 200, 400, 600 and 800 nm..... 62

Figure 4-21 SEM micrograph of a multilayer with constant Au/Co layer thickness (Au 200 nm/Co 600nm) after etching for 5 minutes..... 62

Figure 4-22 SEM micrograph of the distortion of multilayer thin films 64

Figure 4-23 Polarization curve of Au-Co electrolyte (Table 3-2) 65

Figure 4-24 SEM micrograph of Au/Co multilayer nanowires at different angles 67

Figure 4-25 SEM micrograph reflects the irregular distribution of empty pore size of AAO membrane with pore size of 0.02 μm..... 68

Figure 4-26 Schematic illustration of bifurcating structures in AAO membrane..... 68

Figure 4-27 TEM bright field image of a multilayer structure 69

Figure 4-28 Polarization curve of Au-Co electrolyte (Table 3-2) 70

Figure 4-29 Au/Co multilayered nanowires fabricated by potentiostatic pulse plating .. 71

Figure 4-30 EDS spectra of Au/Co multilayered nanowires 72

Figure 4- 31 TEM bright field image of a nanowire..... 73

Figure 4- 32 SEM imagine of Au-rich alloy nanotubes..... 74

Figure 4- 33 A higher magnification of the Au-rich nanotube 74

ABSTRACT

Electrodeposited AuCo and Au/Co multilayers are of interest as potential materials for MEMS components. AuCo alloys have been fabricated by the electrodeposition technique, but from cyanide-containing electrolyte. In this study, we explored the electrodeposition of AuCo and Au/Co multilayer thin films, and nanowires, from a non-cyanide electrolyte. Two variables were considered: the concentration of citric acid and pH. The changes in composition were described by the differences in the partial current densities.

The effect of pH and citric acid concentration on the deposit composition and current efficiency was investigated. Results showed that a lower citric acid concentration was favored for multilayered Au/Co deposits with disparate compositions in each layer. At low current density elemental gold is deposited, while at high current density a cobalt rich alloy (98.7 % Co) is obtained. An increase in the citric acid concentration requires larger applied current density to achieve the same cobalt concentration. The influence of pH has a similar behavior. The lower the pH, the larger is the disparity between the compositions. The current efficiency drops with increasing citric acid concentration and pH. By comparing the partial current densities, both the side reaction and Co rates are influenced by the citric acid and pH.

Giant magnetoresistance (GMR) property was explored for Au/Co nanometric multilayers, and a large GMR (> -13 %) was found when the films were deposited on

(100) Cu. The GMR changes from a positive to negative value depending on the Au and Co layer thicknesses.

The application of the multilayered deposit to fabricate a nanomold was explored. The mold was fabricated by depositing the multilayer and selectively etching one layer.

Electrodeposition of Au/Co multilayer nanowires was also fabricated in this study. Both alumina oxide and polycarbonate membranes were used as templates. A nanowire of 15 nm for Co and 25 nm for Au, which is closed to the calculated layer size, was confirmed by TEM analysis.

CHAPTER 1 INTRODUCTION

1.1 Introduction

Electrodeposition refers to the reduction process taking place on a cathode surface in an electrolyte containing metal ions. The process has numerous applications in depositing thin films and deep recessed microstructures, for protective coatings, magnetic sensor and storage devices and as structures for micro-electro-mechanical systems (MEMS).

For example, electrodeposition of soft gold is widely used to fabricate X-ray masks for deep lithography electroforming[1] and plastic molding (LIGA) process.[2] Another application of electrodeposition of soft gold is in gold wafer bumping, which is the key process to the electronic packaging industry, especially where a high density of input/output (I/O) connections is required.[3] Electrodeposited AuCo alloy (so called hard gold), which has a hardness more than twice elemental Au and better wear resistance,[4] has been used extensively in the connector manufacturing industry. The same degree of hardness cannot be matched using other metallurgical methods.

Giant magnetoresistance (GMR) refers to the change in electrical resistance in response to an applied magnetic field. In multilayered systems, GMR is caused by the applied magnetic field changing the relative electron scattering of the magnetic layers, which has extensive industrial applications for hard disk read heads, bio-sensors, vehicle detection for traffic, and etc.[5] Magnetoresistance can also occur in an unlayered alloy films, nevertheless in most cases, with a much smaller value. The GMR multilayers are comprised of alternating nanometric layers of ferromagnetic materials (such as Co, Ni,

and Fe) and nonmagnetic materials (such as Au, Cu, and Cr). To date, several conventional techniques have been used to produce magnetic multilayers, including molecular beam epitaxy, electron-beam evaporation, ion-beam sputtering, and magnetron sputtering. Velu *et al.*[6] measured a CPP GMR of 3 % at 4.2 K for Co/Au sandwiches , which were fabricated by ultrahigh vacuum evaporation. Hutten *et al.*[7] reported an Au/Co granular structures with GMR of 2.4 % at 10 K, fabricated by a melt-spinning technique.

However, when depositing on irregular shape substrate or deep recesses, these methods have intrinsic limitation. In contrast, electrodeposition can fulfill this task cost effectively. However, few GMR results were reported for electrodeposited Au/Co structures, since most of the research effect has focused on the Cu/Co system.[8-11]

To exhibit GMR properties, the thickness of non-magnetic spacer layers has to be smaller than a critical length. In multilayer thin films, the spacer layer thickness has to be comparable to the electron mean free path (a few nanometers) to exhibit current-in-plane (CIP) GMR. In multilayer nanowires, the electron diffusion length (a few tens of nanometers) is the critical length for the exhibition of current-perpendicular-to-plane (CPP) GMR.[12] Compared with the current-in-plane GMR, current-perpendicular-to-plane GMR has been proven to show a larger magnetoresistance change in some systems.[13, 14] A variety of multilayer nanowires, including Co/Cu, Fe/Cu, and NiFe, have been fabricated by electrodeposition techniques with CPP GMR reported.[10, 15, 16] However, to the best of our knowledge there has been no electrodeposited Au/Co multilayer GMR reported. The closest study related to our goal is the one presented by Valizadeh *et al.*[17, 18] They electrodeposited Au/Co multilayer thin films and nanowires

onto polycarbonate membranes from a cyanide-containing electrolyte, but no GMR was reported.

In electrodeposition of multilayers, accurate control of a microstructure on the nanometric scale makes it possible to control not only magnetic properties but also mechanical properties. The multilayers with layer size of tens to hundreds of nanometers are of great interest in optics and electronics industries for nanolithography application.[19] Seekamp *et al.*[20] fabricated low refractive index passive optical devices with polymethylmethacrylate (PMMA) and polystyrene (PS) by using ultra violet nanoimprint lithography. Lim *et al.*[21] reported a one-dimensional grating mold on a sub-micron scale by the electrodeposition of NiCuFe/Cu multilayer. Currently electron-beam lithography is the most developed and widely used nanolithography, however, equipped with intrinsic problems of charging, wave diffraction, scattering limits and high operating cost. Due to the disparate compositions in each layer of Co/Au multilayers, electrodeposition and selective etching could be an efficient alternative way for nanomold fabrication, instead of electron-beam lithography.

Because of the feasibility of electrodeposition in irregular or deep recessed areas, template electroplating has been widely investigated for the fabrication of nanowires, which refers to a three-dimensional, wire type structure having a diameter of nanometer scale and enormous surface area. Due to their unique configuration of large aspect ratio, the GMR property can be easily measured in a perpendicular mode (CPP GMR).

Reported electrolytes for AuCo alloys or multilayers use the gold (I) cyanide complex as a main source of gold in the electroplating industry. The cathode reduction reaction follows:

$$[Au(CN)_2]^- + e^- \rightarrow Au + 2CN^- \qquad \textbf{Equation 1-1}$$

Due to the gold-cyanide complex, the equilibrium potential is shifted to -0.61 V (cyanide complex) from 1.71 V. Cyanide combines with many organic and inorganic compounds, and is extremely toxic to humans. Chronic (long-term) inhalation exposure of humans to cyanide results primarily in effects on the central nervous system (CNS). Other effects in humans include cardiovascular and respiratory effects, an enlarged thyroid gland, and irritation to the eyes and skin. From 1987 to 1993, according to the Toxics Release Inventory,[22] cyanide compound releases to land and water totaled about 1.5 million lbs. The major cyanide releases to water are discharges from metal finishing industries, iron and steel mills, and organic chemical industries.

In 1992, the regulation for cyanide became effective by the U. S. Environmental Protection Agency (EPA). Later in 1995, a more stringent cyanide limit was set: the Maximum Contaminant Level (MCL) for cyanide was set at 0.2 ppm because EPA believes, given present technology and resources, this is the lowest level to which water systems can reasonably be required to remove this contaminant should it occur in drinking water.[23] The drinking water standards and the regulations for ensuring such standards are met, are called National Primary Drinking Water Regulations. All public water supplies must abide by these regulations. These rigorous regulation are economically unfeasible for industry if they continue to use $KAu(CN)_2$ in gold plating.

In addition to the environmental issues there are several other shortcomings to the use of $[Au(CN)_2]^-$ which has stimulated this investigation and commercialization of other non-cyanide gold complexes in plating baths.[24] The stability of the gold cyanide complex causes the reduction potential to occur at very negative potentials resulting in

the co-deposition of hydrogen ions, which lowers the plating efficiency and makes the development of electroless plating baths difficult.[25] The use of gold cyanide baths often leads to the delamination of the resist from the seed layer.[26] This leads to gold deposition underneath the resist, which is highly undesirable in most applications. In contrast, sulfite-based baths exhibit better resist compatibility.[27, 28]

Due to the extreme toxicity of the cyanide compound, a sulfite-thiosulfate electrolyte can be a possible alternative for AuCo electrodeposition. Gold sulfite (I) is unstable at pH < 7 where sulfite protonates froming bisulfite;[29] Gold (I) thiosulfate complex is stable in weakly acidic solutions. Whereas, the mixed sulfite-thiosulfate ligand bath, when operated at a slightly acidic pH of 6.0 and at a mildly elevated temperature of 60 ^{o}C, it is highly stable and there is no need to add any stabilizer to suppress spontaneous decomposition.[30] Cobalt can be electrodeposited from all-sulfate solution, and which is often operated at slightly acidic condition.[31]

1.2 Goal of Study

Considering the environmental and technical concerns, in this study, we explore the electrodeposition of Au/Co alloy and multilayers from a single, thiosulfate-sulfite electrolyte. The cobalt concentration was kept in great excess of gold to obtain alloys rich in cobalt, and to make it possible to fabricate multilayers. In the Au-Co single, sulfite-thiosulfate electroplating system, the electrolyte stability, alloy compositions, current efficiencies and partial current densities are investigated systemically. Two types of nanometric materials will be investigated: one dimensional multilayer structures made of alternating thin layers of different composition, and two-dimensional wire/tube structures suspended within a three-dimensional matrix.

CHAPTER 2 LITERATURE REVIEW

2.1 Basic Concepts of Electrodeposition

Electroplating is the deposition of a metallic coating by applying a negative charge onto a substrate in an electrochemical cell. An electrochemical cell is schematically depicted in **Figure 2-1**. It consists of at least two electrodes (cathode and anode) where the electrochemical reactions occur, an electrolyte for conduction of ions, and an external conductor to provide for continuity of the circuit.

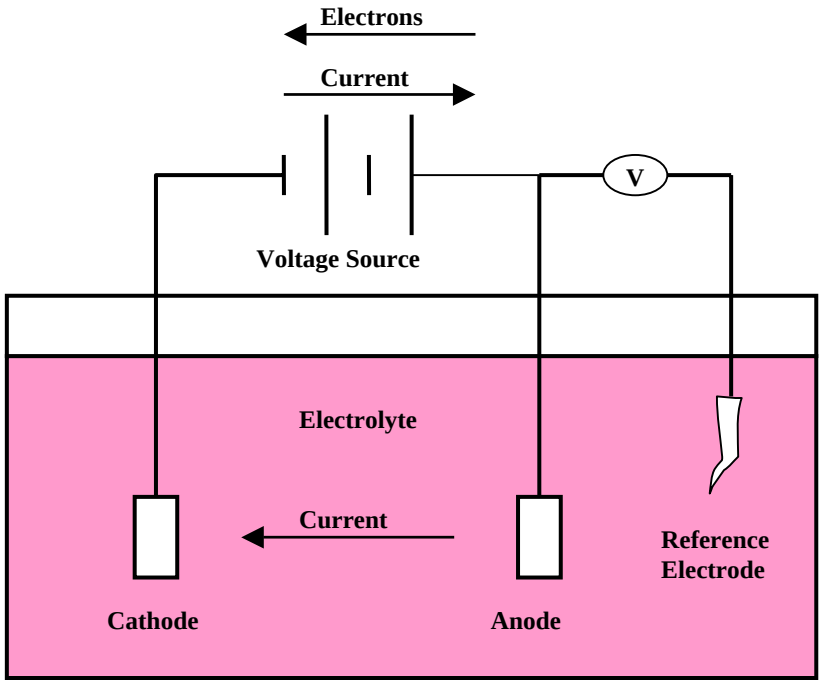

Figure 2-1 Schematic of an electrochemical cell.

During the deposition of AuCo the following cathodic reactions take place:

$Au (I) + e^- \rightarrow Au (s)$ **Equation 2-1**

$Co (II) + 2e^- \rightarrow Co (s)$ **Equation 2-2**

The anodic reactions are dependent on the anode materials chosen.

Faraday's law, shown in **Equation 2-3**, relates the amount of charge passed to the amount of substance oxidized or reduced, which can be used to calculate the thickness of deposited metal films in electrodeposition.

$$It\eta = nF\left[\frac{m}{sM}\right] \qquad \textbf{Equation 2-3}$$

where I is the applied current, t is the charging time, η is the current efficiency, n is the number of electrons transferred, F is the Faraday's constant (96485 C/equiv), m is the mass reacted, s is the stoichiometric coefficient and M is the molecular weight.

At large applied current or potentials the mass transport mechanism dominates and causes the current to reach a limiting value. **Figure 2-2** shows the current response to an applied potential at steady state for a single reactant. At a low applied potential, the reduction reaction is under kinetic control. The surface concentration is approximately equal to the bulk concentration, and the reduction rate is dependent on the applied potential in an exponential way. The system is under a mixed control of kinetic and mass transport when the overpotential becomes larger. The surface concentration becomes less than the bulk concentration, and a concentration gradient of metal ions appears on the electrode surface. Finally when the surface concentration drops to zero, the mass transport control becomes completely dominant and the concentration gradient reaches a maximum value. At this moment, a maximum current, referred to as the limiting current, is reached and the reaction rate reaches a maximum.

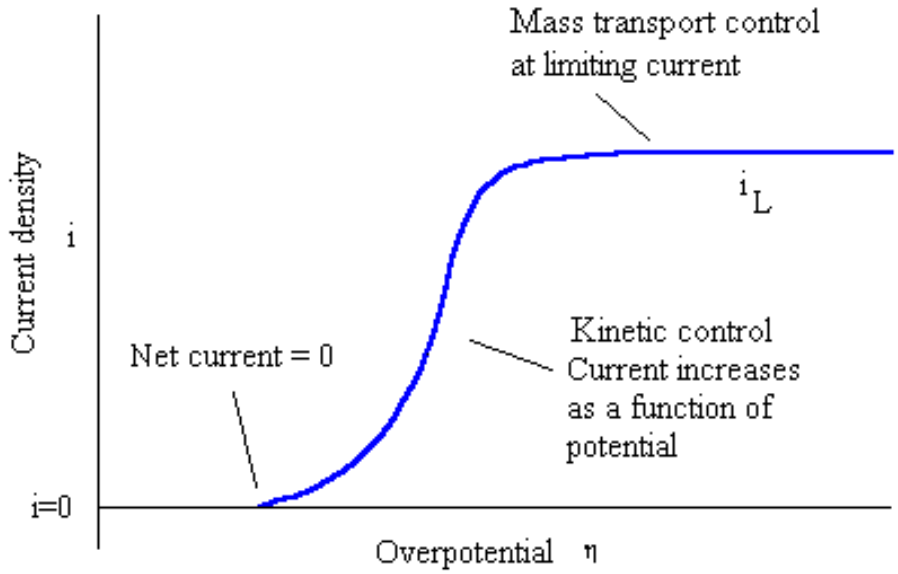

Figure 2-2 Schematic illustrations of kinetic and mass transport control

2.2 Electrodeposition of Au/Co

2.2.1 Single Bath/ Dual Bath

For the electrodeposition of multilayers, there are two general techniques: the dual bath and the single bath electrodeposition. Both processes can be controlled by modulating either the current density or the potential. In dual bath electrodeposition, the substrate is transferred to the first solution, plated and then rinsed and subsequently transferred to the second solution. This technique requires that the deposit is not exposed to the atmosphere to minimize contamination and corrosion at each sublayer surface. In 1939, Brenner[32] first employed two separate baths for the two components of the multilayer and periodically immersed the deposit into the two baths to electrodeposit composition-modulated films. However this technique proved to be too cumbersome to be adopted in practice.

In single bath electrodeposition, individual layers are electrodeposited from only one electrolyte solution containing two or more different metal ions forming the multilayer structure. The advantage of a single bath plating over a dual bath is that the substrate always remains under the electrolyte, thus lowering the risk of contamination. This method was first tried using the Cu-Ni system to produce composition-modulated alloys by electrodeposition in 1986 by Yahalom and Zadok.[33] The single bath plating is suitable for a considerable number of metal couples. The main caveat, however, is that both metals need to be deposited from similar baths. Another is that they differ sufficiently in their degree of nobility;[34] the reduction potential of the components must be far enough apart to allow a separate electrodeposition of the components.

Au is a noble metal, with a very positive standard reversible potential and thus reduction is favored. **Table 2-1** shows the standard reversible potentials (E^0) of the reduction of the two elements and the possible side reactions that can happen in this

Table 2-1 Standard Equilibrium Potentials (V vs. NHE)[35]

	Electrochemical Reaction	**Standard equilibrium Potential (V vs. NHE)**
More Noble ↑	$Au^+ + e^- = Au$	1.692
	$O_2 + 4\ H^+ + 4\ e^- = 2\ H_2O$	1.229
	$2\ H^+ + 2\ e^- = H_2$	0.000
	$Co^{2+} + 2\ e^- = Co$	-0.277
	$2\ H_2O + 2\ e^- = H_2 + 2OH^-$	-0.828

study. If the concentration of Au is comparable to Co, when current is passed, Au would be deposited for similar kinetic reaction rates of all metal ions. To overcome this problem,

the concentration of Au is nearly one thousand times lower than the concentration of Co. Consequently, pure Au is deposited at lower current density, whereas a Co-rich alloy is deposited at a high current density due to the mass transport limitation of the Au deposition. To date, few studies for Au-Co single bath electrodeposition has been reported.

2.2.2 Single Sulfite-Thiosulfate Electrolyte

In the electrodeposition of Au, the conventional cyanide bath has been extensively studied and the detailed information on various aspects of the process has been described in the literature.[36] Due to the extreme toxicity of the cyanide compound, a sulfite-thiosulfate Au electrolyte was examined as a possible alternative.

The gold sulfite complex is commonly used to prepare non-cyanide baths because of the ability to produce smooth, bright and ductile pure gold deposits with good microthrowing power. In the sulfite baths, gold exist in the form of $[Au(SO_3)_2]^{3-}$, with an approximate stability constant of 10^{10},[37] which is orders of magnitude smaller than that of the cyanide complex, $[Au(CN)_2]^-$, ie 10^{39}. Because of this reason, the sulfite complex tends to easily decompose and precipitate in the form of metallic gold, **Equation 2-4.** Special stabilizing additives are always added in commercially available sulfite baths to suppress the bath instability.

$$2\,Au^+ \rightarrow Au\,(0) + Au^{3+} \qquad \textbf{Equation 2-4}$$

The thiosulfate bath, $[Au(S_2O_3)_2]^{3-}$, is another type of gold complex with a stability constant of 10^{26},[38] which is substantially greater than that of the sulfite complex (10^{10}). Due to the higher stability constant, the thiosulfate bath might have been widely used in

gold plating, but actually it was not. The disadvantage of thiosulfate ion is that it easily liberates elemental sulfur from the following reaction, shown in **Equation 2-5**:

$$S_2O_3^{2-} \leftrightarrow S + SO_3^{2-} \qquad \textbf{Equation 2-5}$$

Due to the insufficient stability, the non-cyanide baths described above containing either sulfite or thiosulfate as a sole complexing agent appears to be of limited use. In 1991, H. Shindo *et al.*[39] found that the stability of the sulfite bath can be improved by adding sodium thiosulfate as the second complexing agent. Therefore, considering the pros and cons of sulfite baths and thiosulfate baths, a mixed ligand bath was investigated in this study. The Techni ® Gold 25E RTU solution was employed, in which sulfite gold complex is more concentrated than the thiosulfate gold complex.

In the Au-Co electrochemical system, citric acid ($C_6H_8O_4 \cdot H_2O$) is an often-used additive. The main purposes are: (1) help maintain the pH at the electrode surface and (2) prevent precipitation of metal salts. Solutions based on complex compounds tend to yield fine-grained deposits, which normally don't exhibit texture.[40]

2.2.3 Electrodeposition of AuCo

To date, there are few reports concerning the electrodeposition of Au/Co multilayers, and none from a non-cyanide-containing electrolyte. Valizadeh *et al.*[18] studied the electrodeposition of compositionally modulated AuCo alloy layers from a single bath with a citrate acid, cobalt sulphate and gold cyanide electrolyte. The Au content in the Co layers and Co content in the Au layers was found to be 3 and 0.1 wt. % respectively. The interfacial roughness was about 1.5 nm for a coating with a bilayer thickness of about 10 nm. The Co layers showed an estimated grain size of 2 nm.

Valizadeh *et al.*[17] also investigated the electrodeposition of Au/Co multilayered nanowires into 20 μm-thick ion track etched polycarbonate membranes with pore diameters of 110 – 150 nm from a single electrolyte. The Co-rich metallic nanowires were deposited at -1100 mV and the Au nanowires at -49 mV vs. Ag/AgCl. The magnetic measurements of 12 nm Co/4 nm Au nanowires for fields applied parallel and perpendicular to the film plane indicated a low remnant magnetization.

Valizadeh *et al.*[41] also studied the electrodeposition of Ag/Co multilayered nanowires in polycarbonate membranes (20 μm thickness and 120 nm pore diameter) using a single bath containing cobalt sulphate, silver cyanide and potassium pyrophosphate. Hydrogen evolution or initial layer re-dissolution of Co during Ag deposition occurred and a current efficiency of 58 % was determined for pulsed plating of Co. Multilayered nanowires with 8 nm Ag/ 15 nm Co layers were well defined as observed by TEM. The Ag/Co multilayered nanowire electrodeposition conditions were based on another study of Co-Ag composition-modulated alloys electrodeposition by Valizadeh *et al.*,[42] in which study, pure Ag can be deposited at current densities below 1 mA/cm^2, and 97 % pure Co can be obtained at a current densities of 40 mA/cm^2.

Cagnon *et al.*[43] investigated the anion effects on the structure and magnetic behavior of electrodeposited Co/Au (111) layers from different $CoSO_4$ solutions with anions of Cl^- and SCN^- added in amount traces. Results revealed that the anion had a strong influence and the growth was 2-d in the Cl solution and 3-D in the SCN solution. Perpendicular magnetization anisotropy (PMA) was observed in both solutions. In another study, Cagnon *et al.*[44] found that Cu/Co/Au (111) layers, electrodeposited from a sulfate plus

chloride solution, exhibit enhanced PMA due to the magnetoelastic effects at the Co/Au interface.

Kleinert *et al.*[45] carried out an in situ study of Co deposition on Au (111) and Au (100) electrodes. Their study focused on the initial stages of Co deposition and the nucleation behavior at surface defects such as monoatomic high steps. In both cases, the three-dimensional growth of Co clusters of undefined shape is observed. Once the Co deposition starts, the growth is very fast and hydrogen evolution takes place at the electrodeposited Co, which often disturbs imaging. Furthermore, the hydrogen bubbles reaching the Pt reference electrode lead to a shift of the reference potential.

Gundel *et al.*[46] characterized in-situ and in real time the magnetic state of electrodeposited ultrathin Co, Ni and Fe/Au (111) layers. The magnetization is out-of-plane at the Co/Au (111) and Fe/Au (111) interfaces below a critical thickness of few monolayers (MLs). For Co/Au (111) interfaces, the magnetization (M) is strictly out-of-plane for a cobalt thickness smaller than 1-2 MLs. The magnetization is then completely in the plane of the cobalt when the cobalt thickness is above 2 ML.

Kelly *et al.*[47] studied the effects of current density and an arsenic additive on the gold microstructure and residual stress from unsparged solutions of Technigold 25E with a pH of 6.5. It was found that the addition of arsenic (ppm) did not appreciably change the film grain size but did lower the twin density and modify texture. Films produced without and with arsenic had tensile and compressive stress, respectively. Pores were observed in all the gold films, but were larger and less concentrated for films produced with arsenic. For the case of direct current with arsenic, the pores were concentrated at the grain boundaries.

The properties of the metallic and organic phases in the gold plating play an important role in the mechanical behavior of these platings.[48] The study of the magnetic properties of AuCo platings has been very helpful in analyzing their structure. Magnetic force measurements are especially useful in separating the effects of the metallic and organic phases in the electroplating with a minimum of wet chemistry. Kahn[49] studied the magnetic properties and structure of cobalt-hardened gold electrodeposited from a cyanide-containing solution. After being annealed in hydrogen at 800 ^{o}C to destroy any cobalt compounds in the platings, the magnetic measurements revealed that only one phase exists, i.e. a solid solution of cobalt in gold. This phase showed superparamagnetic behavior with some remanence and is a magnetic nanocomposite.

2.3 Physical Mechanism of GMR

Giant magnetoresistance (GMR) was first discovered in 1988 by Baibich *et al.*[50] in Paris and Binasch *et al.* in Jülich. Like other magnetoresistive effects, GMR is the change in electrical resistance in response to an applied magnetic field. It was found that the application of a magnetic field to a single crystalline (100)-oriented FeCrFe multilayer resulted in a significant reduction of the electrical resistance of the multilayer. This effect was found to be much larger than either ordinary or anisotropic magnetoresistance and was, therefore, called "giant magnetoresistance" or GMR. These films were prepared by molecular beam epitaxy (MBE), which is a sophisticated and expensive ultra-high vacuum deposition technique ($\Delta R/R$=50 % at 4.2 K under a magnetic field of 5 Tesla).

Within a decade of GMR being discovered, GMR has generated a lot of interest among academic and industrial laboratories, commercial devices based on this phenomenon, such as hard-disk read-heads, magnetic field sensors and magnetic memory

chips had become available in the market. To date, various structures which display GMR have been found, such as superlattice multilayers,[16] granular materials, [51, 52] spin valve structures with asymmetric magnetic layers, spin valves with an exchanged-biased layer, current perpendicular to plane pillars. Values of GMR vary in a great range, depending on the material and temperature.[53] But, GMR is most usually seen in magnetic multilayered structures, where two ferromagnetic layers are closely separated by a thin nonmagnetic spacer layer a few nm thick.

GMR is distinguished from both ordinary magnetoresistance and anisotropic magnetoresistance (AMR), which are also present in layered and granular magnetic systems. Ordinary magnetoresistance arises from the effect of the Lorentz force on the electron trajectories due to the applied magnetic field. In contrast to GMR, it does not saturate at the saturation magnetic field and is usually small in metals[54] (less than 1 % in fields of the order of 1 Tesla). AMR originates from the spin-orbit interaction and causes the resistance to depend on the relative orientations of the magnetization and the electric current. The magnetic field range in which the AMR effect occurs is governed by the field needed to change the direction of the magnetic moment.

Figure 2-3 shows a Cu/Co multilayer system schematically, including: (a) change in the resistance of the magnetic multilayer as a function of applied magnetic field, (b) the magnetization configurations of the multilayer at various magnetic fields and, (c) the magnetization curve for the multilayer. In absence of the magnetic field, the internal magnetic (M) vectors of the neighboring ferromagnetic layers are aligned in an anti-parallel manner through the nonmagnetic interlayer by a quantum effect, which is the exchange coupling effect. When applying an external magnetic field, it aligns the

magnetic moments in a parallel way, saturates the magnetization of the multilayer and then leads to a drop in the electrical resistance of the multilayer.

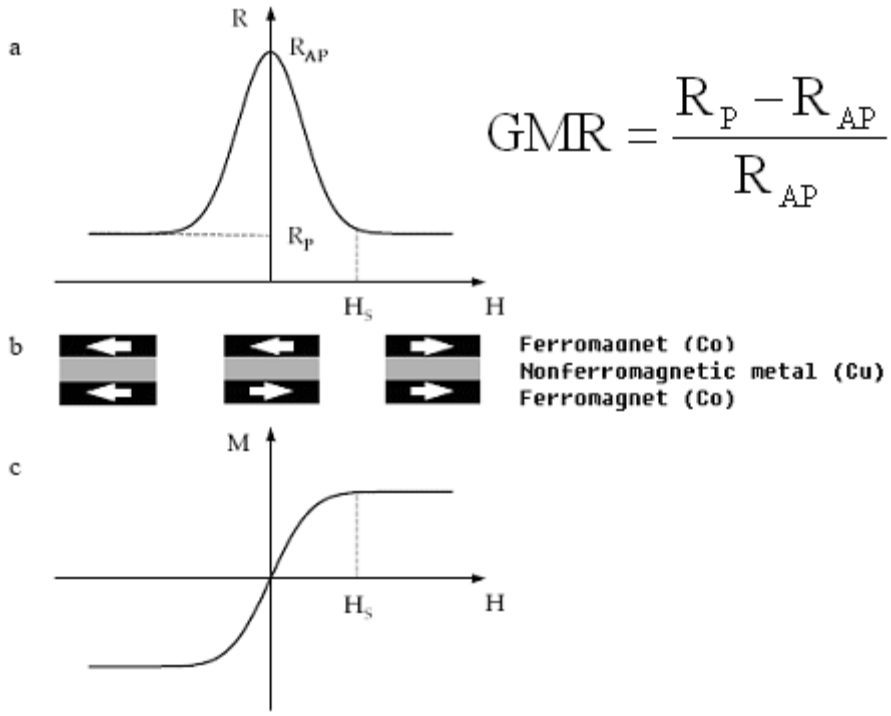

Figure 2-3 Schematic representation of the GMR effect.

Mott's model[55] of the electrical conduction in ferromagnetic metals can be used to describe the governing features of GMR. First the electrical current in ferromagnetic metals is carried independently in two conduction channels that correspond predominately to the spin-up and spin-down s-p electrons. The up-spin and down-spin electrons do not mix over long distances and, consequently, the electrical conduction occurs in parallel for the two spin channels. Secondly, whatever the nature of the scattering centers, the scattering rates of the up-spin and down-spin electrons are quite different due to the fact that the scattering rates are spin-dependent. Therefore, the conductivity can be significantly different in the two channels.

For the parallel-aligned magnetic layers (the top panel in **Figure 2-4-a**), the up-spin electrons pass through the structure almost without scattering, because their spin is parallel to the magnetization of the layers. On the contrary, the down-spin electrons are scattered strongly within both ferromagnetic layers, because their spin is antiparallel to the magnetization of the layers. Since conduction occurs in parallel for the two spin channels, the total resistivity of the multilayer is determined mainly by the highly-conductive up-spin electrons and appears to be low. For the antiparallel-aligned multilayer (the top panel in **Figure 2-4-b**), both the up-spin and down-spin electrons are scattered strongly within one of the ferromagnetic layers, because within the one of the layers the spin is antiparallel to the magnetization direction. Therefore, in this case the total resistivity of the multilayer is high.[56]

Now we consider the two-current series resistor model by using Mott's theory. It is assumed that the scattering is strong for electrons with spin antiparallel to the magnetization direction, and is weak for electrons with spin parallel to the magnetization direction. Also the mean free path is much longer than the layer thicknesses and the net electric current flows in the plane of the layers. In absence of external magnetic field, neighboring ferromagnetic layers are aligned in an antiparallel manner (**Figure 2-4-a)**, both the up-spin and downspin electrons are scattered strongly within one of the ferromagnetic layers. Since conduction occurs in parallel for the two spin channels, the total resistivity of the multilayer is high. When applying external magnetic field, the neighboring ferromagnetic layers are aligned in a parallel manner (**Figure 2-4-b)**. The up-spin electrons pass through the structure almost without scattering, because their spin is parallel to the magnetization of the layers. On the contrary, the down-spin electrons are

scattered strongly within both ferromagnetic layers since their spin is antiparallel to the magnetization of the layers. Therefore, the total resistivity of the multilayer appears to be low.

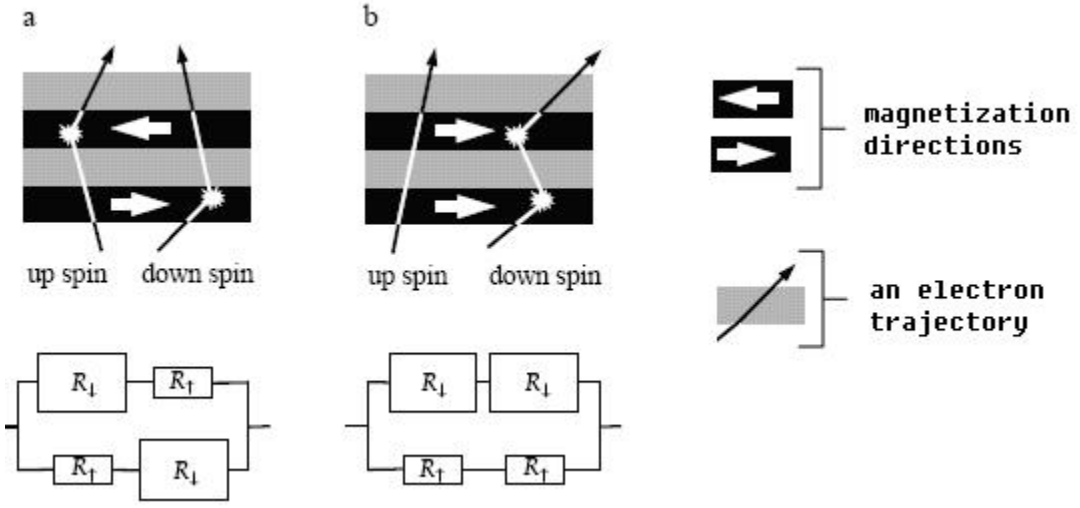

Figure 2-4 Schematic illustration of electron transport in a multilayer for antiparallel (a) and parallel (b) magnetizations of the successive ferromagnetic layers.[56]

According to different geometries in measurement, GMR can be listed into two categories: current-in-the-plane (CIP) geometry and current-perpendicular-to-the-plane (CPP) geometry. The current-in-the-plane CIP geometry is currently widely used in thin film structures in industrial application. While, measuring the current perpendicular to the multilayer plane is very difficult due to the very small thickness of the multilayer and consequently the very low resistance, which is difficult to detect. However, CPP is very attractive because its magnitude is higher than the corresponding magnitude of CIP GMR. One way to engineer the CPP mode is to use nanowires. As an example, electrodeposited multilayered nanowires grown within a polycarbonate membrane constitute a new medium in which GMR perpendicular to the plane of the multilayers can be measured. A CPP GMR of at least 22 % at ambient temperature has been reported.[57]

2.4 MR of Au/Co System

For the last few years, a large number of studies have been devoted to ferromagnetic metallic layers which have been widely used as components of thin films, sandwiches and multilayer structures. Many new magnetic properties have emerged from these materials: large perpendicular anisotropy, giant magnetoresistance effect due to the spin-valve effect,[58] oscillation in the coupling between two ferromagnetic layers through a non-magnetic spacer layer. In the scope of these features, Au/Co multilayers, fabricated by different methods on different substrates,[59] have already attracted much interest.

GMR effects not only occur due to a multilayer structure, but also could occur in the metal/metal granular systems. As Baibich *et al.*[50] reported, the alloy particles with GMR should consist of ferromagnetic single domain particles embedded in a nonmagnetic well-conducting matrix in order to substitute the role of the ferromagnetic layers in multilayered systems. As long as the particle size as well as the interparticle distance of these ferromagnetic particles is less than or comparable to the electron mean free path, a large magnetoresistance was anticipated due to the same spin-dependent scattering mechanism, which was already established for multilayers.

Hutten *et al.*[7] investigated the giant magnetoresistance and magnetic properties in AuCo granular structures. The melt-spun $Au_{71.6}Co_{28.4}$ ribbons were prepared from high purity elements using the melt-spinning technique. The highest GMR effect amplitude $\Delta R/R$ was reported to be 2.4 % at 10 K and decreases to about 1 % at room temperature. At relatively low fields, the MR rapidly decreased with increasing external field starting from zero field up to about 0.5 T. This high field dependence of metal/metal granular

systems was originated from small ferromagnetic clusters (Co) distributed within the nonmagnetic well-conducting matrix phase (Au).

Velu *et al.*[6] reported the magnetoresistance (MR) effects of perpendicular magnetic Co/Au sandwiches, which was fabricated by ultrahigh vacuum evaporation on a glass substrate with very small surface roughness; the maximum resistivity appeared at the coercive field H_c of a few 10^2 G and the MR ratio was about 3 % at 4.2 K. They discussed a mechanism for the magnetoresistance and suggested that the GMR occurs by spin-dependent scattering around or in the magnetic domain walls. A similar mechanism was proposed by Takahata *et al.*[60] for perpendicular magnetic Co/Au multilayers. Vavra *et al.*[61] proposed a different mechanism for the magnetoresistance for Co/Au, in which magnetoresistance occurred owing to the change in the number of adjacent layers with antiparallel magnetic moments.

Honda *et al.*[62, 63] studied the Co/Au multilayers which were prepared on glass substrate by the electron-beam evaporation technique. The perpendicular anisotropy was induced when the Co layer thickness was less than 12 Å. They found that perpendicular magnetic Co/Au multilayers exhibiting stripe domains show large GMR which consists of two components: one shown hysteresis related to the magnetic wall motion and the other decreases gradually with field for higher magnetic fields.

Later, Honda *et al.*[64] reported that in the perpendicular magnetic multilayers, the stripe magnetic domains were observed at zero field, indicating that each layer was demagnetized by multidomains. These films exhibited GMR consisting of hysteretic and nonhysteretic components. It was suggested that the former arose from antiparallel spin alignment between the adjacent Co layers due to the random wall position layer by layer,

and the later is related to the granular-type GMR. The MR ratio of the hysteretic component increased up to 20 % at 4.2K from the negligibly small value at room temperature. This temperature dependence is similar to that for the perpendicular giant magnetoresistance of multilayer Co/Cu nanowires.[65]

Beauvillain *et al.*[66] studied the variation of the magnetoresistance (MR) with temperature (T) in the He-4 temperature range (1.3 – 4.2 K) and at 300 K in $Au/Co_1/Au/Co_2/Au$ thin-film structures. The variation of the cobalt film's coercivity with thickness was quite different at low and high temperature. Based on the previous study of Beauvillain *et al.*[66], Velu *et al.*[67] extended the measurement of the magnetoresistance (MR) with temperature (T) to a larger temperature range (1.3 – 300 K) in dissymmetric structures $Au/Co_1/Au/Co_2/Au$ where Co_1 and Co_2 are two ultra thin Co films with different thicknesses. The results shows that the coercive field decreases when increasing the temperature and the decrease is more pronounced for the thinnest films. The variation of the coercive fields Hc_1 and Hc_2 versus T exhibits a crossover leading to a reduction by a factor one-half of the MR at the same temperature. At the low temperature of 1.4 K, the MR ratios for Au/Co (0.66 nm)/Au (5 nm)/Co (0.34 nm)/Au and Au/Co (0.2 nm)/Au (4.7 nm)/Co (0.6 nm)/Au were 5.3 % and 5.7 % respectively.

Kolb *et al.*[68] studied Au (111)/Co/Au simple trilayers on glass in the very low Co thickness limit by MBE. The deposition of less than 2 atomic layers of cobalt leads to discontinuous magnetic layer and the structure can be considered as a two dimensional granular system, where the magnetic domains are limited by the Co island's lateral sizes. At a temperature of 1.4 K, the existence of a large coercivity deduced from MR

measurement in perpendicular applied field shows the magnetization remains perpendicular to the film plane, even for a Co thickness as low as 0.2 atomic layer.

Kolb *et al.*[69] also fabricated granular multilayers with many periods by MBE in order to increase the signal from both magnetization and MR measurements. The magnetoresistance increases as each new Co layer is added. The increase was larger when the resulting multilayer had an odd number of layers; this behavior can be explained by a Camley-Barnas model calculation.[70] At 300 K, the MR is only less than 2 % at high fields up to 10 T.

Barnas *et al.*[70] carried out theoretical and experimental studies on novel magnetoresistance effects in Fe/Cr and Au/Co multilayers. They fabricated Co/Au/Co double layers on GaAs, with the Au interlayers were thick enough to avoid exchange coupling between the Co films. Only at sufficiently high magnetic fields, the magnetic alignments of both ferromagnetic films change from antiparallel to parallel. In the same study, they concluded, that for magnetoresistivity in Co/Au/Co structures, the antiparallel alignment was achieved by different coercive fields of the Co films and not by an antiferromagnetic exchange coupling between the ferromagnetic films, as in the case of the Fe/Cr layered structures.

Araki *et al.*[71] measured the magnetic and magnetoresistive properties of Au/Co artificial superstructured films prepared by an alternate deposition technique in ultra high vacuum. A large perpendicular anisotropy was found when the Co layers were thinner than 20 Å. The maximum change of resistivity is about 4 % at 77 K.

For the Au/Co multilayers deposited by sputtering techniques as well as molecular beam epitaxy (MBE), the structure of the deposits is always the cfc (111) Au/cp (0001)

co epitaxial relationship. Chappert and Bruno[72] reported that the easy magnetization axis was perpendicular to the surface when the Co thickness does not exceed 1.1 nm. The magnetoresistance ratio is then larger than that obtained with thicker films, when the magnetization lies in plane. Hamberod *et al.*[73] presented a new single crystal bct Co (100)/Au (100) multilayered structure grown on MgO (100) substrates. Unlike the Co (1000)/Au (111) structure, no perpendicular anisotropy is observed. The 2 monolayer (ML) Co multilayer exhibits superparamagnetic behavior and the 4 ML Co multilayer shows two magnetic contributions: superparamagnetic and ferromagnetic.

Pizzini *et al.*[74] studied the Co structure in Cu/Co and Au/Co multilayers. The Cu/Co and Au/Co multilayers were fabricated by thermal evaporation from tungsten crucible in an ultrahigh vacuum chamber. The interface roughness was less than 4 Å for Cu/Co multilayers and about 6 Å for Au/Co multilayers. The Cu/Co multilayers were able to accommodate the small lattice mismatch (2 %) between Co and Cu without inducing a large disorder. For Au/Co multilayers, the lattice was not able to accommodate the large mismatch (14 %) between Co and Au and resulted in the creation of defects.

Casanove *et al.*[75] reported the fine structure and magneto-optical properties of Au/Co multilayers epitaxially grown on MoS_2 substrates. Only the Co films deposited at 300 K presented well-defined layers and exhibited a strong magnetic anisotropy, despite the presence of some interface roughness. The epitaxial growth of Co on Au was thought to enhance the magneto-elastic component of the magnetic anisotropy.

Oscillation of magnetoresistance as the thickness of the nonferromagnetic spacer layers between the ferromagnetic layers increases is a signature of GMR. The oscillating GMR depends on the nature of the magnetic metal and on the growth direction of the

multilayer. Based on experimentally determined Fermi surfaces of the bulk metals, quantitative prediction can be made for noble metal spacer layers. The oscillation period was is typically about 1 nm. The magnetic coupling was shown to oscillate between antiferromagnetic and ferromagnetic so that the magnetic moment of successive ferromagnetic layers were either parallel (ferromagnetic) or antiparallel (antiferromagnetic) in small magnetic fields.

The oscillatory coupling between ferromagnetic layers through a nonmagnetic (NM) metallic spacer layer, first observed on rare-earth[76] and transition metal[77] multilayers, has been shown to be a fairly general behavior.[78] Bartenlian *et al.*[79] first reported the unambiguous evidence of oscillatory coupling in Co/Au (111)/Co trilayers grown on glass platelets in ultrahigh vacuum (thermal evaporation and electron-beam evaporation). The maximum MR ratio $\Delta R/R_0 = [R_{max} - R(H_s)] / R(H_s)$, where H_s is the saturation field, was 2 %. Both the oscillation period and the dependence of the coupling strength on the spacer layer thickness are in good agreement with theoretical predictions based on a (Ruderman-Kittel-Kasuya-Yosida) RKKY model.[80] Parkin *et al.*[81] studied the oscillations of interlayer exchange coupling and GMR in (111) oriented permalloy/Au multilayers. They found the oscillation period is around 10 Å, which is significantly shorter than the period of 11.5 Å predicted in RKKY based models.

Roussigne *et al.*[82] derived the magnetic anisotropies and interlayer exchange interaction from Brillouin-scattering spectra of various thin film with one or two Co magnetic layers, evaporated in ultrahigh vacuum. The oscillatory behavior of the interlayer exchange interactions was also observed in Co/Au/Co sandwiches. The measured values of the pseudoperiod (9.6 Å) and the attenuation length (12 Å) agree well

with magneto-optical and magnetoresistivity measurements and with theoretical predications.

In most cases, the resistance of the magnetic layer by itself is unknown, since it is always covered by a nonmagnetic film in order to avoid oxidization. Therefore, Corno *et al.*[83] examined Au/Co/Au sandwiche resistance under variable magnetic field in a ultrahigh vacuum chamber. In their study, Corno *et al.* observed that the amplitude of the MR is weak when the cobalt is naked, then it grows with the thickness of the Au cover layer up until a thickness of five to six atomic planes. Nevertheless in all cases, the cobalt has a ferromagnetic behavior. These results were consistent with previous study. As reported by Grolier *et al.*,[84] the thickness of gold spacer layer in the bilayer Au/Co/Au/Co/Au was 1.2 nm in order to obtain an antiferromagnetic coupling between the two cobalt layers. The MR ratio $\Delta R/R$ is equal to 2.5 % at 300 K. The coercive field peak was observed at exactly one Au monolayer coverage, in full agreement with theory.

It is well established that GMR is due to spin-dependent scattering of the conduction electrons in the bulk or at the interface of the ferromagnetic (F) layers.[85] More precisely, the scattering probability D for a conduction electron crossing a ferromagnetic layer depends on its spin orientation with respect to that of the majority band so that $D\downarrow \neq D\uparrow$, where $D\downarrow$ ($D\uparrow$) refers to electrons with spin parallel (antiparallel) to the majority-spin band. The spin asymmetry of scattering is usually defined by $\alpha = D\downarrow / D\uparrow$.[86]

In a sandwich system with ferromagnetic layers F_1 and F_2, the magnetoresistance ratio $\Delta R/R$ is given by

$$\Delta R / R = (R_P - R_{AP}) / R_{AP} \propto \frac{1}{(D_1\downarrow - D_1\uparrow)(D_2\downarrow - D_2\uparrow)} \qquad \textbf{Equation 2-6}$$

where R_{AP} and R_P are the resistance of an antiparallel and parallel arrangement of the magnetization directions of F_1 and F_2 respectively. For equivalent ferromagnetic layers, the resistance is larger for an antiparallel arrangement than for a parallel one ($\Delta R/R < 0$), which is normal GMR, independently of whether $\alpha > 1$ or $\alpha < 1$. On the other hand, if F_1 and F_2 are different such that $\alpha_1 > 1$ ($D_1\downarrow > D_1\uparrow$) and $\alpha_2 < 1$ ($D_2\downarrow < D_2\uparrow$), one would expect an inverse GMR ($\Delta R/R > 0$).

Renard *et al.*[87] studied the inverse magnetoresistance in the $Fe_{1-x}V_x$/Au/Co system. At low temperature the Au/$Fe_{0.82}V_{0.18}$/Au/Co/Au structure shows an inverse GMR of -0.2 %; on the contrary, the Au/Co/Au/Co/Au structure shows the normal GMR with maximum value of 8 %. And also, the temperature dependent inverse GMR decreases in magnitude as the temperature increase, but remains negative up to room temperature in the films with x =30 %. In the films with x =18 %, MR ratio goes through zero near 240 K, and then exhibits negligibly small positive values at room temperature.

2.5 Nanolithography

Nanolithography is the art and science of etching, writing, or printing at the nanoscopic level.[88] It includes various methods, such as nanoimprint lithography, electron-beam lithography, soft lithography, and Dip pen Nanolithography ™ (DPN). Currently, electron-beam lithography is the most developed and popular direct-write method of nanolithography, which employs an electron-beam to fabricate nanostructures. However, those problems such as charging, wave diffraction and scattering limit the obtainable resolution.

Comparatively, nanoimprint lithography has the advantage of high resolution, considerable throughput and low cost. Nanoimprint lithography is similar to electron-beam lithography, except that a mechanical mold or mechanical force (embossing) is used to create the pattern in the resist. In other words, nanoimprinting refers to the first step of pressing the pattern in the resist, while lithography refers to the generation of the patterned resist used in the fabrication process. In 2002, by using ultra violet nanoimprint lithography, Seekamp *et al.*[20] fabricated low refractive index passive optical devices with polymethylmethacrylate (PMMA) and polystyrene (PS). Lim *et al.*[21] reported an electrochemical method to prepare a nanostamp. The method included electrodeposition of compositionally modulated NiCuFe/Cu multilayers and selective etching of the Cu layer, to prepare a one-dimensional grating mold on a sub-micron scale. This metal multilayer-etched stamp was used to cast the multilayer image in rubber and emboss it in Teflon.

CHAPTER 3 EXPERIMENTAL

3.1 Thin Films Electrodeposition

3.1.1 Electrolyte

The electrolyte for thin films electrodeposition is listed below in **Table 3-1**. The bath constituents are similar to Ref [18] with one important consideration, that the cyanide species have been removed. In the preparation of the electrolyte, analytical grade reagents from Fisher Scientific International were used with deionized water of 18 mega ohms-cm. The gold plating solution is from a commercial vendor (Technic, Inc., Techni Gold 25E). The pH values were adjusted with sulfuric acid and potassium hydroxide at room temperature by using an Orion® Model 420A pH meter. To optimize the electrolyte, three different citric acid concentrations (0.47 mol/L, 0.67 mol/L, 0.87 mol/L) and three different pH values (5.15, 6.15, 8.03) were tested.

Table 3-1 Composition of AuCo bath for thin films plating

Constitute	**g/L**	**mol/L**
$CoSO_4 \cdot 7H_20$	80	0.29
KOH	120	2.14
Au (Techni ® Gold 25E)	0.082	0.00042
$C_6H_8O_4 \cdot H_2O$	Variable	
pH	Variable	
Room Temperature		

3.1.2 Rotating Disk Electrode (RDE)

A rotating disk electrode (RDE) is used in the Au/Co system experimental studies of the electrodeposition due to (1) stable, laminar flow over a wide range of operating conditions, (2) uniform mass transport boundary layer thickness and (3) uniform limiting current density. As the disk rotated, fluid containing reactants is uniformly drawn towards its surface so that the reaction rate (current distribution) is uniform at the limiting current on the electrode. The Levich equation, **Equation 3-1**, describes the relation between the boundary layer thickness and the rotation rate,

$$\delta_N = 1.61 \cdot D^{1/3} \cdot \omega^{-1/2} \cdot \nu^{1/6} \qquad \textbf{Equation 3-1}$$

where δ_N is the boundary layer thickness, D is the diffusion coefficient, ω is the angular velocity and ν is the kinematic viscosity of the solution. In terms of the limiting current density the above equation can be recast, $i_{\lim} = nFDC^b / \delta$,

$$i_{\lim} = 0.62nFC^b D^{2/3} \nu^{-1/6} \omega^{1/2} \qquad \textbf{Equation 3-2}$$

where $i_{\lim}$ is the limiting current density, n is the electrons transferred, F is the Faraday constant, and C^b is the bulk concentration.

The non-uniform current density distribution below the limiting current is one of the least desirable features of the RDE, which leads to edge effects, preferential plating on the edges of the disk. This effect is pronounced when the reaction rate is fast and mass transport is not dominating. Under these conditions, referred to as primary current distribution, the current distribution is mostly determined by the electrolyte conductivity, geometry of the cell and the placement of the electrodes.

The RDE is placed in a PINE AFMSRX Rotator. The rotation rate of the electrode may be precisely controlled using a four digit pushbutton control on the front panel. The rotation rate is adjustable to within 1 % of the control setting over a range from 50 to 10,000 rpm.

3.1.3 Substrate Preparation

In electrodeposition, the nature of the substrate, upon which the plating occurs, has substantial influence on electrodeposits, their structure and properties. This is particularly true when the deposit is of less than 1 μm thick, such as the multilayer thin film discussed in **Section 4.2**. When the deposit's thickness is 1 μm or more (such as the nanoimprint mold in **Section 4.2.3**), electrochemical parameters play a more decisive role in the deposit properties.

The mechanical polish preparation of the substrate includes three steps:

1. Coarse polishing: using various grit silicon carbide papers 500, 1200, 4000;
2. Polishing/finishing: using colloidal silica with OP-NAP polishing cloth;
3. Fine polishing/finishing: using diamond spray and DP-red lubricant with MD-mol polishing cloth.

The chemical cleaning is to use 1 M H_2SO_4 solution to remove the oxide film on the copper disk surface.

3.1.4 Cell Set-up

The schematic of the electroplating cell used for thin film plating is shown in **Figure 3-1**. The reaction kettle is a HDPE plastic jar of 1000 mL capacity. A copper rotating disk

electrode (RDE) with a diameter of 0.6 cm is used as the cathode, where Au/Co alloy and multilayered thin films are plated. A 4 x 4 cm platinum mesh is used as the anode, affixed to a plastic support. A saturated calomel electrode (SCE) is employed as a reference electrode. To minimize the ohmic drop, the reference electrode is placed close to the working electrode, but not too close to shield the cathode.

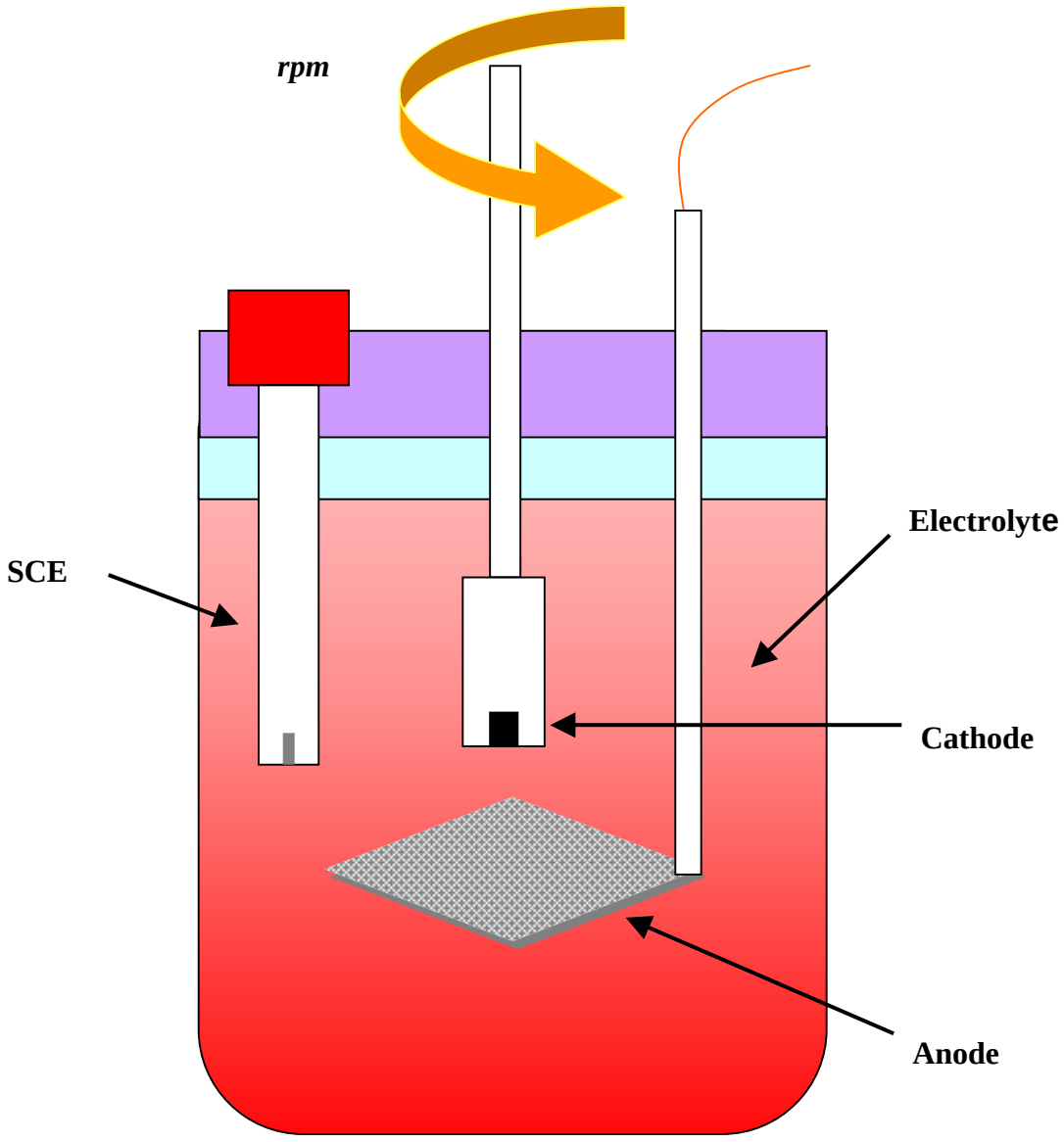

Figure 3-1 Schematic of the cell for thin film electrodeposition

3.2 Nanowire Fabrication

3.2.1 Electrolyte

A single, thiosulfate-sulfite Au/Co electrolyte was developed for Au/Co nanowire electroplating, the composition is listed in **Table 3-2**. This electrolyte is similar to the one used for thin film plating with a rotating disk electrode (RDE), but with more concentrated Au ions in order to compensate for the longer diffusion distance in AAO/polycarbonate membrane templates and thus improve the deposition rate, and current efficiency. The cobalt concentration was still kept in excess to the gold concentration to obtain alloys rich in cobalt. The electrolyte was made by the same method as previously described in **Section 3.1.1**. The pH value was fixed at 6.15 and nanowire fabrication was operated at room temperature.

Table 3-2 Composition of AuCo bath for nanowire electroplating

Constitute	**g/L**	**mol/L**
$CoSO_4 \cdot 7H_20$	80	0.29
KOH	100	1.782
Au (Techni ® Gold 25E)	0.123	0.00062
$C_6H_8O_4 \cdot H_2O$	97.92	0.47
pH	6.15	
Room Temperature		

3.2.2 Working Electrodes

3.2.2.1 Recessed Rotating Disk Electrode

In this study, two kinds of working electrodes were employed. **Figure 3-2** illustrated the recessed rotating disk electrode.[89] It consisted of an electrode body with a threaded cap which could be adjusted to mask the edge of the rotating disk. The exposed electrode diameter was 3 mm. The electrode material was stainless steel having an exposed area of 0.0706 cm^2.

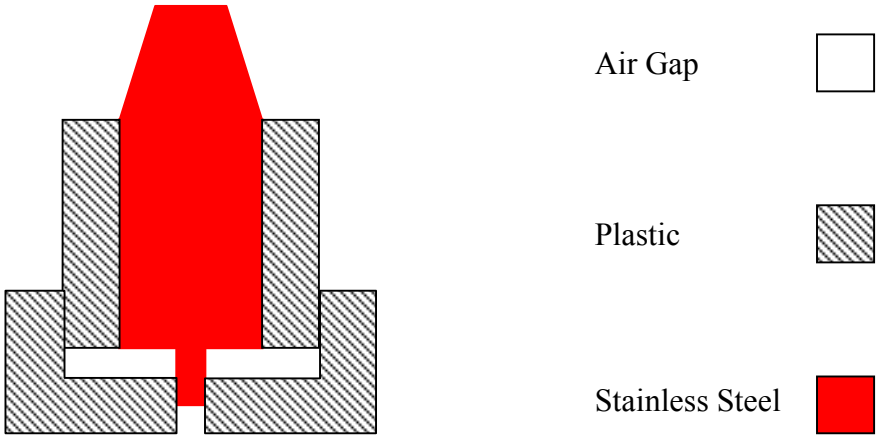

Figure 3-2 Schematic, cross-sectional drawing of the recessed rotating disk electrode

3.2.2.2 Stagnant Electrode Holder

Figure 3-3 is a schematic of the stagnant electrode holder used for nanowire electroplating. This electrode holder is composed of two circular PEEK discs of radius 5.5 cm and thickness of 1.0 cm. The upper disc center is a round opening of diameter 1.5 cm, which provides a plating area of 1.767 cm^2. Through this circular hole, the substrate contacts with the electrolyte. On the back of the upper disc, two different O-rings were embedded in grooves to prevent the electrolyte from contacting the backside of the membrane.

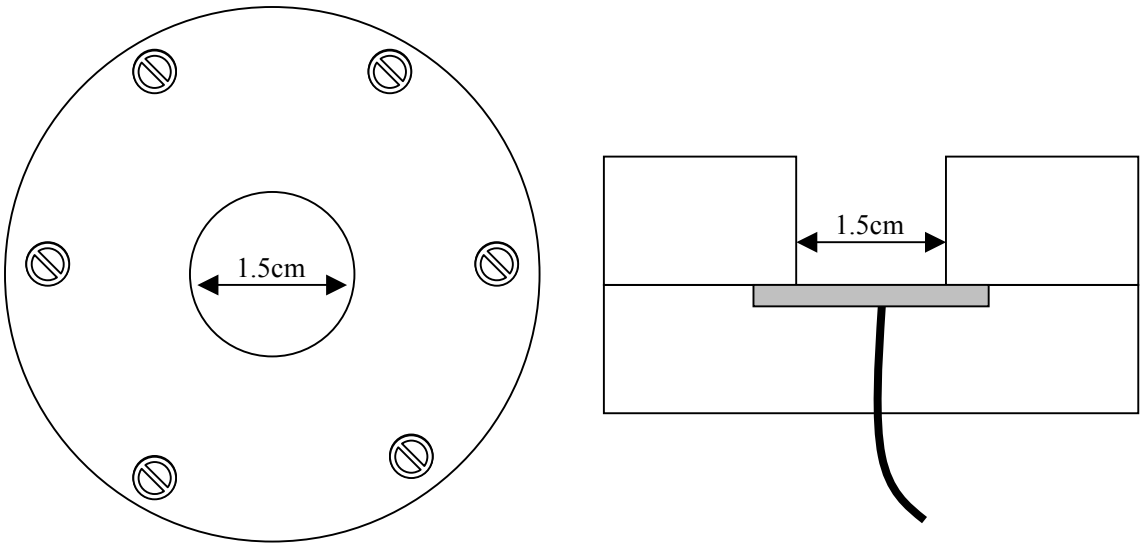

a. Top-view b. Cross-section view

Figure 3-3 The stagnant holder for nanowires electrodeposition

A square stainless steel plate of 2.5 x 2.5 cm was embedded into a recess on the bottom plastic disc so that the entire surface was planar and conductive. Electrical contact was provided by means of an insulated copper wire to the back of the stainless steel plate, fixed and sealed with resin to insulate the bottom of the electrode from the electrolyte. The top and bottom pieces were fastened by six screws on the outer edge of the discs.

3.2.2.3 AAO/Polycarbonate Membrane

Anodic Alumina Oxide (AAO, Whatman® Anodisc®) and polycarbonate (Whatman® Nuclepore®) membranes were used as templates for nanowire plating. Membranes having different pore sizes were tested, ranging from 0.01 μm to 0.8 μm. The deposition procedure is shown in **Figure 3-4**. Before plating, a layer of Au was sputtered onto one side of the membrane to serve as conductive substrate, **Figure 3-4(b)**, and to seal the nanometric pores. Then the membranes were fixed on the recessed rotating disk electrode or the stagnant electrode holder, with the sputtered Au layer side contacted with the

stainless steel electrode. As the plating proceeded, nanowires grew in the pores and filled up the pores, **Figure 3-4(c)**. After the nanowire plating, a solution of 1 M NaOH and another of dichloromethane were used to dissolve the AAO and polycarbonate membranes respectively, to release the nanowires for further analysis, **Figure 3-4(d)**.

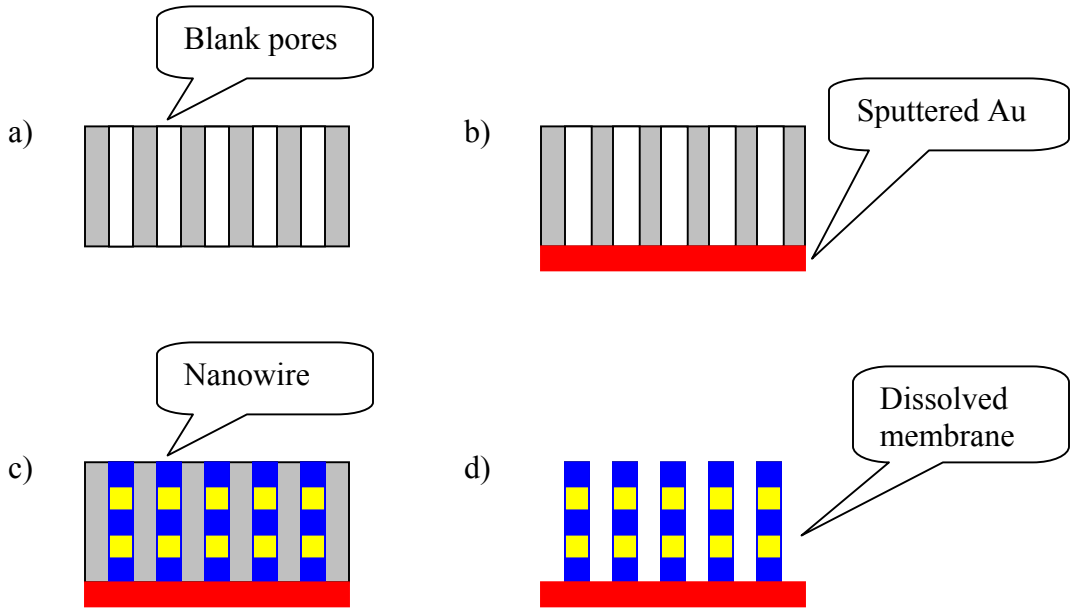

Figure 3-4 Nanowire growth procedure in AAO/polycarbonate membrane templates

3.2.3 Cell Set-up

3.2.3.1 Recessed Rotating Disk Electrode

The plating cell set-up for the recessed rotating disk electrode is illustrated in **Figure 3-5**. A HDPE plastic jar of 1000 mL is used as the reaction kettle. A polycarbonate membrane fixed on a stainless recessed rotating disk electrode with a diameter of 3 mm is used as the cathode. The same platinum mesh as used in the thin film experiments were also used when plating the nanowires. A saturated calomel electrode (SCE) is employed

as a reference electrode. The rotating rate of the recessed rotating disk electrode is 1600 rpm, controlled by PINE AFMSRX Rotator.

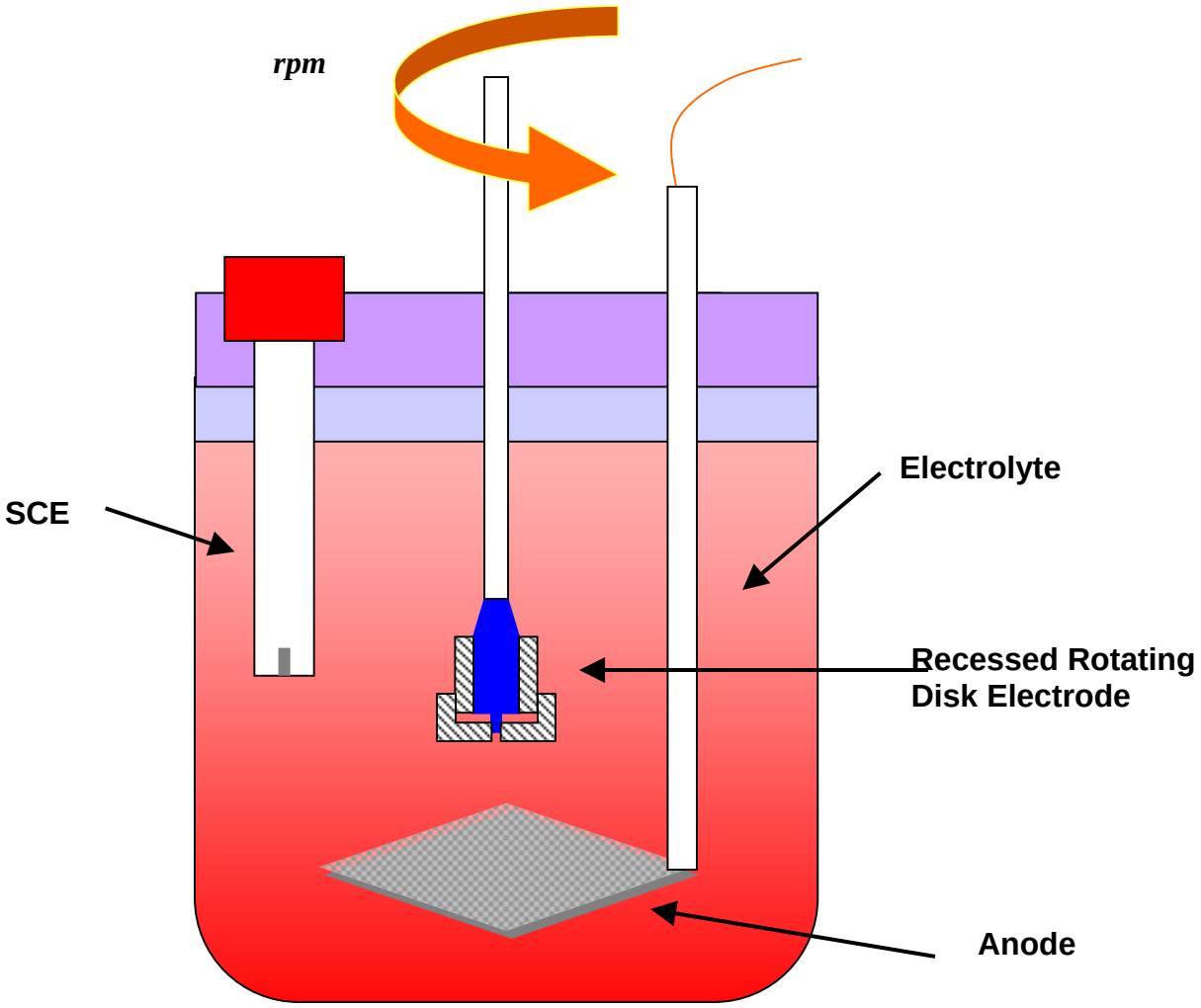

Figure 3-5 Electroplating cell for recessed rotating disk electrode

3.2.3.2 Stagnant Electrode Holder

For the stagnant holder, a new cell was designed, shown in **Figure 3-6**. The electrode holder was placed on the bottom of the cell, with same platinum mesh and reference electrode in **Figure 3-5.** The solution was agitated by a PTFE blade-type agitator controlled by PINE AFMSRX Rotator at 900 rpm.

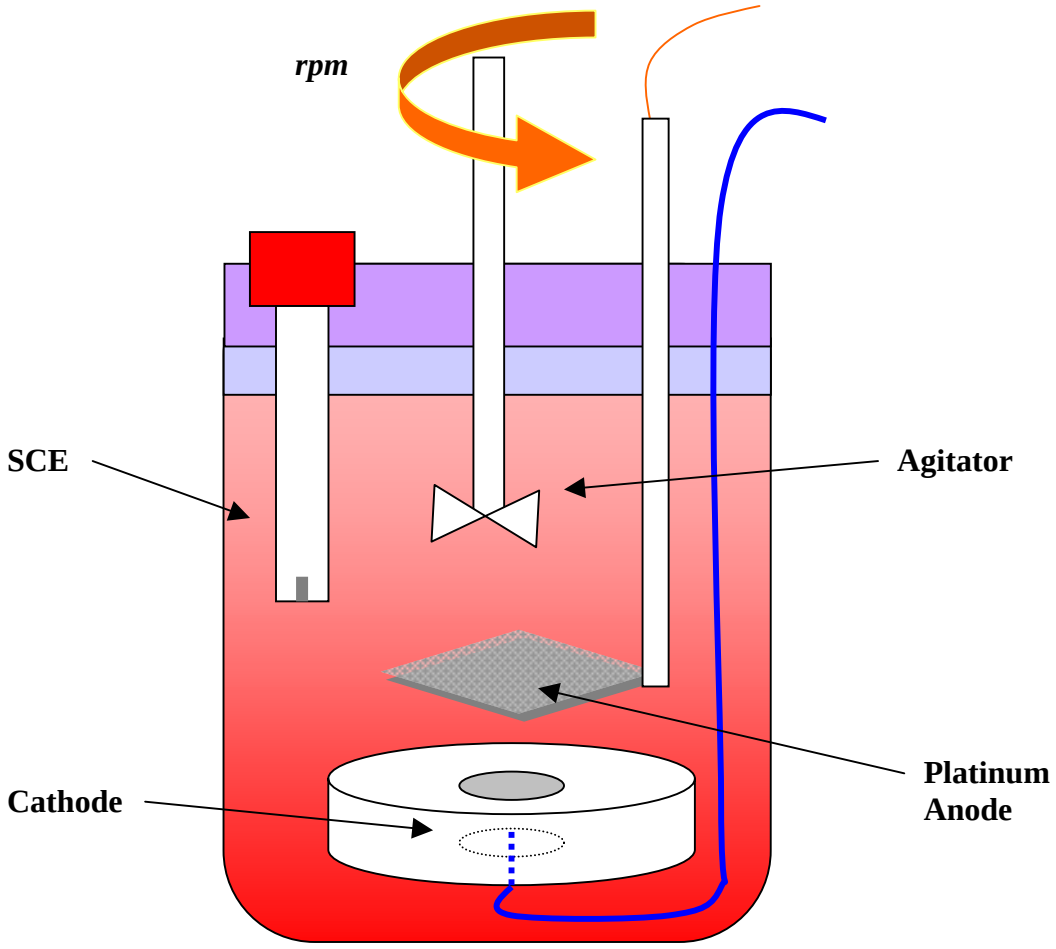

Figure 3-6 Schematic cell for nanowires electrodeposition

3.3 Methods

3.3.1 Polarization

Polarization curves, which correlate the current density with the applied potential at steady-state, were carried out on a Bas-Zahner IM6 Zahner® unit with a sweep rate of 2 mV/s. The potential sweep starts at open circuit potential (OCP), where the net current density is zero, and stopped when the side reactions are overwhelmingly dominant due to excessive gas generation. Finally the potential was corrected for ohmic drop, which was measured by impedance analysis unit in the Bas-Zahner IM6.

3.3.2 Impedance Analysis

Impedance is a measure of the ability of a circuit to resist the flow of electrical current. The ohmic drop ($I \cdot R_\Omega$) can be calculated, with the measured, ohmic resistance, R_Ω from the impedance data. The working potential is corrected accordingly,

$$E_{WE} = E_{measured} - (I \cdot R_\Omega) \qquad \textbf{Equation 3-3}$$

3.3.3 Current Efficiency and Partial Current Density

In the Au/Co system, the deposition of Au (I) and Co (II) ions are the main electrochemical reactions. There are also several possible side reactions that can occur simultaneously. The reactions are listed from **Equation 3-4** to **3-7**.

Electrochemical Reactions

$$Au\ (I) + e^- \rightarrow Au \qquad \textbf{Equation 3-4}$$

$$Co\ (II) + 2e^- \rightarrow Co \qquad \textbf{Equation 3-5}$$

Side reactions:

$$2H_2O + 2e^- \rightarrow 2OH^- + H_2 \qquad \textbf{Equation 3-6}$$

$$O_2 + 2H_2O + 4e^- \rightarrow 4OH^- \qquad \textbf{Equation 3-7}$$

The current efficiency (η) is the ratio of current density used to electrodeposit the metals compared to the total applied current density, which is usually expressed on a percent basis

$$\eta = \frac{\sum i_{metal}}{i_{total}} * 100\% = \frac{\sum i_{metal}}{\sum i_{metal} + i_{side}} * 100\% \qquad \textbf{Equation 3-8}$$

Each partial current density is calculated from Faraday's Law, shown in **Equation 3-9**.

$$i_j = \frac{n_j F m_j}{s_j M_j t A} \qquad \textbf{Equation 3-9}$$

where i is the current density for each metal, n is the number of electrons transferred, F is the Faraday's constant, m is the mass actually plated, s is the stoichiometric coefficient, M is the molecular weight, t is the plating time, and A is the effect area of the working electrode. The mass actually plated (m) is the product of the deposit thickness, plated surface area and mass density. The deposit's thickness and composition are measured by a Kevex Omicron X-ray fluorescence (XRF).

3.3.4 Alloys and Multilayer Plating

Figure 3-7 illustrates the plating schematics. Galvanostatic (constant current) plating is used for AuCo alloy plating. Different current densities, ranging from -0.25 mA/cm^2 to -350 mA/cm^2, were tested to deposit pure Au and nearly pure Co-rich alloys. In galvanostatic plating, the layer thickness can be kept constant by controlling the plating time. For the Au/Co multilayer thin film electrodeposition, a two galvanostatic, square-wave pulsed plating was carried out with currents of -1 mA/cm^2 for the Au layer and -100 mA/cm^2 for the Co layer with variable times. The multilayered nanostructures having large layer thickness > 100 nm were examined by scanning electron microscopy (SEM).

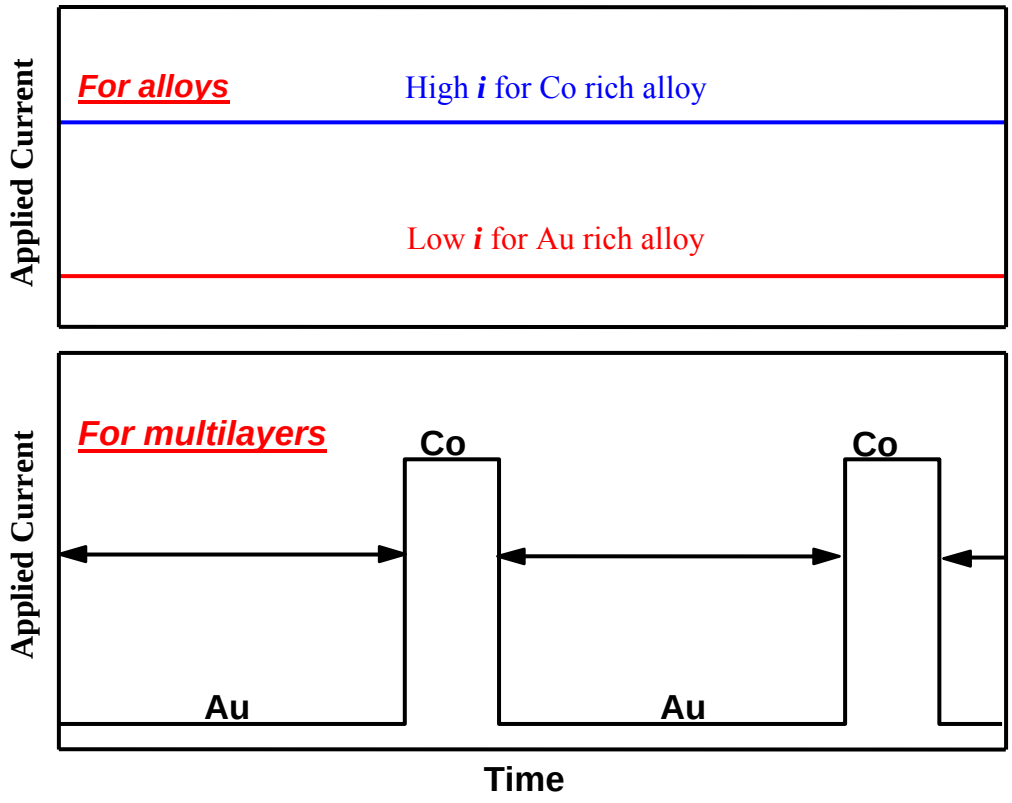

Figure 3-7 Schematic of DC (top) and square-wave pulse (bottom) plating

3.4 Deposit Characterization

3.4.1 XRF

A Kevex Omicron X-ray fluorescence (XRF) unit is used to measure the composition and thickness of the deposited alloy films. The XRF uses the energy-dispersive X-ray spectrometry (EDS) analytical method to analyze the elements. The x-ray radiation, produced by an X-ray source consisting of an electron gun and a target sealed inside a vacuum envelop, is directed at the deposit and the energy emitted from the deposit is measured, which is proportional to the deposit thickness. The detected x-rays are presented as a spectrum. After calibrating with known standards, the composition of the alloy film can be determined. In this Kevex Omicron XRF, the collimator size is 100 μm,

and the x-ray conditions were adjusted in an air environment to achieve a detector dead time around 50 %. The composition is integrated and averaged from 6 points scanned along the diameter of each rotating disk electrode and nanowire membrane.

3.4.2 SEM

The scanning electron microscope (SEM) (Jeol JSM-840A SEM located in Department of Geology and Geophysics, LSU, and Hitachi S-4500II Field Emission SEM with EDAX located in CAMD, LSU) is used to observe both the deposit surface morphology.

In the SEM, an incident electron beam (primary electrons) excites free electrons inside a specimen and the excited electrons (called the second electrons) are subsequently emitted from the specimen surface. The quantity of these secondary electrons, which are collected by a detector, changes with the location of the surface and contribute to variations in the image contrast. A protruding site produces more secondary electrons and thus appears white, whereas a flat region emitting fewer or zero electrons shows up black. As a result, surface irregularities can be seen as black-white images. The accelerating voltage used was 20~30 kV.

SEM specimens have to be electrically conductive in a vacuum environment. The acrylic resin and alumina materials used in this study can also be examined if the surface is coated with a thin conducting film, such as gold or gold-palladium. Furthermore, materials giving low-contrast will provide better images in terms of sharpness and resolution after being coated with a gold or gold-palladium film. In the work presented here, a two-minute sputtering time was sufficient to obtain a continuous coating film. The

sputtering machine used was a Technics Hummer II Sputter Coater, located in Department of Geology and Geophysics, LSU.

3.4.3 XPS

X-ray photoelectron spectroscopy (XPS) is also used in this study to determine the elemental analysis of the deposited thin films. The Kratos AXIS 165 X-ray Photoelectron Spectroscope and Scanning Auger Microscope, which is located in LSU Materials Characterization Center, is equipped with standard Mg/Al source and high performance Al monochromatic source.

X-ray Photoelectron Spectroscopy (XPS) measures the energies of photoelectrons emitted from samples irradiated with soft x-rays. Only electrons emitted from the top few nanometers of the sample are detected, since electrons from deeper within the sample lose energy as a result of atomic interactions - this means XPS is a truly surface specific technique. The characteristic energies of photoelectron are influenced by chemical bonding states, and so by measuring peak shifts, it is possible to gain insight into the chemistry and oxidation state.[90]

3.4.4 TEM

The observation of nanometric multilayered microstructures below 50 nm was observed with transmission electron microscopy (TEM) (JEOL 100-CX TEM located in Socolofsky Microscopy Center in Department of Biological Sciences, LSU). TEM is able to resolve atomic features. The preparation procedures of nanowire specimens for the TEM includes: dissolving the membrane, rinsing by distilled water and then

centrifugalizing the suspension three times. Finally a drop of the suspension was placed on a holey carbon grid film and allowed to dry.

3.4.5 GMR

The giant magnetoresistance (GMR) effect was measured with a 9 T quantum design physical properties measurement system (PPMS), using the standard four-point probe ac technique at 27 HZ with an excitation current of 1 mA. **Figure 3-8** shows the schematic of the transverse magnetoresistance measurement, which is used to characterize the current-in-plane (CIP) GMR.

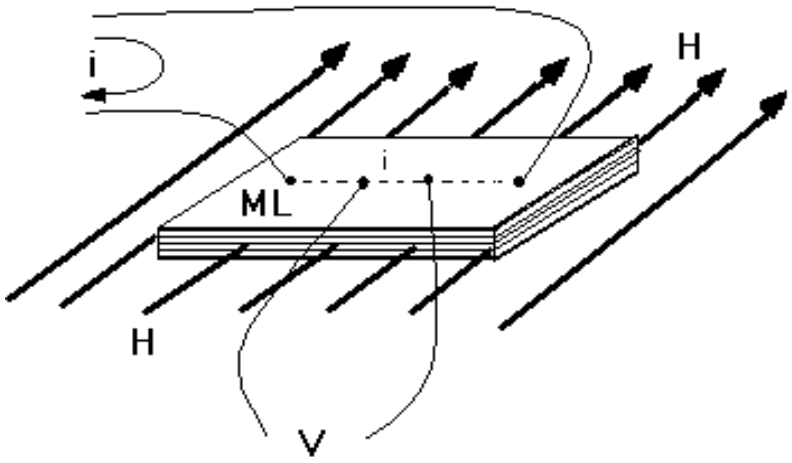

Figure 3-8 Transverse MR measurement

CHAPTER 4 RESULTS AND DISCUSSIONS

4.1 Au-Co Alloy Electrodeposition

4.1.1 Polarization Curves

A polarization curve, shown in **Figure 4-1,** was obtained with a copper rotating disk electrode at a rotation speed of 1600 rpm. In the polarization curve, a gold plateau (-4 mA/cm^2) was observed when the working potential is lower than -0.7 V, which confirmed that the gold can be successfully electrodeposited from this single Au-Co bath. The Au diffusion coefficient D_{Au} was calculated to be 3.49×10^{-6} cm^2/s from the value of the limiting current density and applying the Levich equation, which is reasonable. For example, Huang *et al.*[91] reported a value of 3×10^{-6} cm^2/s for copper diffusion coefficient in sulfate electrolyte. Chassaing *et al.*[92] reported a value of 5×10^{-6} cm^2/s for copper diffusion coefficient in a citrate electrolyte. The calculated diffusion coefficient for Au was in the same order of magnitude of Cu, and in a reasonable range.

In a single bath, a requirement for multilayer deposition is that the reduction potentials must be far enough apart to allow a disparate electrodeposition of the two components. In the Au-Co single bath, the precious metal (Au) was kept at a very low concentration and the less precious metal (Co) was kept at much higher concentration. In such a way, pure Au was electroplated at lower current density and the Co-rich alloy was achieved at higher current density.

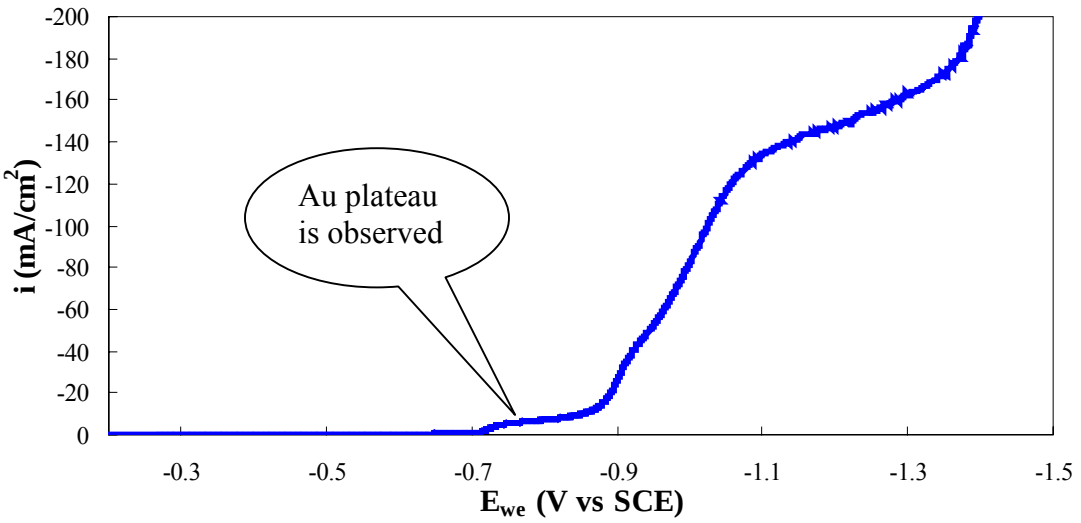

Figure 4-1 AuCo polarization curve which shows the Au plateau, 1600 rpm

Figure 4-2 shows three polarization curves corresponding to three different Au concentrations: 0, 0.00042, and 0.00083 mol/L Au (I). As the dotted arrow shows, the polarization curve increases from right to left with addition of Au. An increase in the limiting current density of Au was expected. The shift in the total current density indicates a change in complexing species, with a promotion of the Co reaction.

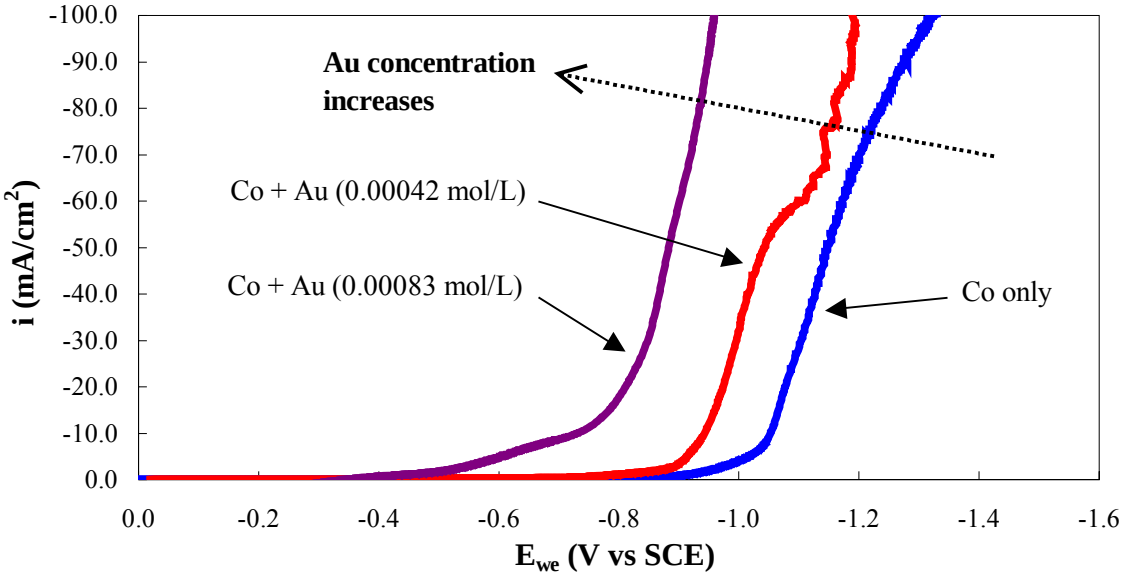

Figure 4-2 Au-Co polarization curves with different Au concentrations, 1600 rpm

4.1.2 Effects of Citric Acid

To optimize the citric acid concentration so that the elemental Au and a Co-rich alloy can be electrodeposited, three different citric acid concentrations were tested. The three solutions contain the same concentration of metal ions, except with varying citric acid concentrations: 0.47, 0.67, and 0.87 mol/L. **Figure 4-3** and **Figure 4-4** show the alloy deposit composition of Au and Co, respectively, as a function of current density, for a constant, unmodulated current density at rotation rate of 1600 rpm. As expected, at low current densities, nearly pure Au is deposited. In contrast, a Co-rich alloy is deposited at high current densities. This trend is true for all three solutions. Among them, the citric acid concentration of 0.47 mol/L exhibits the best results. Especially when the current density is lower than -1 mA/cm^2, the Au content stays around 99.5 (wt %). And also, when the current density is higher than -50 mA/cm^2, the Co content is higher than 98.8 (wt %). The high purity deposits are crucial to the success electrodeposition of multilayer thin films, which will be discussed in **Section 4.2**.

The current efficiency, shown in **Figure 4-5**, further confirms the advantage of citric acid concentration of 0.47 mol/L over the other two higher concentrations. The current efficiency is higher at 0.47 M citric acid concentration compared to 0.67 and 0.87 M in the region of the Co-alloy plating. All three electrolytes have a similar low current efficiency of 5 % at low current density, where Au is plated.

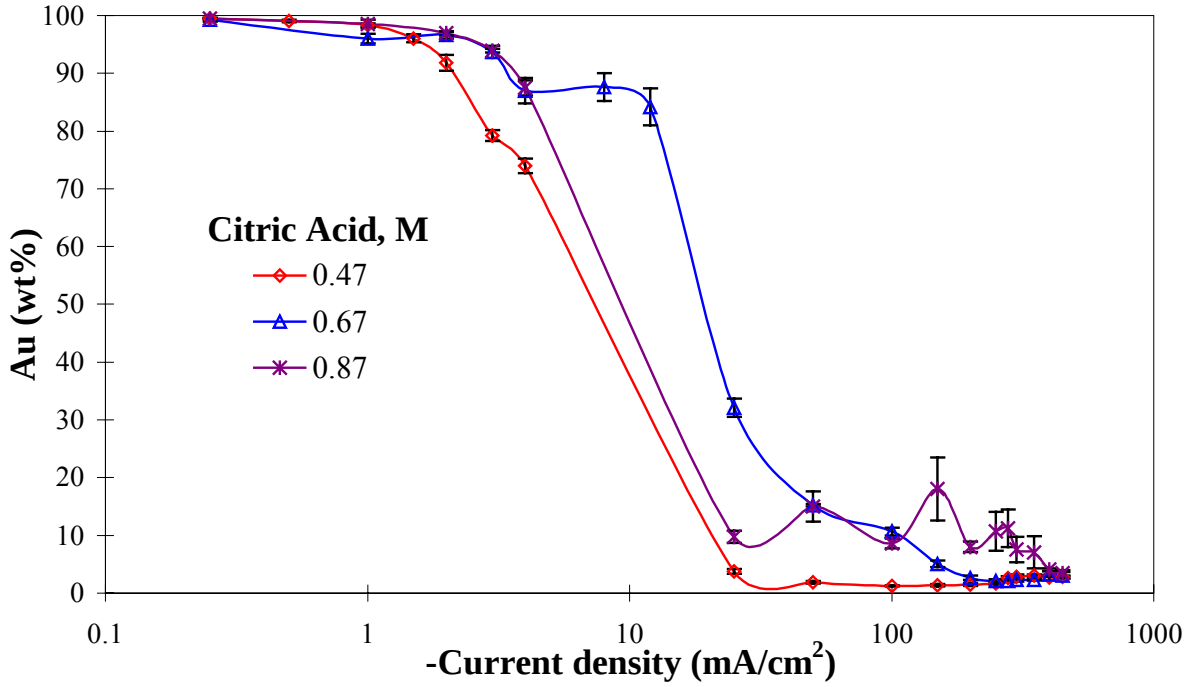

Figure 4-3 Au concentration change in galvanostatic deposited alloys at different citric acid concentrations, 1600 rpm

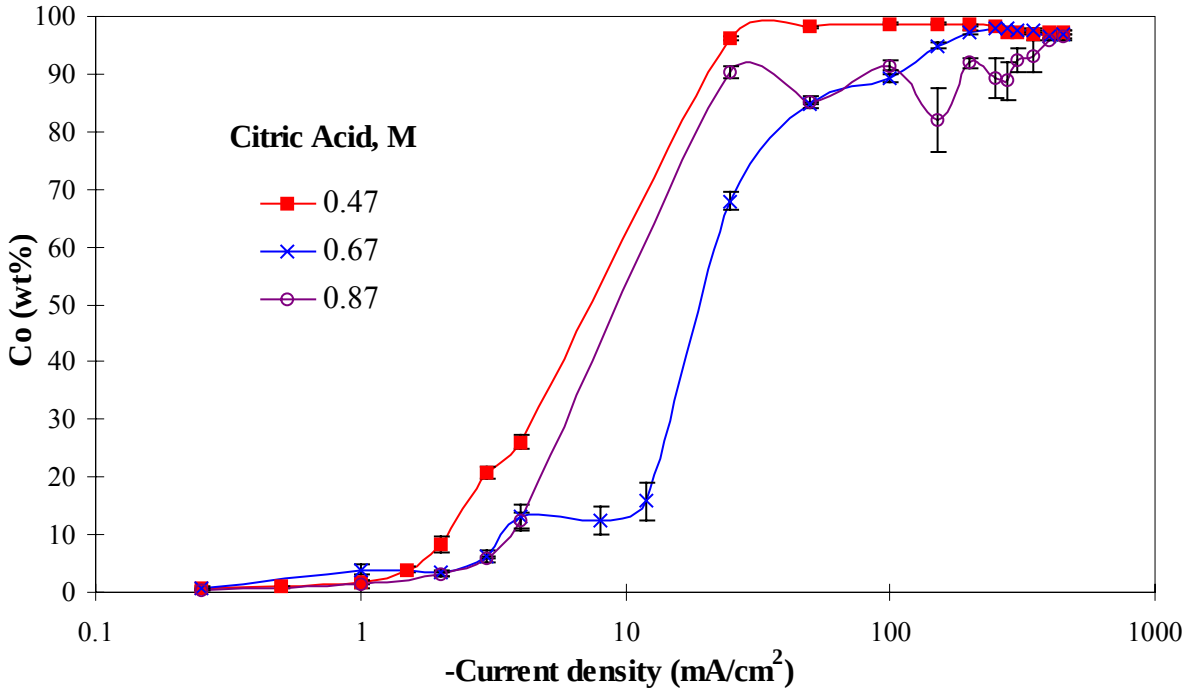

Figure 4-4 Co concentration change in galvanostatic deposited alloys at different citric acid concentrations, 1600 rpm

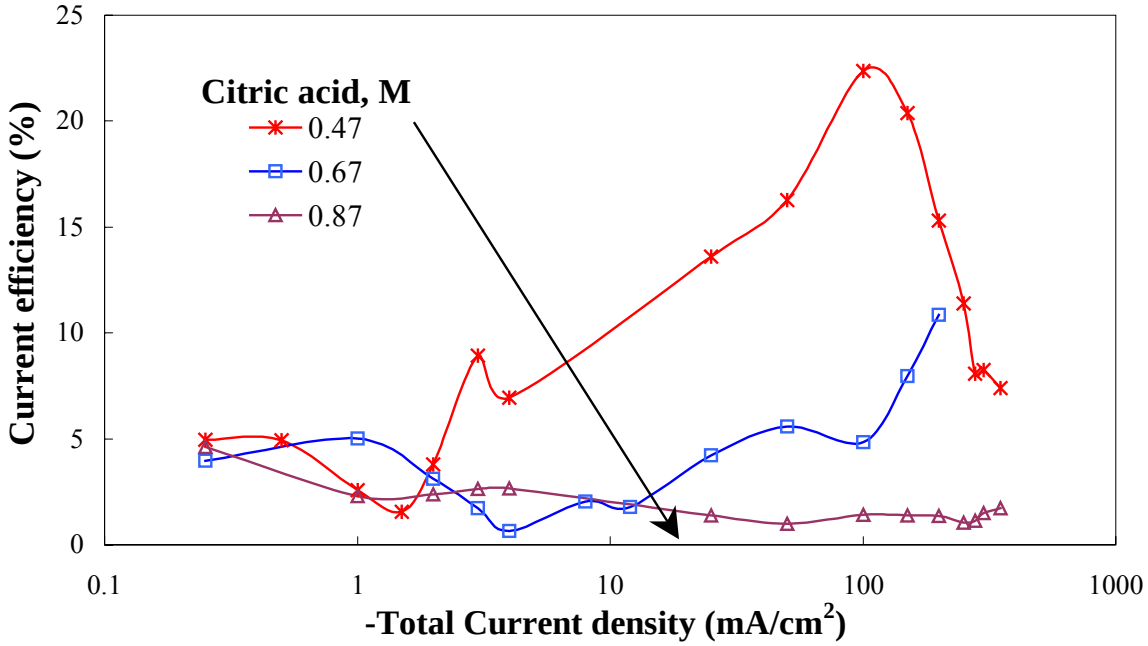

Figure 4-5 Current efficiency of the DC plated alloys at different citric acid concentrations

Both the alloy composition and current efficiency were used in the determination of partial current densities of each reactant and to determine the layer thickness used in the pulse plating experiments. The partial current densities of the gold and cobalt reactions are shown in **Figure 4-6**, the side reaction partial current density is shown in **Figure 4-7**. In **Figure 4-6**, the cobalt partial current density goes up with an increase of applied potential. Increasing citric acid concentration shifts the Co reaction rate to more negative potentials. The Au reaction rate is not significantly affected by the citric acid concentration. Furthermore, **Figure 4-7** reflects the fact that increasing citric acid concentration increases the side reaction rates, which, consequently, lowers the current efficiency, consistent with **Figure 4-5.**

It was observed that the higher the citric acid concentration, the more readily the gold complex decomposed as metallic gold precipitation. Thus, the 0.47 M citric acid

concentration exhibits the best stability with the largest current efficiency, and was chosen for further investigation.

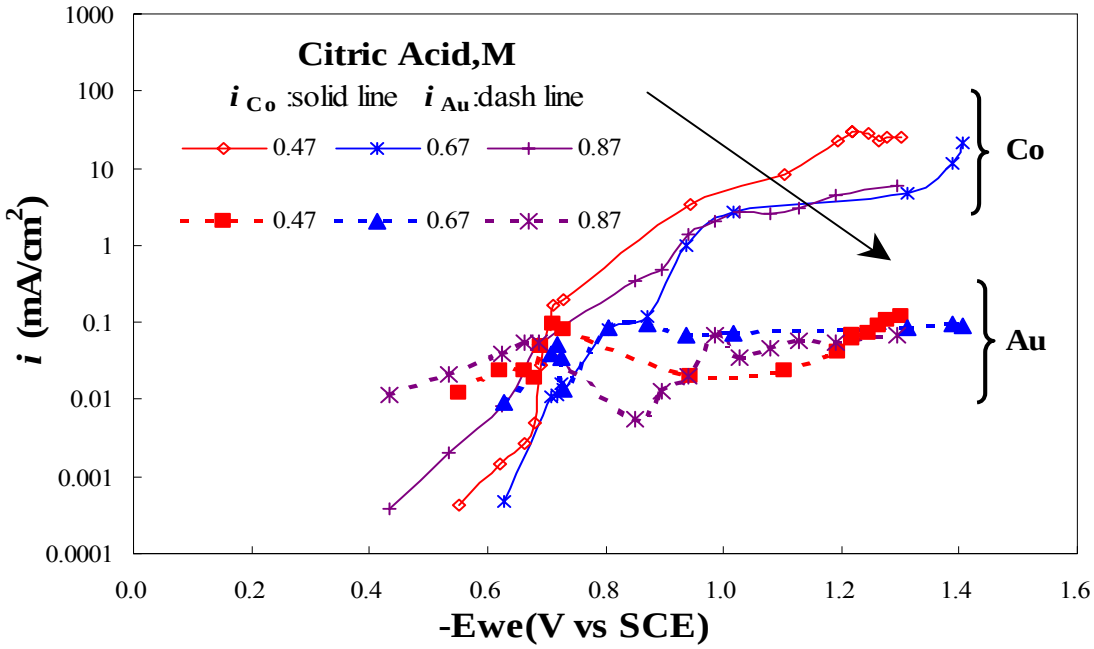

Figure 4-6 Au and Co partial current densities at different citric acid concentrations

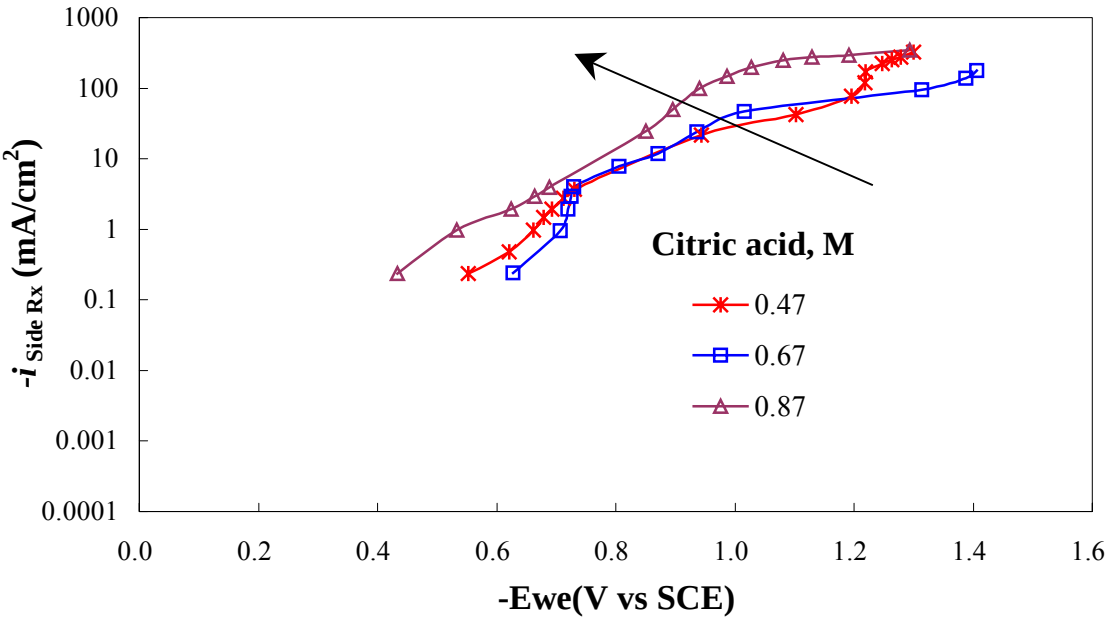

Figure 4-7 Side reaction partial current density at different citric acid concentrations

4.1.3 Effects of pH

The pH level is expected to impact the bath stability and possibly deposit composition. Five different electrolyte pH values (2.82, 4.04, 5.15, 6.15, 8.03) were examined. Without being used for electrodeposition, the solutions were stocked for several days. It was discovered that the gold precipitation occurred when the pH < 5.0.

Therefore three different pH levels (5.15, 6.15, 8.03), were tested to find the best electrolyte composition and electrodeposition parameters, to use in the multilayer structure. **Figure 4-8** and **Figure 4-9** show the alloy deposit composition as a function of pH levels, for a constant, unmodulated current density at a rotation rate of 1600 rpm. As expected, the elemental gold is deposited at low current densities, and a Co-rich alloy is deposited at high current densities. Among the three pH values, the slightly acidic value of 6.15 shows the best results. The Au content reaches 99.5 (wt %) when the current density is lower than -1 mA/cm^2, and the Co content is higher than 98.7 (wt %) when the current density is higher than -100 mA/cm^2.

Figure 4-10 shows the current efficiency in the galvanostatic electrodeposition of Au-Co alloys at the three different pH values. The trend is similar to **Figure 4-5**. The current efficiency is only 5 % at low current densities, goes through a minimum, and then goes up again approaching a value of 20 % at high current density for the lowest pH value.

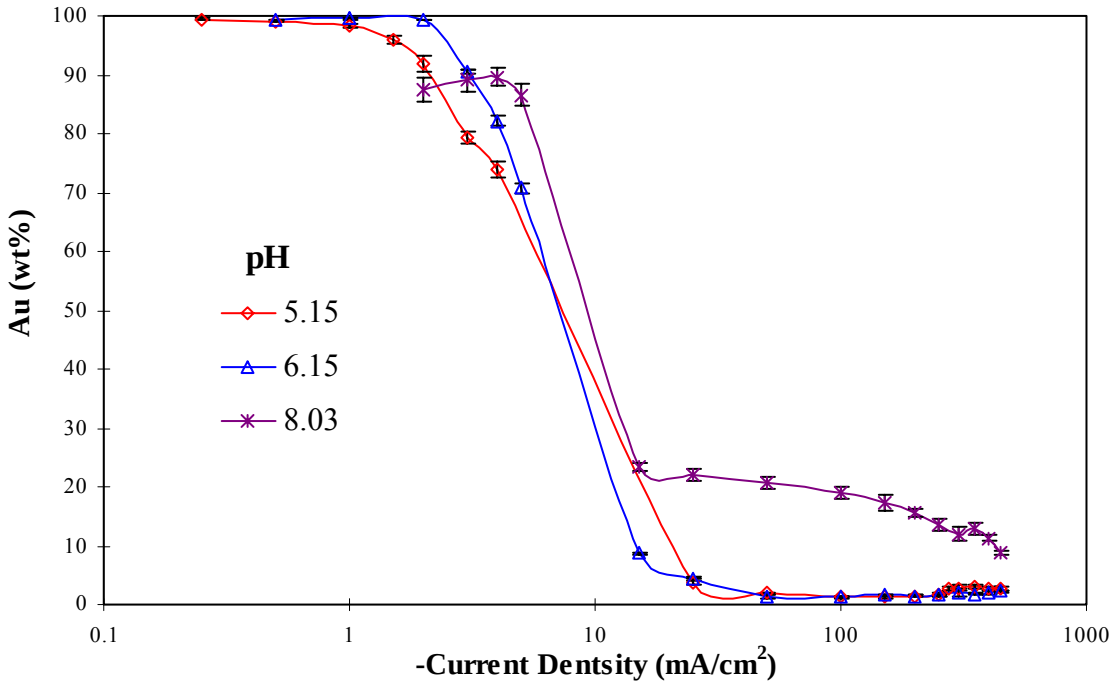

Figure 4-8 Au concentration change in galvanostatic deposited alloys at different pH values

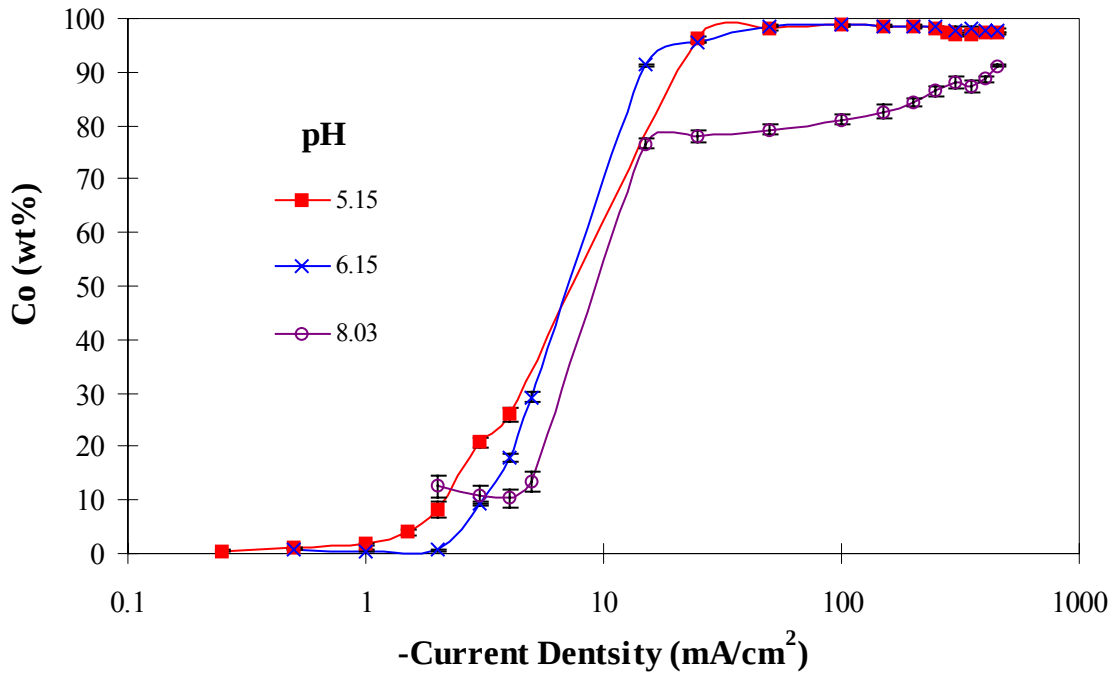

Figure 4-9 Co concentration change in galvanostatic deposited alloys at different pH values

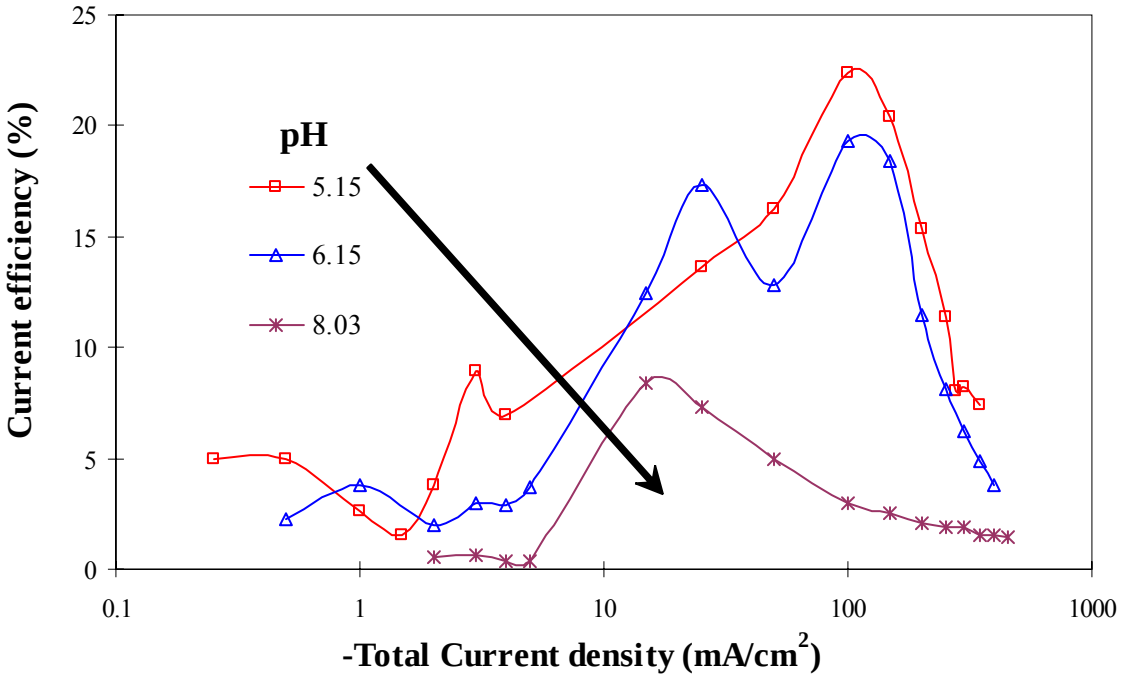

Figure 4-10 Current efficiency of the DC plated alloys at different pH levels

The partial current densities of each reaction were calculated from the above results of galvanostatic electrodeposition at different pH levels. **Figure 4-11** shows the partial current densities of gold and cobalt reduction; **Figure 4-12** shows the partial current density of the side reactions. In **Figure 4-11**, as expected, gold exhibits a limiting current at low current densities; and the cobalt partial current density goes up with an increase of applied potential, and also reaches a limit. Even though pH does not influence the Au reaction rate, a high pH of 8.03 does shift the Co reaction rate to a more negative potential, resulting in a lower current efficiency.

Figure 4-12 is a plot of the side reaction rates. The pH does not significantly alter the side reaction at high currents (or very negative potentials). At low current densities, the low pH of 5.15 has a lower side reaction rate than the higer pH of 8.03 or 6.15.

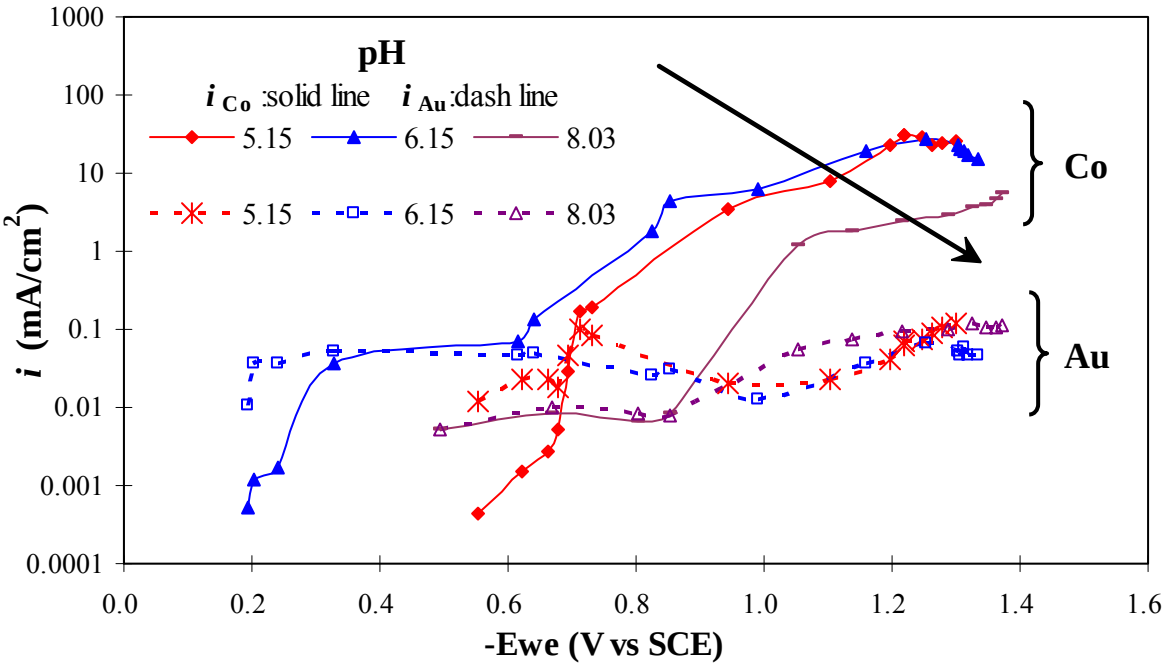

Figure 4-11 Au and Co partial current densities at different pH levels

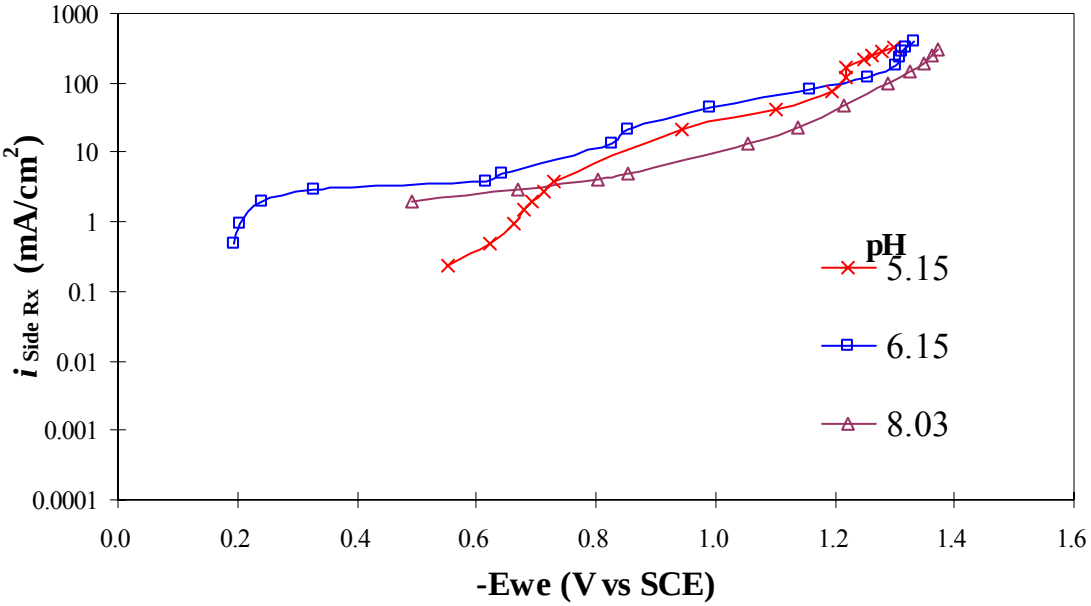

Figure 4-12 Side reaction partial current density at different pH levels

Based on the bath stability and the DC electrodeposited alloy composition, the slightly acid pH of 6.15 was chosen for further study.

4.2 Multilayer Thin Films Electrodeposition

4.2.1 Electrodeposition Parameters

Galvanostatic, square-wave pulsed plating was carried out with currents of -1 mA/cm^2 for the Au layer and -100 mA/cm^2 for the Co layer with variable times. At low current density elemental gold is deposited, while at high current density a cobalt rich alloy (98.7 % Co) is obtained.

4.2.2 XPS

XPS analysis was employed to determine if oxygen was present in the film. Oxygen is expected to be present on the deposit surface, since Co readily forms a cobalt-oxide in air. However, oxygen present in the bulk would indicate partial reduction of the metal species. A multilayer film was tested that was plated under the same conditions described above on a rotating disk electrode, having 5 nm Au layers and 5 nm Co-rich alloy layers, repeated four times. In XPS analysis, etching is carried out from the surface of the film toward the bottom near the Cu disk substrate.

Figure 4-13 shows the oxygen content as a function of the etching time. The oxide is only present at the film surface, as expected due to the oxygen in the air. In the film depth, no oxygen was detected. This confirms that the metallic Au or Co-rich alloy layers are completely reduced and can be plated successfully.

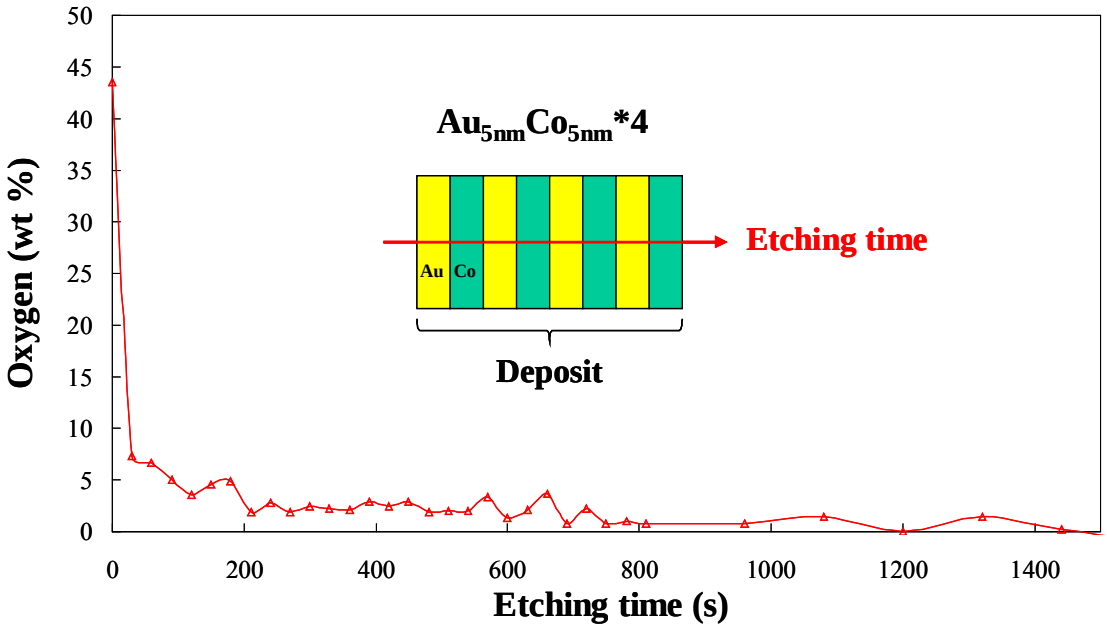

Figure 4-13 Schematic of XPS analysis of Au/Co multilayer films

4.2.3 GMR

The current-in-plane giant magnetoresistance (CIP-GMR) was measured at room temperature. GMR is defined as **[R(H)-R(0)]/R(0)*100**, where R(H) is the resistance in an external field H, and R(0) is the resistance when the external field is zero. The plating current densities for each bilayer were -1 mA/cm^2 for the Au layer and -100 mA/ cm^2 for the Co layer with variable times.

Two series of multilayers were plated on Cu (100) foil for the investigation of GMR behavior with film thickness. The GMR measurement was performed with the multilayer on the Cu foil, which contributes to a short circuit for the in-plane current flow, as shown in **Figure 4-14** at low fields. Therefore, a much higher magnetic field was needed for the demonstration of GMR behavior. There was no MR at low field due to the shunting of the current through the copper substrate, as expected.

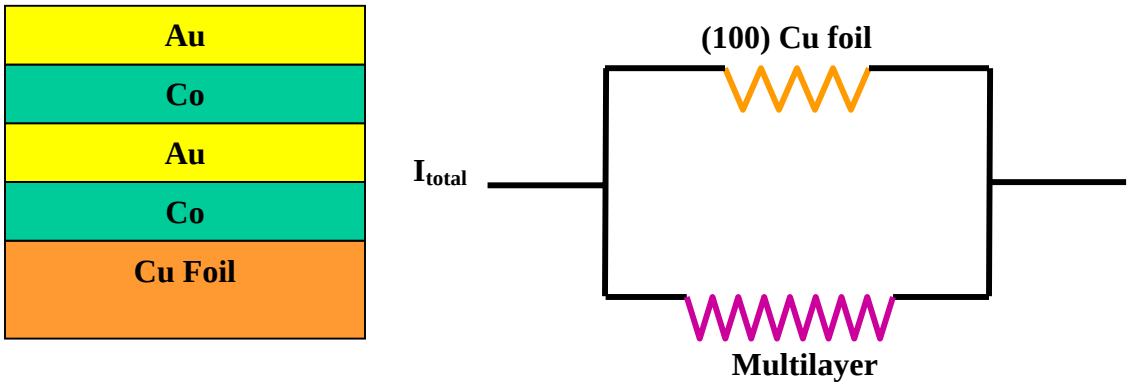

Figure 4-14 Schematic of GMR on Cu foil substate

Figure 4-15 shows that the magnetoresistance varies with Co-rich layer thickness. The Au layer thickness was fixed at 3 nm by maintaining the plating time while the Co-rich layer plating time varied from 2 nm to 5 nm. The Au/Co multilayers plated on Cu foil does exhibit a change in resistance, with large magnetic field. Also, the observed GMR is positive when the Co-rich layer is thinner than 4 nm. Increasing the Co-rich layer thickness, the GMR changes from positive to negative with more than 13 % GMR. This sample was comprised of 3 nm Au layer and 5 nm Co layer, having 925 bilayers.

In a second series of experiments the Au layer thickness was varied. **Figure 4-16** shows that the magnetoresistance varies with Au layer thickness. Similar phenomenon happened to the second sample series. The Co-rich layer thickness was fixed at 4 nm by keeping the plating time constant while the Au layer plating time varied from 1.5 nm to 4 nm. The GMR is positive when the Co-rich layer is less than 3 nm. While for the sample consisting of 4 nm Au layer, 4 nm Co layer and having 925 bilayers, the GMR changes from a positive to negative value with a GMR of more than 7 % at a magnetic field of 9 Tesla.

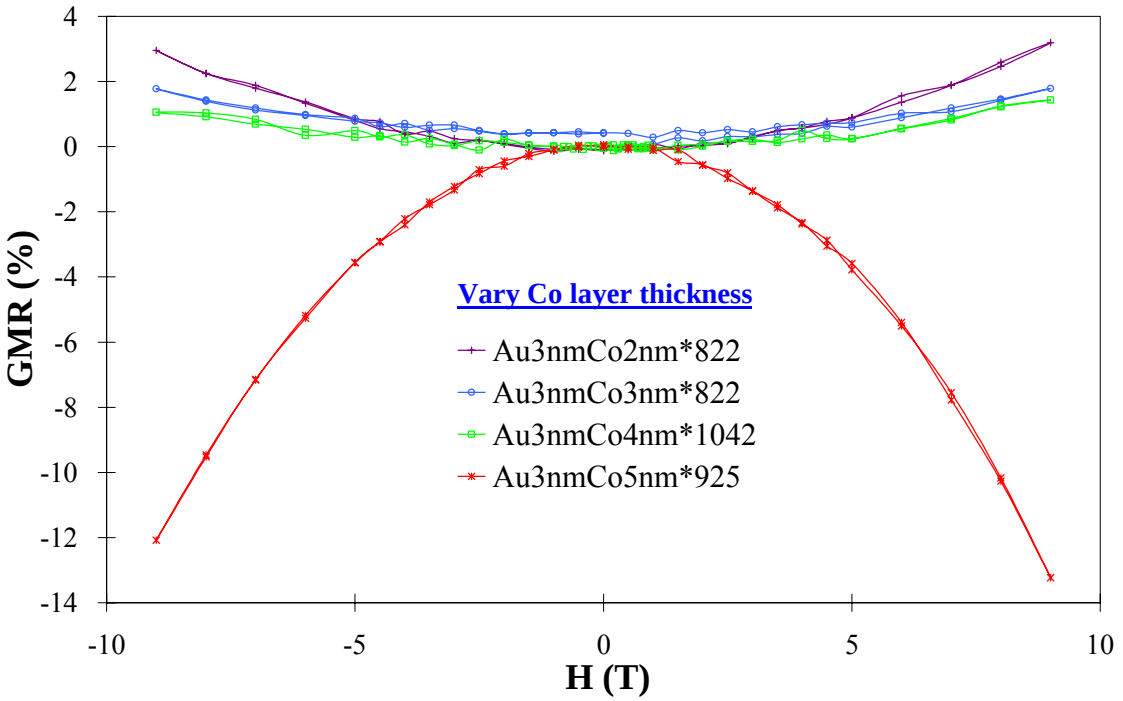

Figure 4-15 GMR results of Au/Co multilayer films on Cu foil substrate, with variable Co layer thickness

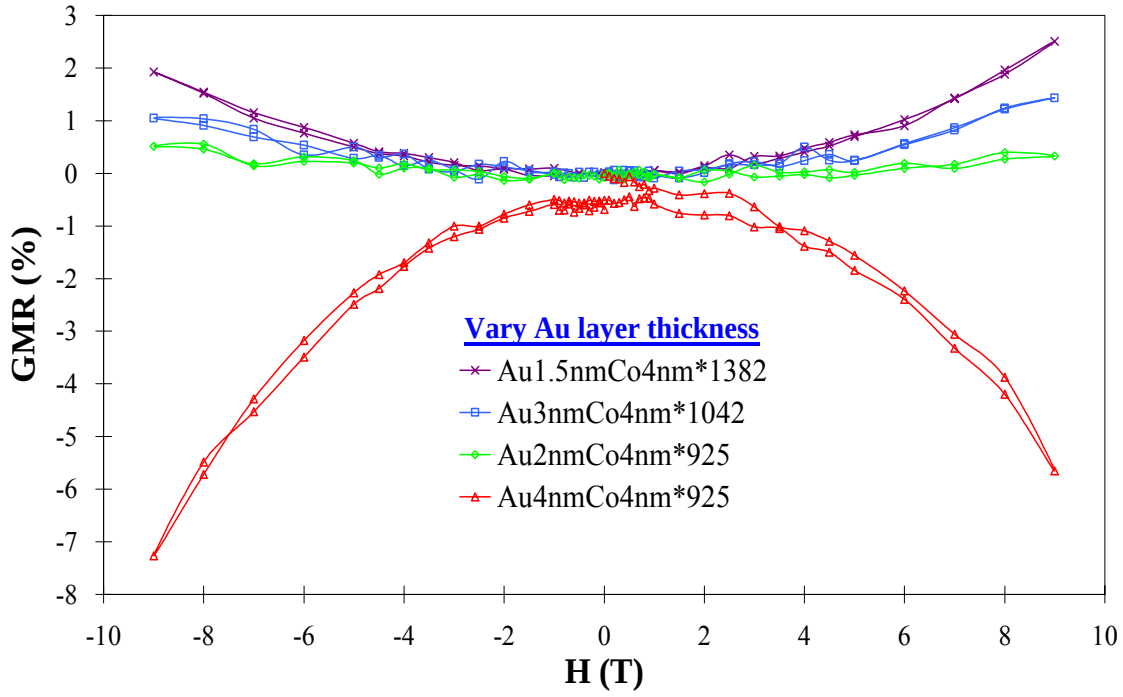

Figure 4-16 GMR results of Au/Co multilayer films on Cu foil substrate, with variable Au layer thickness

Figure 4-17 shows the maximum GMR observed at 9 T for different Au layer and Co-rich layer thicknesses. The GMR transits from a positive to negative value depending on the layer thicknesses. Both Au and Co layer thicknesses affect the GMR. The origin of GMR is due to the antiferromagnetic (AF) coupling of two adjacent ferromagnetic Co layers separated by a nonferromagnetic Au layer. When the external magnetic field is applied and increased, the resistance will decrease. The observed positive magnetoresistance may be due to a different phenomenon.

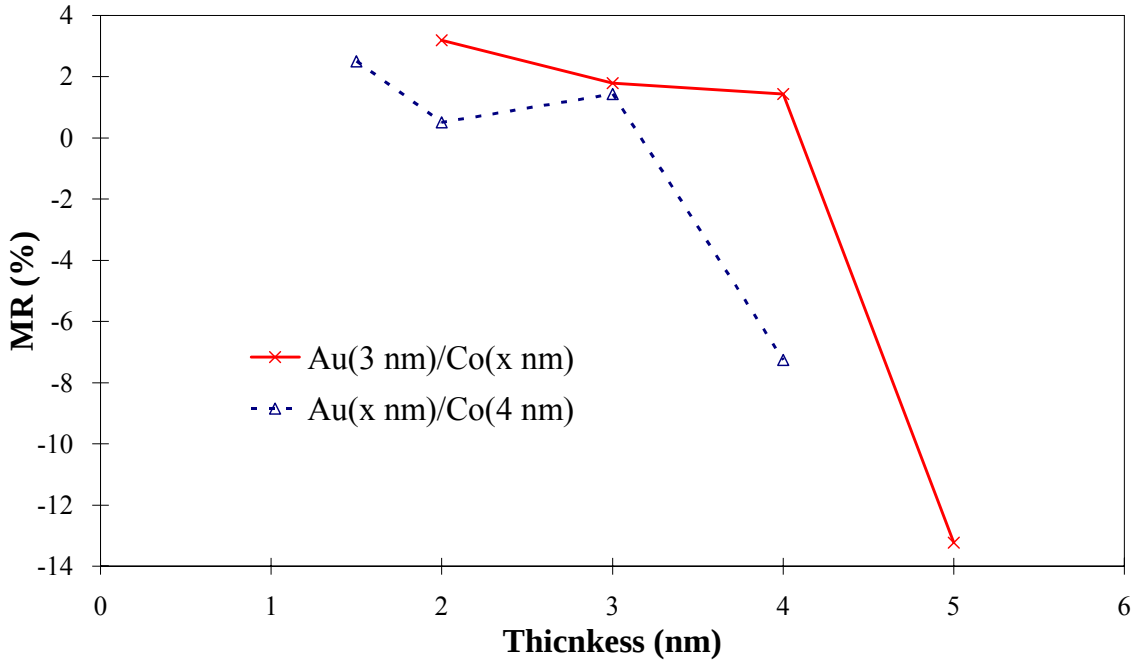

Figure 4-17 GMR variation with layer thickness

4.2.4 Nanoimprint Molds

Multilayers with layer size of a few nanometers show a larger giant magnetoresistance (GMR) property, as presented in the previous section. On the other hand, the multilayers with layer sizes of tens to hundreds of nanometers are also of great

interest in optics and electronics industries for nanolithography application.[19] Therefore, the use of the multilayer as a stamping mold on the nanoscale was explored.

AuCo alloys are well suited as a mold since the Au imparts a corrosion resistance effect while the Co gives the alloy high hardness. It is well known that gold, when electroplated with about 0.5 % cobalt, has a hardness of about four to five times that of annealed electrodeposited gold.[93] This degree of hardness cannot be achieved using any of the known metallurgical methods. It is widely believed that grain sizes of 20 to 30 nm in this material are responsible for this high degree of hardness.[94] Koch *et al.*[95] reported that hard gold can be electroplated even without any hardening additives if the bath is operated under a suitable current densities and temperature.

To fabricate a mold, the electrodeposition of the multilayers is followed by mounting the sample in an acrylic resin, cross-section cutting, cross-section polishing, and an etching step. The complete preparation procedure is shown in **Figure 4-18**. The electrodeposition of Au/Co multilayers is similar to the plating process for GMR materials, with only increasing the plating time to achieve a significantly bigger layer size. A copper rotating disk electrode (RDE), platinum anode and SCE reference electrode were used for the characterization of the electrolyte, **Figure 4-18(a)**. Galvanostatic, square-wave pulsed plating was carried out with currents of -1 mA/cm^2 for the Au layer and -100 mA/cm^2 for the Co layer with variable times. At low current density cobalt hardened gold (99.5 % Au) is deposited, while at high current density a cobalt rich alloy (98.7 % Co) is obtained. Multilayer thin films deposited onto the RDE were mounted by Buehler Sample-Kwick fast cure acrylic resin, **Figure 4-18(b)** and cut by ISOMET® Low Speed Saw to expose the cross-section, **Figure 4-18(c)** and mechanically polish the

cross-section, **Figure 4-18(d)** and then selectively etched the Co layer with $K_2Cr_2O_7$ etching solution (See **Table 4-1** for detail compositions), **Figure 4-18(e)**. Usually the etching process takes 5 to 15 minutes, according to different layer thickness. The grated nanostructures were confirmed by scanning electron microscopy (SEM).

Table 4-1 Composition of $K_2Cr_2O_7$ etching solution

Constituent	Concentration (mol/L)
$K_2Cr_2O_7$	0.0085
H_2SO_4	0.09
HCl	0.003

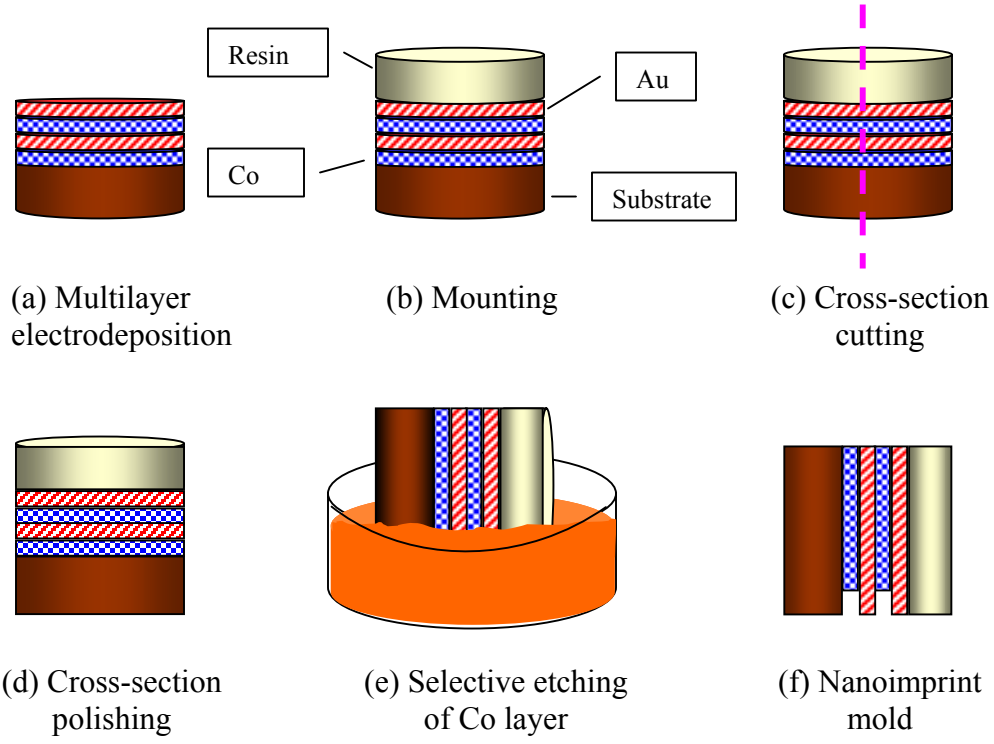

Figure 4-18 Six steps of the nanoimprint mold preparation from the Au/Co multilayers electrodeposition and then selective etching of Co layers

Scanning electron microscope (SEM) is used widely to confirm the grated nanostructures. **Figure 4-19** shows the overview of a multilayer thin film cross-section

on a copper rotating disc electrode (RDE), covered by the acrylic resin and then polished on the cross-section. It consists of three parts, Cu substrate, multilayer thin films and acrylic resin.

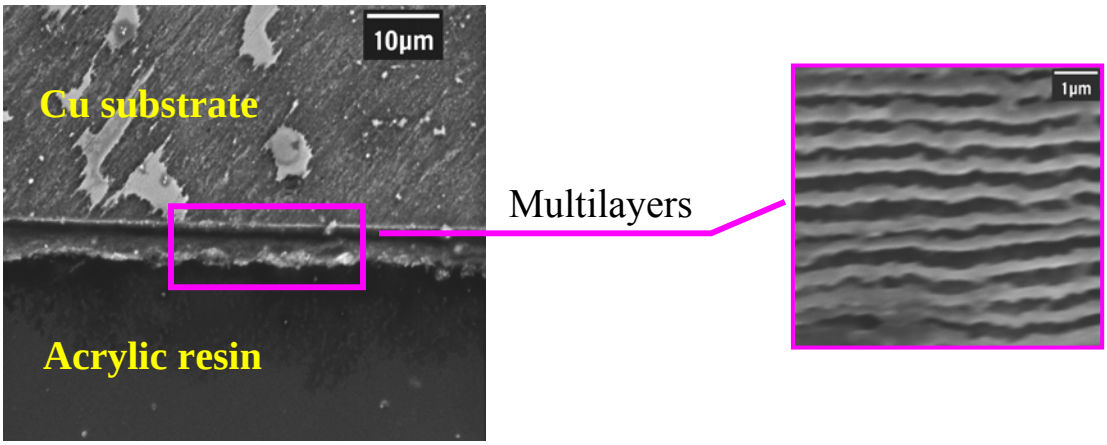

Figure 4-19 Overview of cross-section multilayers on RDE after mounting, cutting, polishing and etching

Figure 4-20 shows an example of a successfully etched Au/Co multilayer. Au layers were plated for 5,040 seconds. Using the current efficiency determined from the alloy plating, the layer size was calculated to be 200 nm, which is consistent with the light stripes in **Figure 4-20**. By using an 8-step pulse, the Co layer thicknesses were varied during plating, having a calculated size of 200, 400, 600 and 800 nm, with the plating times of 30, 60, 90 and 110 s, respectively. The dark stripes of X, Y, Z_1, Z_2 in **Figure 4-20** are corresponding to Co layers, closed to the calculated layer size.

Figure 4-21 is another example of Au/Co multilayers with uniform Au/Co layer deposition time, electrodeposited by a galvanostatic, two-step pulse plating. Au layers were plated for 5,040 seconds. The Au layer was deposited at -1 mA/cm^2 current density for 5040 minutes, resulting in a 200 nm thickness. The Co layer was deposited at -100 mA/cm^2 current density for 90 seconds, resulting in a 600 nm thickness. The layers look

fairly uniform along the direction of growth. This sample was selectively etched by the above $K_2Cr_2O_7$ etching solution for 5 minutes.

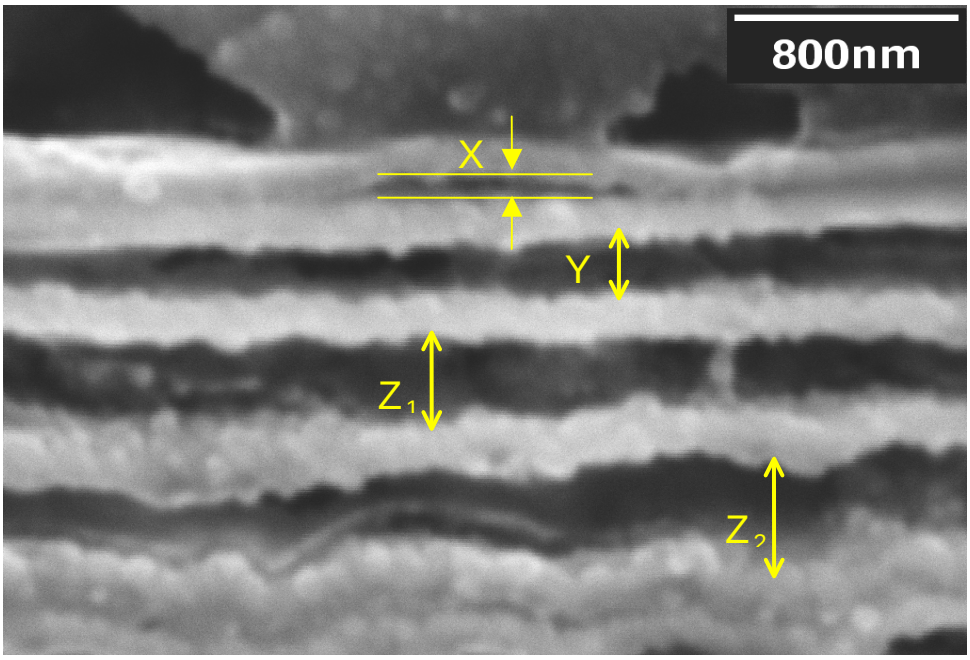

Figure 4-20 SEM micrograph of a multilayer with constant Au layer of 200 nm and variable Co layer thicknesses of 200, 400, 600 and 800 nm

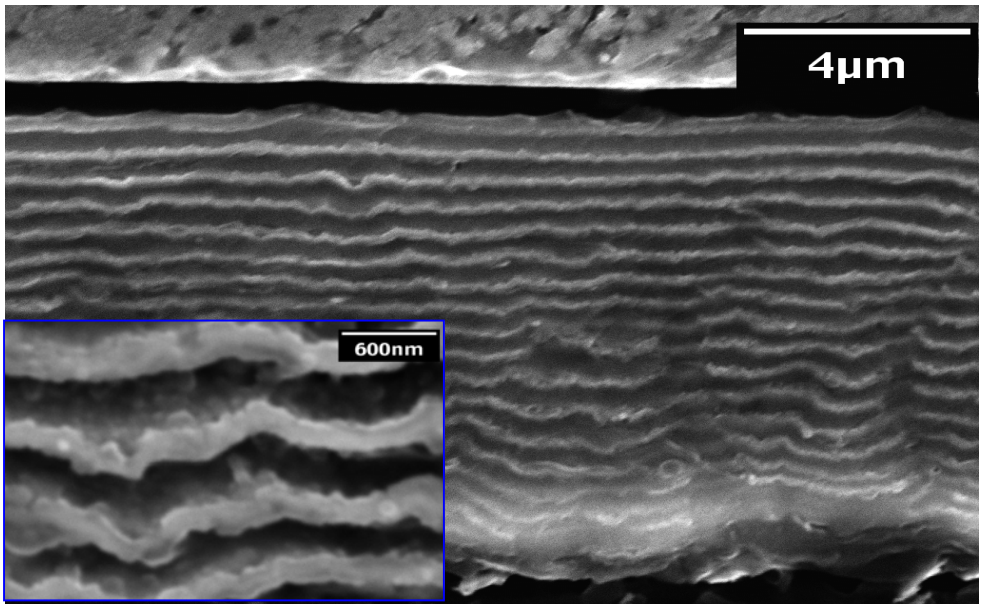

Figure 4-21 SEM micrograph of a multilayer with constant Au/Co layer thickness (Au 200 nm/Co 600nm) after etching for 5 minutes

Figure 4-22 reflects the defects of multilayer thin films on a larger scale. As shown in the circle area in **Figure 4-22**, there includes cracking of the deposit and loss of adhesion to the substrate. The bending of the multilayer thin film from a horizontal to a vertical position was due to the process of cross-section cutting by the diamond saw. The ISOMET® low speed saw is not sharp enough to cut the rotating disk electrode completely. The cracking of the deposit and loss of adhesion to the substrate maybe results from internal stress, and the large lattice mismatch with the substrate. Codeposition of hydrogen can also cause cracks in a deposit. A tensile macrostress can develop when hydrogen diffuses onto the substrate or previously deposited layers causing them to expand, or when hydrogen diffuses out of a layer of the deposit allowing it to shrink. In some circumstances, when micropores form during deposition, hydrogen then diffuses into them causing them to expand resulting in a compressive macrostress. Improving the current efficiency and removing the codeposition of hydrogen is an effective way to ameliorate the multilayer thin film structures.

Additionally, in the mounting process of the sample, the electrodeposited thin film along with the copper substrate was first embedded in a fast hardening resin (Buehler Sample-Kwick fast cure acrylic resin, powder and liquid). After mixing the power and liquid in a 2:3 ratio, the autopolymerization reactions occur and the temperature increased. The high temperature may have caused each Co layer, Au layer and copper substrate to expand before etching since the coefficient of thermal expansion (CTE) differs for Cu, Co, Au and acrylic resin. The coefficient of thermal expansion (linear) is defined as the change in length per unit length of material for a one degree Centigrade change in temperature. Among those four materials, acrylic resin has the biggest CTE, which is

around 5 times that of metals. This may also contribute to the deformation of layers and delamination of the multilayer from the copper substrate.

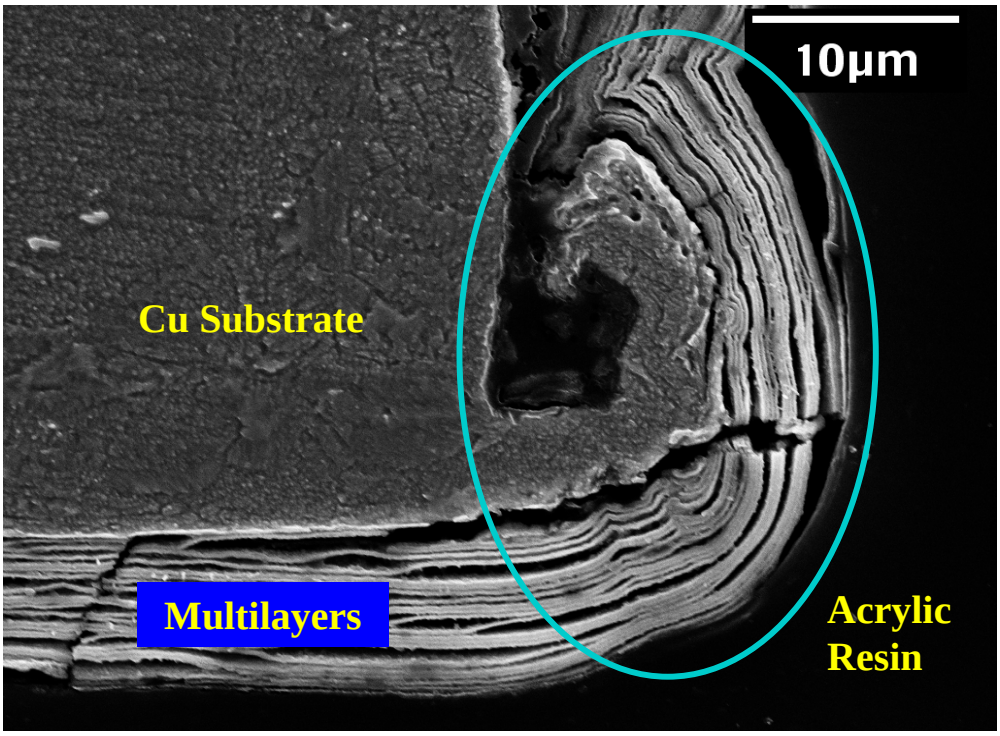

Figure 4-22 SEM micrograph of the distortion of multilayer thin films

Table 4-2 Coefficient of linear thermal expansion (CTE)

Material	CET (x10^{-6}/^{o}C)	Temp. Range (^{o}C)	Reference
Cu	16.5	25	http://www.efunda.com
Co	13.0	25	http://www.efunda.com
Au	14.4	20-50	Craig[96]
Acrylic resin	76	5- 37	Chandler *et al.*[97]

4.3 Nanowires Electrodeposition

In this study, two electroplating methods were employed, including galvanostatic (constant current) control and potentiostatic (constant potential) control. By controlling

the potential, the desired alloy composition can be controlled more precisely and the layer interface of the multilayered structure becomes sharper. But the layer thicknesses are not constant, which is undesired. On the contrary, when applying constant current for same plating time, the same amount of charge is applied, and more uniform layer thickness can be obtained, if the current efficiency is constant.

4.3.1 Au/Co Multilayer Nanowire - Galvanostatic Control

Galvanostatic control electroplating was applied to obtain multilayered nanowire structures with uniform layer thickness. The proper current densities for Au and Co electrodeposition were determined from a polarization curve in a stagnant electrode, as shown in **Figure 4-23**. The sweep rate was 2 mV/s, the sweep range was from the open circuit potential (OCP) to -3 V vs SCE. The membrane used was AAO with a pore size of 0.02 μm, and the Au-Co electrolyte composition was the same as used previously in **Table 3-2**.

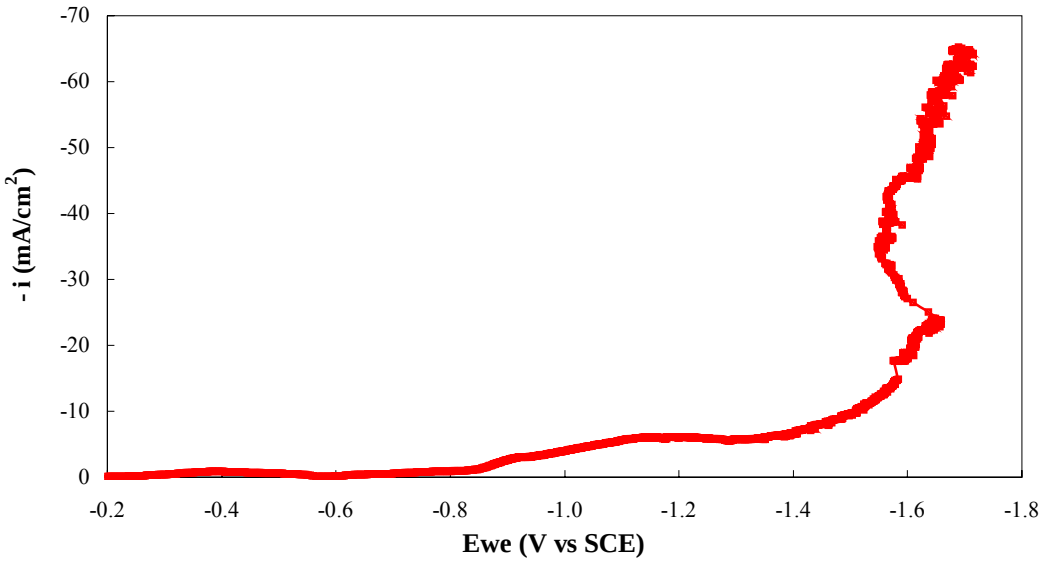

Figure 4-23 Polarization curve of Au-Co electrolyte (Table 3-2)

The conditions for the two-step galvanostatic pulse plating were -1.767 mA for 180 s for the Au layer and -176.7 mA for 3 s for the Co layer. The electrode area exposed was 1.767 cm^2, including exposed and unexposed regions. The total cycle number is 100. The membrane template was anodic alumina oxide (AAO) with a pore size of 0.02 μm.

Figure 4-24 presents two SEM micrographs of Au/Co multilayer nanowires observed at different angles. From the SEM image, the sputtered Au layer thickness was estimated to be 20 μm; the length of the nanowires was about 4.5 μm. The diameter of each nanowire was around 350 nm, which is much bigger than the reported manufacture specification of 20 nm. The reason can be found from **Figure 4-25**.

Figure 4-25 presents a SEM micrograph of AAO membrane with empty pores. The average pore size ranges from 200 to 400 nm, which is much bigger than the manufacture specification of 20 nm. As reported by Huang *et al.*,[98] in some nanowires, bifurcating structures were observed at the bottom of the wire. A sketch of the pore structure is shown in **Figure 4-26**. On one end the pore diameter is 200 – 400 nm while at the other end the pores are comparable to the manufactures specifications.

After examination of the nanowire structure by SEM, the transmission electron microscope (TEM) was employed to confirm the multilayer structure in each nanowire, operated in bright field. **Figure 4-27** clearly shows the multilayer structure. The bright layer is the Co-rich alloy layer and the dark layer is the Au layer. The layer thickness estimated from the TEM image is 15 nm for Co and 25 nm for Au, with a bilayer thickness of 40 nm, which is close to the calculated layer size.

(a)

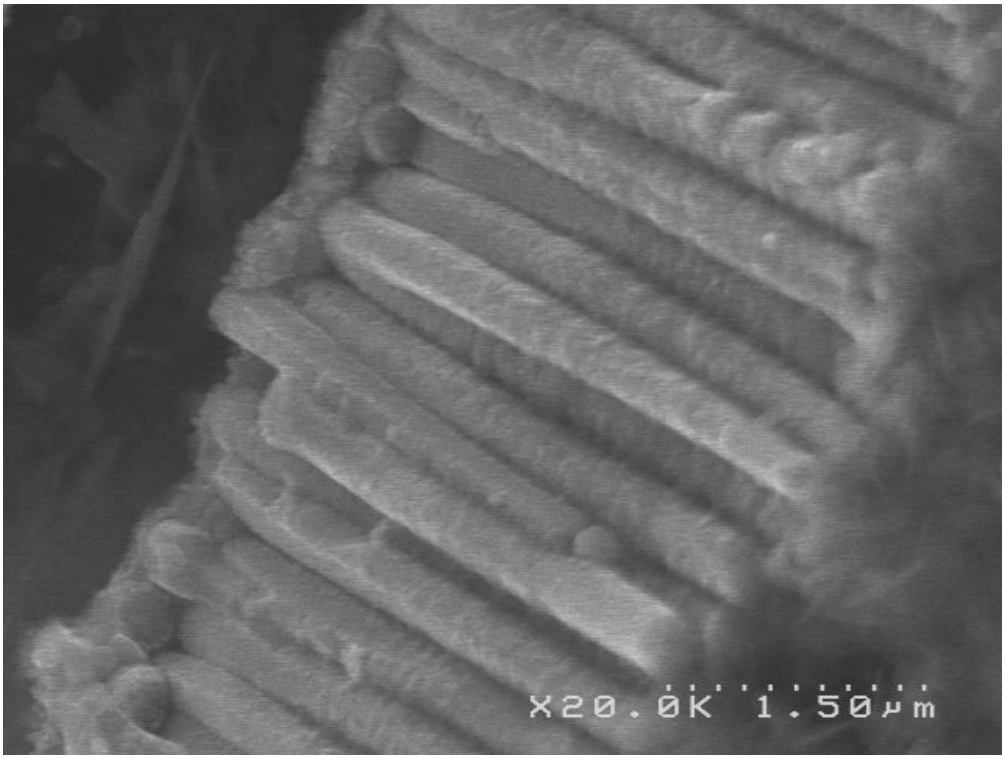

(b)

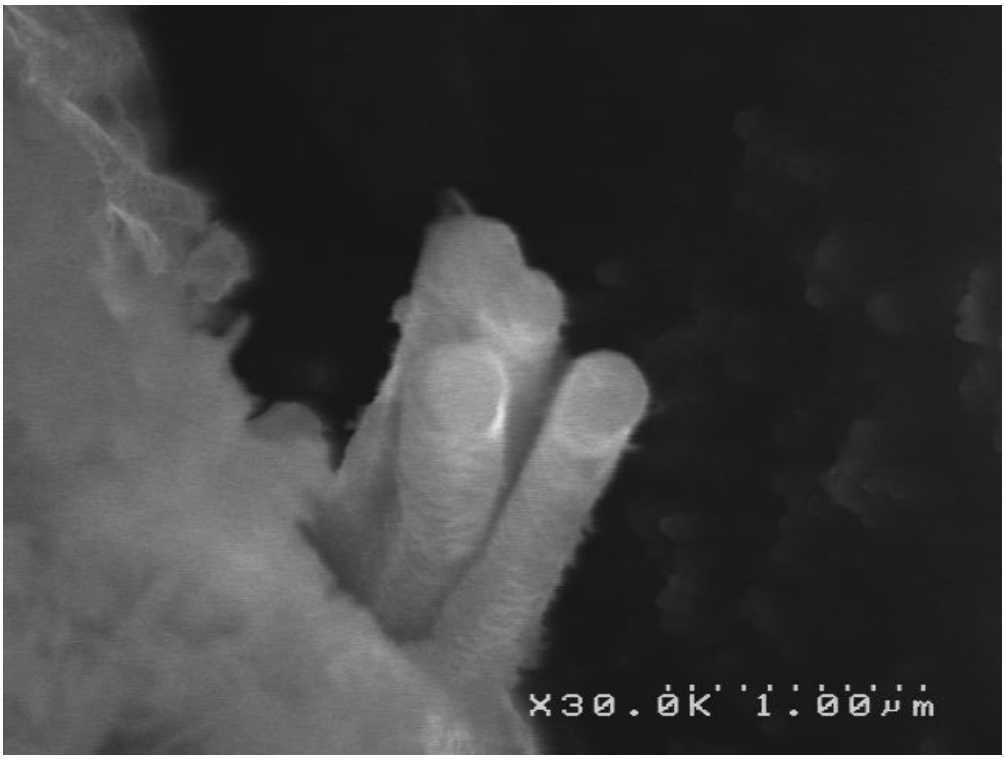

Figure 4-24 SEM micrograph of Au/Co multilayer nanowires at different angles

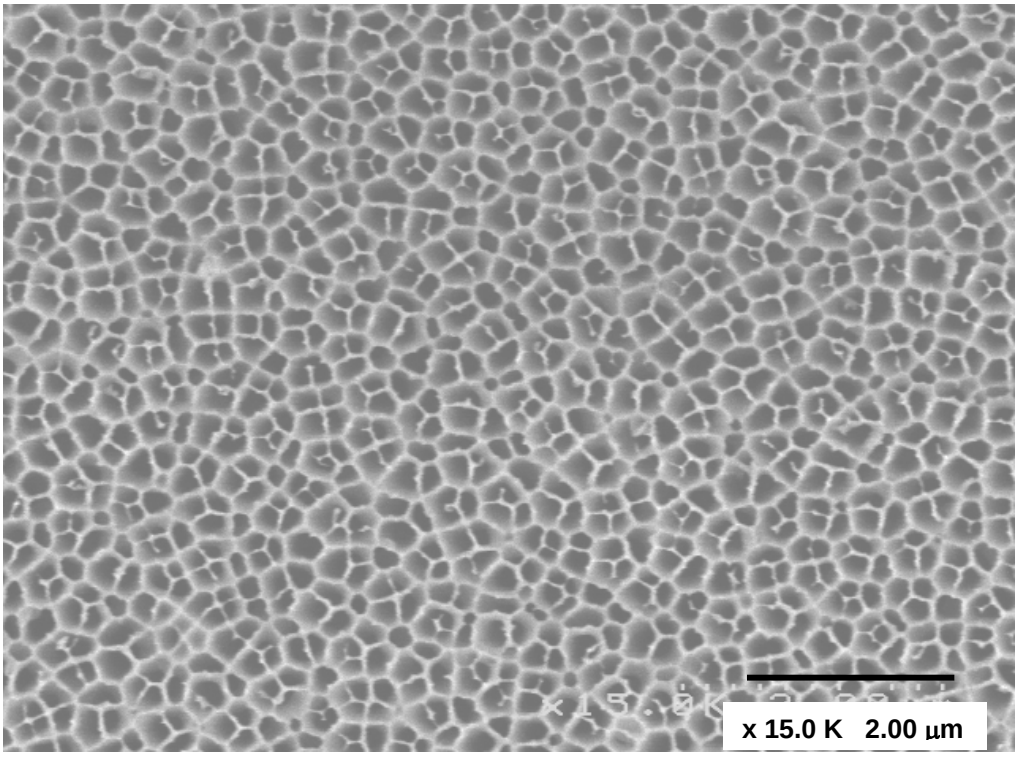

Figure 4-25 SEM micrograph reflects the irregular distribution of empty pore size of AAO membrane with pore size of 0.02 µm

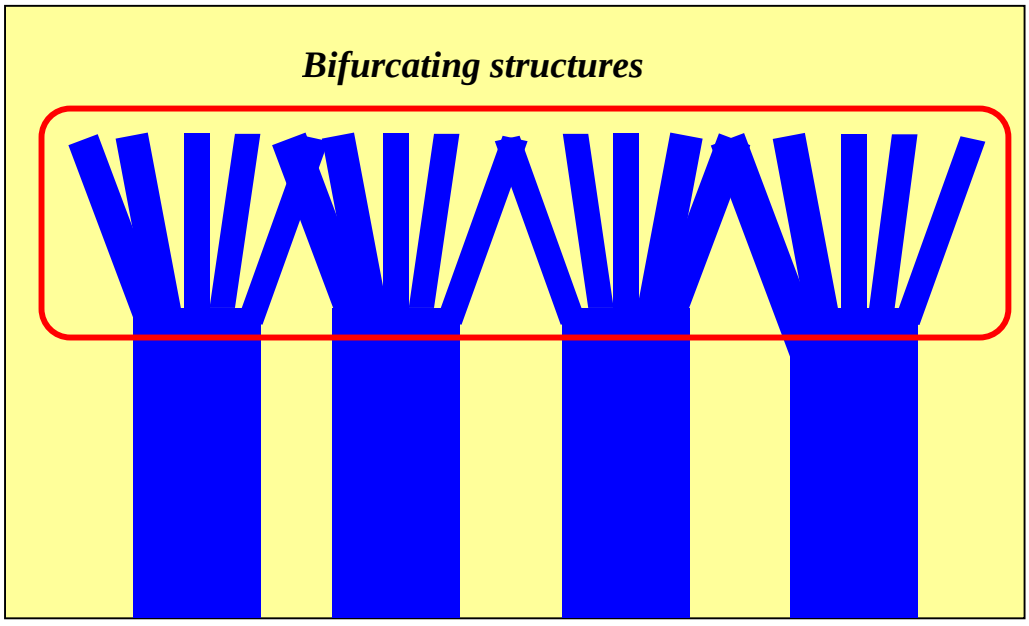

Figure 4-26 Schematic illustration of bifurcating structures in AAO membrane

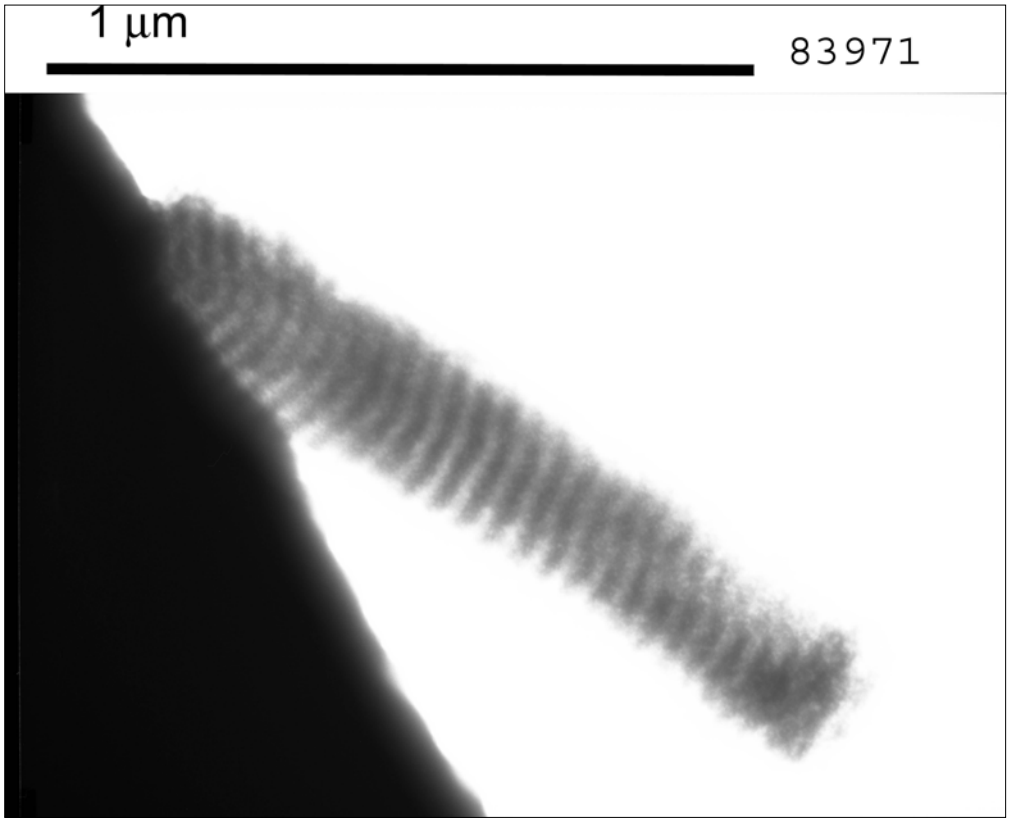

Figure 4-27 TEM bright field image of a multilayer structure

4.3.2 Au/Co Multilayer Nanowire - Potentiostatic Control

Potentiostatic electroplating or constant potential electroplating is another way to electrodeposit materials. The potentials for Au and Co electrodeposition were determined from the polarization curve in **Figure 4-28**, in which the potential was not corrected for ohmic drop. The Au-Co electrolyte composition is same to **Table 3-2**. The sweep rate was 2 mV/s, the sweep range was the same as in the previous section and the membrane used was AAO membrane with pore size of 0.2 µm, a larger pore size than in the galvanostatic control.

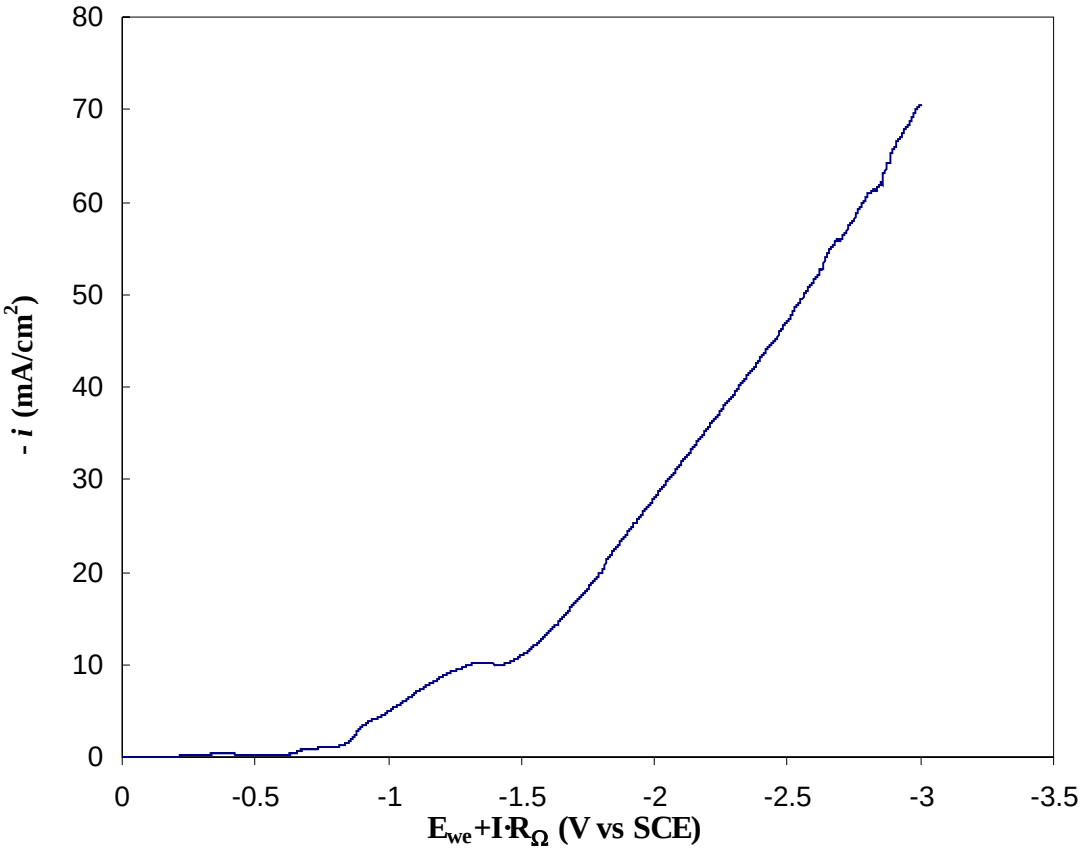

Figure 4-28 Polarization curve of Au-Co electrolyte (Table 3-2)

From the above polarization curve, two potentials were chosen: -0.7 V for the Au electrodeposition and -1.3 V for the cobalt electrodeposition. Each of them is lower than the potential where the limiting currents are reached, respectively, to minimize the side reactions. The Au layers were plated at -0.7 V for 180 seconds and the Co layers were plated at -1.3 V for 3 seconds. The total cycle number is 100.

Figure 4-29 show two SEM micrographs of Au/Co multilayered nanowires in different magnification scales.

SEM micrograph and the EDS spectra of the nanowires are shown in **Figure 4-30**. Because the nanowires were not fully grown out of the micro pores, their lengths are much smaller than the membrane thickness of 60 μm. The diameter of each nanowire was

around 316 nm. In **Figure 4-30**, the upper right SEM image is the area that was used to obtain composition. In the spectra below, the Al and Cu elements come from the substrate holder for SEM imaging.

(a)

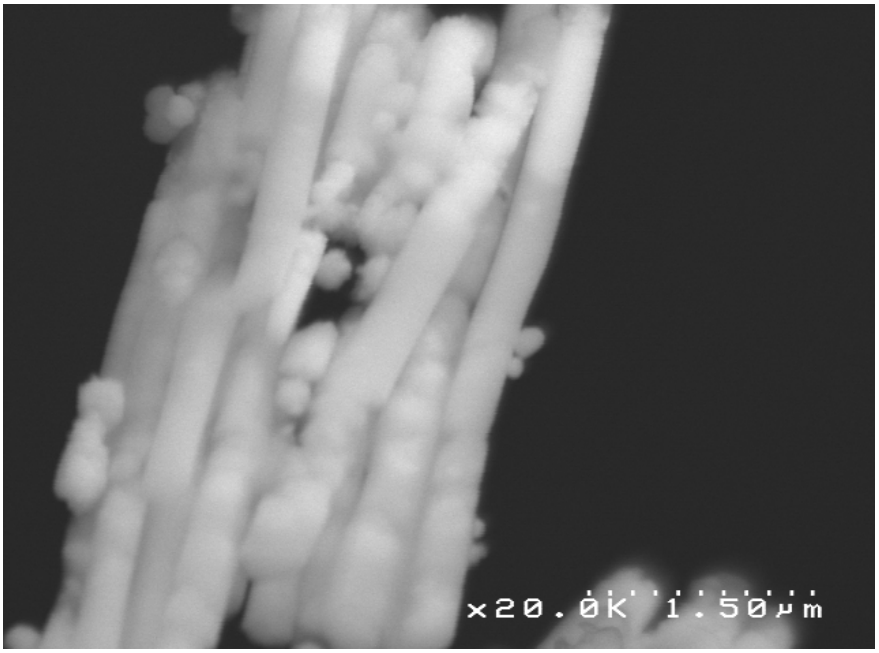

(b)

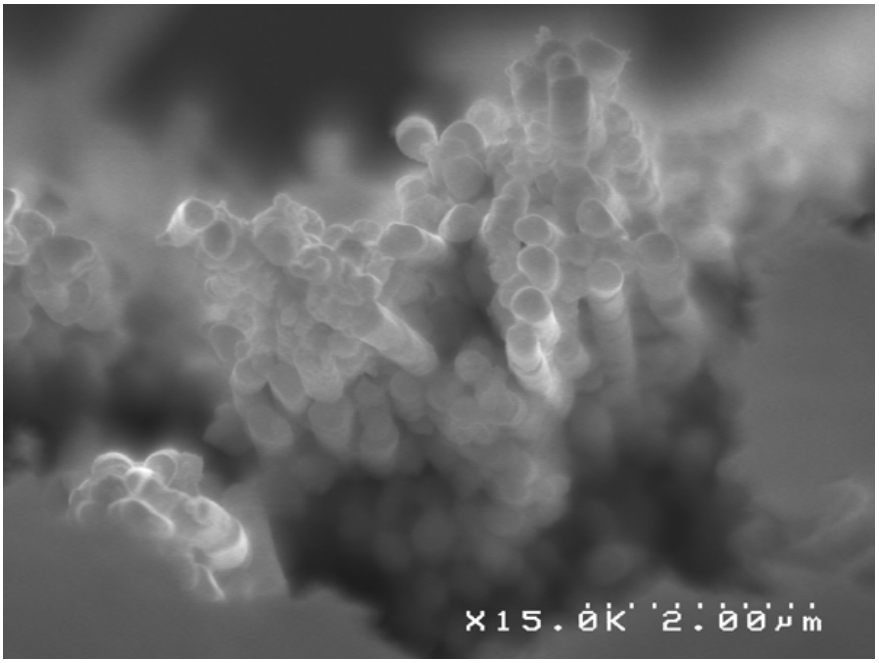

Figure 4-29 Au/Co multilayered nanowires fabricated by potentiostatic pulse plating

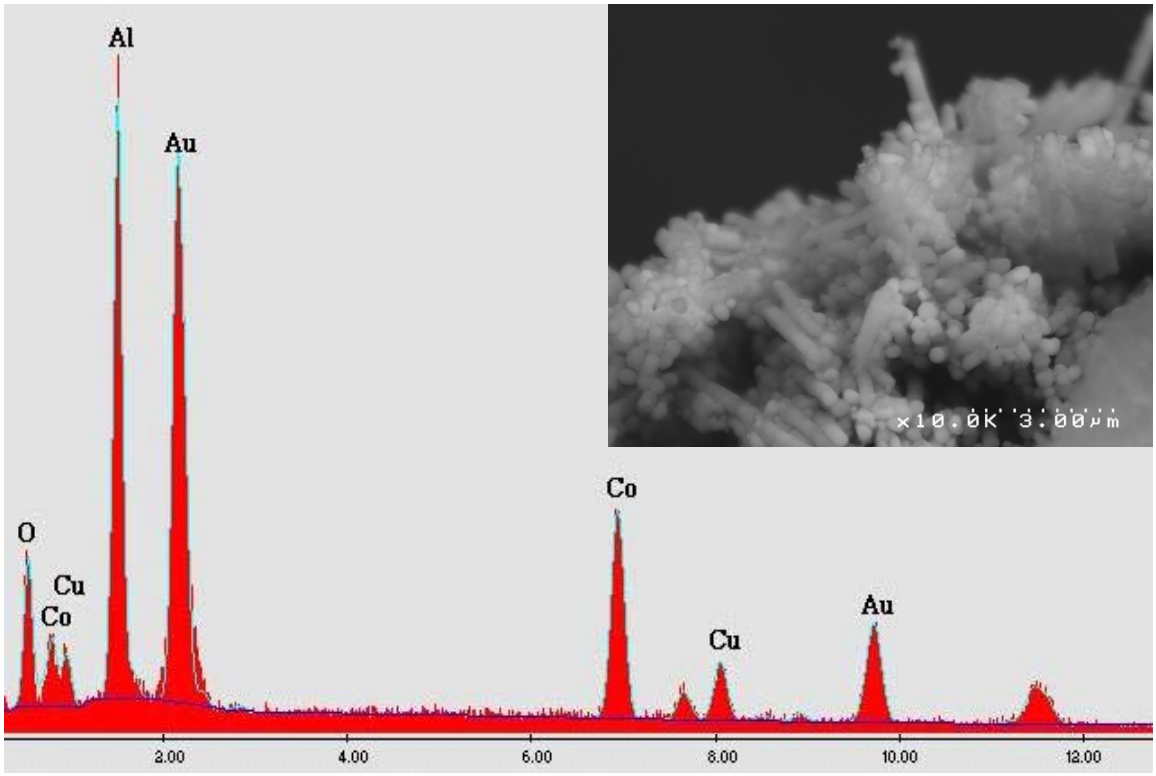

Figure 4-30 EDS spectra of Au/Co multilayered nanowires

Figure 4-31 shows the bright field TEM image of the previously described nanowire. Unlike the nanowire in **Figure 4-27**, there is no clear layer in this nanowire fabricated by potentiostatic electrodeposition. The possible reason could be that the potentials used for Au and Co electrodeposition are not separated far enough to make disparate layers.

Due to the unique configuration of large aspect ratio, the GMR property of nanowires can be easily measured in a current perpendicular to the layer configuration (CPP GMR). Compared with the current-in-plane GMR, current-perpendicular-to-plane GMR has been proven to show larger magnetoresistance change in Co/Cu[10] system, CoNi/Cu[99] and NiFe/Cu[15] systems, future work will focus on testing the Au/Co multilayer nanowires for their CPP GMR property

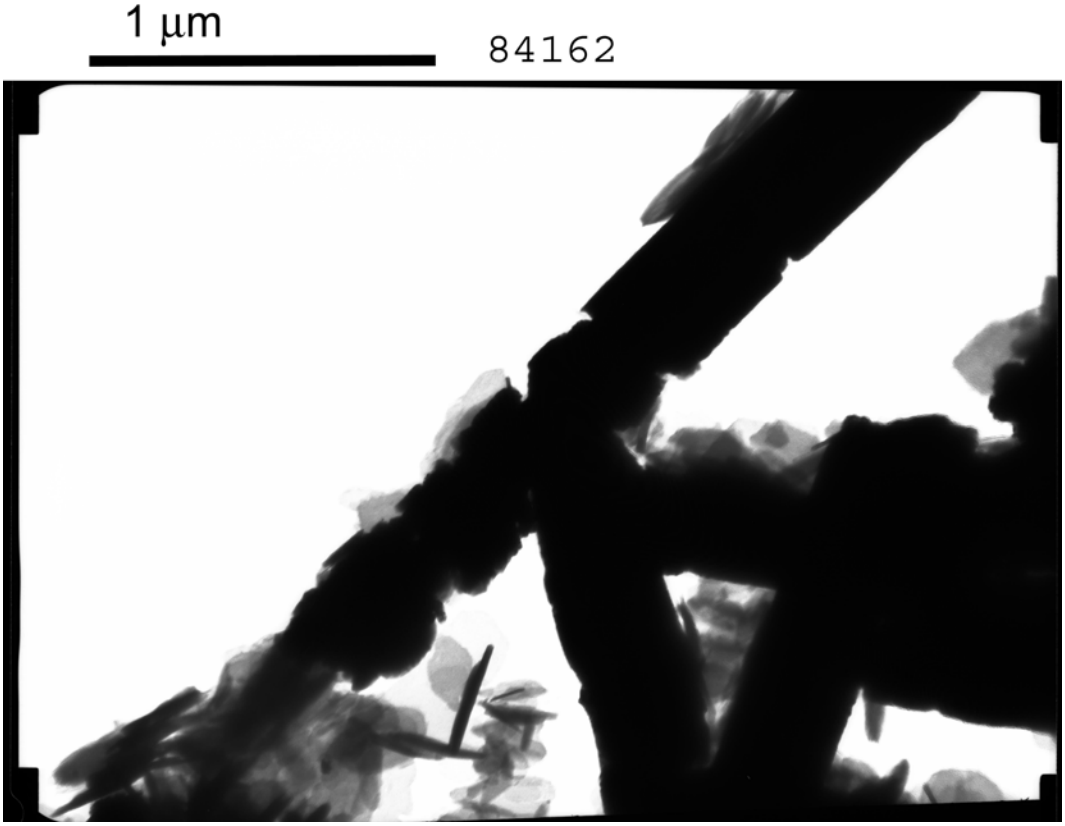

Figure 4- 31 TEM bright field image of a nanowire

4.3.3 AuCo Alloy Nanotube

Figure 4-32 shows a SEM imagine of the nanometric tube-type structure, which was electrodeposited unexpectedly when trying to electroplate AuCo alloy nanowires on a recessed rotating disk electrode (RRDE) by using polycarbonate membrane. The Au-rich alloy nanotubes were plated at constant current of -1.767 mA for 20 hours with rotating rate of 1600 rpm. The membrane pore size is 0.8 μm and membrane thickness is around 60 μm and the electrode area is only 0.0706 cm^2. **Figure 4-32** shows the estimated tube diameter is around 645 nm, which is smaller than the pore size of 800 nm. Similar co-rich alloy nanotubes were also obtained.

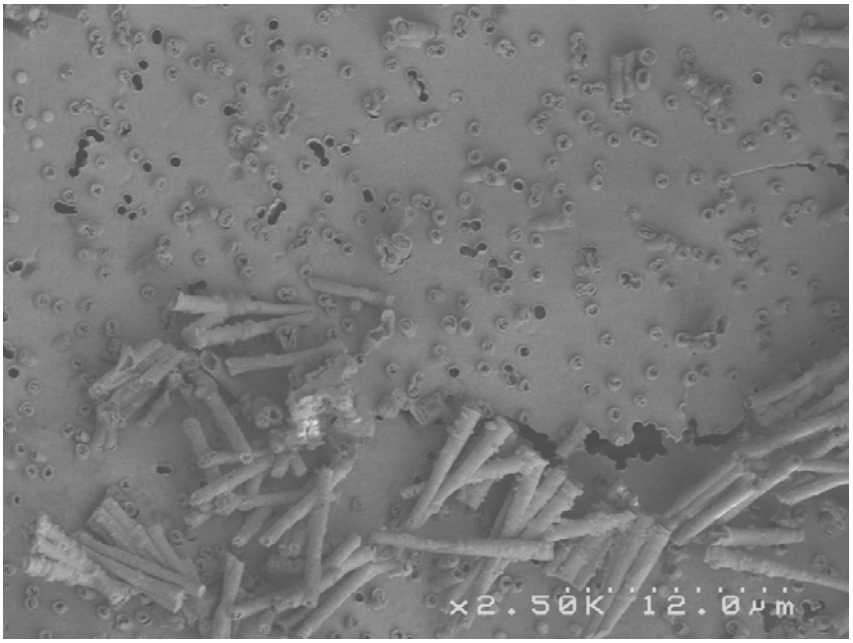

Figure 4- 32 SEM imagine of Au-rich alloy nanotubes

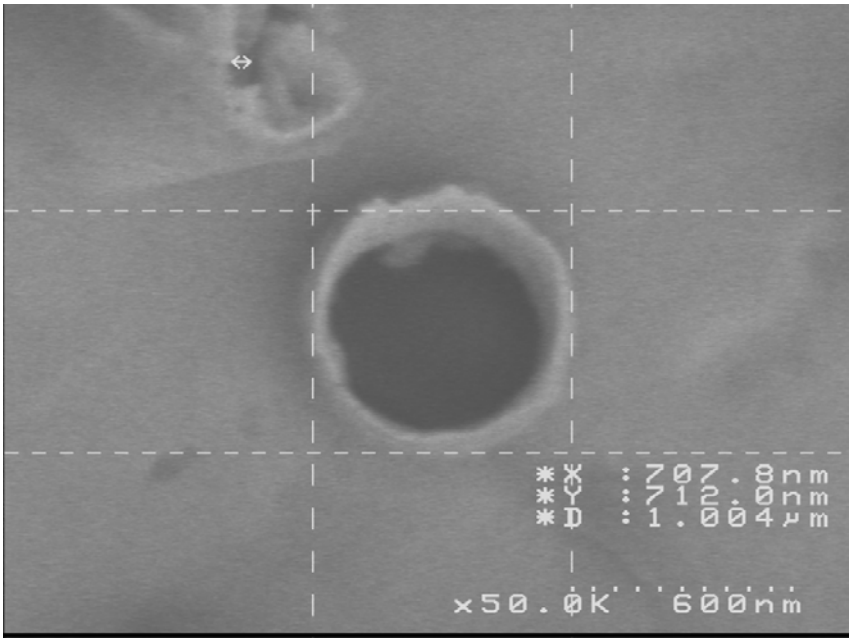

Figure 4- 33 A higher magnification of the Au-rich nanotube

The reason for the growth of nanotubes but not nanowires from recessed rotating disk electrode might be explained in this way: at the beginning of electrodeposition of Au/Co elements, the side reaction cannot be avoided, such as

$2\ H^+ + 2\ e^- \rightarrow H_2$ **Equation 4-1**

and

$2\ H_2O\ +\ 2\ e^-\ \rightarrow\ H_2\ +\ 2OH^-$ **Equation 4-2**

Because the recessed rotating disk electrode always faces down, the tiny hydrogen bubbles could not diffuse out of the micro pores freely, but accumulated and bubbles coalesced. Blocking by bubbles prevents the electrolyte from reaching the center of the micro pores resulting in only tube-shaped structures.

CHAPTER 5 CONCLUSIONS

In this study, a process of using a non-cyanide single bath to electrodeposit AuCo alloys and multilayers was characterized. The precious metal (Au) was kept at a very low concentration and the less precious metal (Co) was kept at much higher concentration. In such a way, pure Au was electroplated at lower current density and the Co-rich alloy was achieved at higher current density. Different applications were explored, including multilayer thin films with GMR property, nanoimprint molds, and multilayer nanowires. The main results and conclusions are summarized:

(1) During AuCo deposition, increasing citric acid concentration shifted the Co reaction rate to more negative potentials and increased the side reaction rates, which, consequently, lowers the current efficiency. But increasing citric acid concentration did not significantly affect the Au reaction.

(2) In AuCo electroplating, even though pH does not influence the Au reaction rate, a higher pH does shift the Co reaction rate to a more negative potential, resulting in a lower current efficiency. However, lower pH values less than 5 result in Au precipitation.

(3) The citric acid concentration of 0.67 M, pH of 6.15 and the Au concentration of 0.00042 M were chosen as the final electrolyte composition for multilayer plating. The Au content reaches 99.5 (wt %) when the current density is lower than -1 mA/cm^2, and the Co content is higher than 98.7 (wt %) when the current density is higher than -100 mA/cm^2.

Au/Co nanometric multilayers exhibiting GMR were electrodeposited, and large GMR (> -13 %) was found when the films were deposited on (100) Cu. The GMR changes from a positive to negative value depending on the layer thicknesses. To the best of the author's knowledge, this is the first demonstration of a GMR in an electrodeposited Au/Co system.

(4) AuCo alloys were explored as a nanoimprint mold since the Au imparts a corrosion resistance effect while the Co gives the alloy high hardness. Galvanostatic pulse plating was used to electroplate the Au/Co multilayers and the $K_2Cr_2O_7$ solution was used to selectively etching co layers. The grated nanostructures were confirmed by scanning electron microscopy (SEM).

(5) Electrodeposition of Au/Co multilayer nanowires was also developed in this study. Both AAO and polycarbonate membranes were used as templates. Galvanostatic and potentiostatic controls were test for the nanowire electrodeposition. A nanowire of 15 nm for Co and 25 nm for Au, which is closed to the calculated layer size, were fabricated by galvanostatic pulse plating and confirmed by TEM analysis.

The future work will focus on testing the Au/Co multilayer nanowires for their CPP GMR property, and then, as a final goal, fabricating GMR-Biosensors.

REFERENCES

1. W. Chu, H. I. Smith, S. A. Rishton, D. P. Kern, and M. L. Schattenburg, *Fabrication of 50 nm line-and-space x-ray masks in thick Au using a 50 keV electron beam system.* Journal of Vacuum Science and Technology - B, 1992. **10**: p. 118.

2. W. J. Daukler, D. J. Resnick, W. A. Johnson, and A. W. Yanof, *A new operating regime for electroplating the gold absorber on x-ray masks.* Microelectronic Engineering, 1994. **23**: p. 235.

3. J. Jasper, D. Shiels, European Semiconductor, 2000. **22**: p. 86.

4. Y. Okinaka, M. Hoshino, Gold Bulletin, 1998. **31**: p. 3.

5. K. M. H. Lenssen, D. J. Adelerhof, H. J. Gassen, A. E. T. Kuiper, G. H. J. Somers, and Jbad van Zon, *Robust giant magnetoresistance sensors.* Sensors And Actuators A-Physical, 2000. **85**(1-3): p. 1-8.

6. E. Velu, C. Dupas, D, Renard, J. P. Renard, J. Seiden, *Enhanced magnetoresistance of ultrathin (Au / Co)n multilayers with perpendicular anisotropy.* Physical Review B, 1998. **37**: p. 668.

7. A. Hutten, D. Sudfeld, K. Wojczykowski, P. Jutzi, G. Reiss, Journal of Magnetism and Magnetic Materials, 2003. **262**: p. 23-31.

8. A. Yamada, T Houga, and Y Ueda, *Magnetism and magnetoresistance of Co/Cu multilayer films produced by pulse control electrodeposition method.* JOURNAL OF MAGNETISM AND MAGNETIC MATERIALS, 2002. **239**(1-3): p. 272-275.

9. A. Blondel, B Doudin, and JP Ansermet, *Comparative study of the magnetoresistance of electrodeposited Co/Cu multilayered nanowires made by single and dual bath techniques.* JOURNAL OF MAGNETISM AND MAGNETIC MATERIALS, 1997. **165**(1-3): p. 34-37.

10. L. Piraux, J. M. George, J. F. Despres, C. Leroy, E. Ferain, R. Legras, K. Ounadjela, and A. Fert, Applied Physics Letters, 1994. **65**: p. 2484.
11. N.V. Myung, B.Y. Yoo, M. Schwartz, K. Nobe, Electrochemical Society Proceedings, 2000. **29**: p. 154.

12. L. Piraux, S. Dubois, A. Fert, Journal of Magnetism and Magnetic Materials, 1996. **159**: p. 287.

13. W. P. Pratt, Jr., S. F. Lee, G. M. Slaughter, R. Loloee, P. A. Schroeder and J. Bass, Physics Review Letters, 1991. **66**: p. 3060.

14. S. Dubois, C. Marchal, J. M. Beuken, L. Piraux, J. L. Duvail, A. Fert, J. M. George, J. L. Maurice, Applied Physics Letters, 1997. **70**: p. 396.

15. S. Dubois, J. M. Beuken, L. Piraux, J. L. Duvail, A. Fert, J. M. George and J. L. Maurice, Journal of Magnetism and Magnetic Materials, 1997. **165**: p. 30.

16. A. Blondel, *et al.*, *Giant magnetoresistance of nanowires of multilayers.* Applied Physics Letters, 1994. **65**(23): p. 3019.

17. S. Valizadeh, L. Hultman, J - M George, P. Leisner, Advanced Functional Materials, 2002. **12**(11-12): p. 766.

18. S. Valizadeh, E.B. Svedberg, and P. Leisner, Journal of Applied Electrochemistry, 2002. **32**: p. 97-104.

19. Stephen Y. Chou, *Big Future for Tiny Dies. Nanoimprint Lithography promises a Revolutionary Advance in Nanotechnology.* Science Spectra, 1998. **10**: p. 38.

20. J. Seekamp, S. Zankovych, A. H. Helfer, P. Maury, C. M. S. torres, G. Bottger, C. Liguda, M. Eich, B. Heidari, L. Montelius, J. Ahopelto, Nanotechnology, 2002. **13**: p. 581.

21. Che-Yih Lim, Q. Huang, X. Xie, A. Safir, S.A. Harfenist, R. Cohn, E.J. Podlaha, Journal of Applied Electrochemistry, 2004. **34**(8): p. 857.

22. http://www.epa.gov, 2004.

23. http://www.epa.gov, *Consumer Factsheet on: CYANIDE.* 2004.

24. T. A. Green, M.-J. Liew, S. Roy, *Electrodeposition of Gold from a Thiosulfate-Sulfate Bath for Microelectronic Application.* Journal of The Electrochemical Society, 2003. **150**(3): p. C104.

25. A. M. Sullivan, P. A. Kohl, Journal of The Electrochemical Society, 1997. **144**: p. 1686.

26. J. Traut, J. Wright, J. Williams, Plating and Surface Finishing, 1990. **77**: p. 49.

27. H. Honma, K. Hagiwara, Journal of The Electrochemical Society, 1995. **142**: p. 81.

28. K. Kosaki, M. Matsuoka, Y. Seiwa, S. Orisaka, K. Nishitani, M. Otsubo, *Electrochemical Microfabrication*, in *Electrochemical Society Proceeding Series*, K. Sheppard M. Datta, D. Snyder, Editor. 1992: Pennington, NJ. p. 317.

29. Y. Okinaka, T. Osaka, *Advances in Electrochemical Science and Engineering*, C. Tobias H. Gerischer, Editor. 1994, VCH Publishing. p. 55.

30. T. Osaka, A. Kodera, T. Misato, T. Homma, Y. Okinaka and O. Yoshioka, Journal of The Electrochemical Society, 1997. **144**: p. 3462.

31. J. H. Lindsay, H. J. Read, *Some properties of Electrodeposited Cobalt.* Plating, 1970. **57**: p. 497.

32. A. Brebber, *Ph. D. Dissertation*. 1939, University of Maryland.

33. Yahalom, Zadok, Journal of Materials Science, 1987. **22**: p. 499.

34. Mordechay Schlesinger, Milan Paunovic, *Modern Electroplating*. 2000. p. 28.

35. G. Millazzo, S. Caroli, *Tables of Standard Electrode Petentials*. 1978, New York: Wiley.

36. Y. Okinaka, *EAST Report 1991: Precious Metals in Modern Technologies and Applicatiions*. 1992, Schwabisch Gmund: Germany. p. 8-18.

37. P. Wilkinson, Gold Bulletin, 1986. **19**: p. 21.

38. I. Pouradier, M. C. Gadet, Journal of Physical Chemistry, 1969. **66**: p. 109.
39. H. Shindo, H. Honma, Proceedings of 84th Conference of Surface Finishing Society of Japan, 1991: p. 163.

40. Mordechay Schlesinger, Milan Paunovic, *Modern Electroplating*. 2000. p. 676.

41. S. Valizadeh, J.M. George, P. Leisner, L. Hultman, Thin Solid Films, 2002. **402**: p. 262-171.

42. S. Valezadeh, G. Holmbom, P. Leisner, Surface and Coating Techonology, 1998. **105**: p. 213-217.

43. L. Cagnon, A. Gundel, T. Devolder, A. Morrone, C. Chappert, J. E. Schmidt, and P. Allongue, Applied Surface Science, 2000. **164**: p. 22-28.

44. L. Cagnon, T. Devolder, R. Cortes, A. Morrone, J. Schmidt, C. Chappert, P. Allongue, *Enhanced interface perpendicular magnetic anisotropy in electrodeposited Co/Au(111) layers.* Physical Review B, 2001. **63**: p. 104419.

45. M. Kleinert, H.-F. Waibel, G.E. Engelmann, H. Martin, D.M. Holb, Electrochemica Acta, 2001. **46**: p. 3129-3136.

46. A. Gundel, L. Cagnon, C. Gomes, A. Morrone, J. Schmidt and P. Allongue, Physical Chemistry Chemical Physics, 2001. **3**: p. 3330-3335.

47. J.J. Kelly, N. Yang, T. Headley, and J. Hachman, Journal of The Electrochemical Society, 2003. **150**(6): p. C445-C450.

48. R. De Doncker, J. Vanhumbeeck, Transactions of the Institute of Metal Finishing, 1985. **63**(2): p. 59.

49. D. Kahn, AMP Journal of Technology, 1991. **1**: p. 43.

50. M. N. Baibich, J. M. Broto, A. Fert, F. Nguyen Van Dau, F. Petroff, P.Etienne, G. Creuzet, A. Friederich, and J. Chazelas, *Giant Magnetoresistance of (001)Fe/(001)Cr magnetic superlattices.* Physical Review Letters, 1988. **61**: p. 2472.

51. C. A. Ross, *Electrodepositon multilayer thin films.* Annual Review of Materials Science, 1994: p. 159.

52. Schwarzacher W, D. S. Lashmore, *Giant magnetoresistance in elctrodeposited films.* Transactions on Magnetics, 1996. **32**(4): p. 3133.

53. S. Tumanski, *Thin film magnetoresistivity sensors.* 2001: p. 1-4.

54. J. E. Lenz, *A review of magnetic sensors.* Proceeding of The IEEE, 1990. **69**(20): p. 973.

55. H. Ehrenreich, F. Spaepen, Solid State Physics, 2001. **56**: p. 6.

56. E.Y. Tsymbal, D.G. Pettifor, *Perspectives of Giant Magnetoresistance.* Solid State Physics, 2001. **56**: p. 113-237.

57. G. P. Heydon, S R Hoon, A N Farley, S L Tomlinson, M S Valera, K Attenborough and W Schwarzacher, *Magnetic properties of electrodeposited nanowires.* Journal of Physics D: Applied Physics, 1997. **30**: p. 1083.

58. B. Dieny, V.S. Speriosu, S.S.P. Parkin, B.A. Gurney, D.R. Wilhoit, D. Mauri, Physical Review B, 1991. **43**: p. 1297.

59. M.R. Khan, C.S.L. Chun, G.P. Felcher, M. Grimsditch, A. Kueny, C.M. Falco, and I.K. Schuller, Physical Review B, 1983. **27**: p. 7186.

60. T. Takahata, S. Araki, and T. Shinjo, Journal of Magnetic Materials, 1989. **82**: p. 287.

61. W. Vavra, C. H. Lee, F. J. Lamelas, H. He, R. Clarke, and C. Uher, Physical Review B, 1990. **42**: p. 4889.

62. S. Honda, T. Fujimoto, K. Koguma and M. Nawate, 2nd International Symposium on Metallic Multilayers, Abstract book, 1995: p. 253.

63. S. Honda, T. Fujimoto and M. Nawate, in Digest of 14th ICMFS/ e-MRS, August 1994, edited by E. Kisker and G. Bayreuther, 1994. **I**(482-483).

64. S. Honda, T. Fujimoto, and M. Nawate, Journal of Applied Physics, 1996. **80**(9): p. 5175.

65. K. Liu, K. Nagodawithana, P.C. Searson, and C.L. Chien, Physical Review B, 1995. **51**(11): p. 7381.

66. P. Beauvillain, P. Bruno, C. Chappert, C. Dupas, F. Trigui, E. Velu, and D. Renard, Journal of Physics (Paris) Colloq., 1988. **8**: p. 1703.

67. E. Velu, D. Dupas, W. Nabhan, F. Trigui, and J.P. Renard, Journal of Applied Physics, 1992. **71**(1): p. 503.

68. E. Kolb, M. Mulloy, C. Dupas, M. Galtier, D. Renard, J. P. Renard, F. Trigui, E. Velu, *ICMFS 94 Proceedings.* Journal of Magnetism and Magnetic Materials, 1995. **148**: p. 315.

69. E. Kolb, M.J. Walker, E. Velu, M.A. Howson, P. Veillet, D. Greig, J.P. Renard, C. Dupas, Journal of Magnetism and Magnetic Materials, 1996. **156**: p. 377.

70. J. Barnas, A. Fuss, R.E. Camley, P. Grunberg, W. zinn, Physical Review B, 1990. **42**(13): p. 8110.

71. S. Araki, T. Takahata, and T. Shinjo, *Journal of the Magnetism Society of Japan.* 1989. **13**: p. 339-342.

72. C. Chappert, P. Bruno, Journal of Applied Physics, 1988. **64**: p. 5736.

73. Hamberod, B. Dieny, J.Eymery, B. Gilles, J.M. Hartmann, A. Marty, and Edon, Journal De Physique IV, 1992. **C3**: p. 245.

74. S. Pizzini, F. Baudelet, E. Dartyge, A. Fontaine, Ch. Giorgetti, J.F. Bobo, M. Piecuch and C. Marliere, Journal of Magnetism and Magnetic Materials, 1993. **121**: p. 208-212.

75. M.J. Casanove, E. Snoeck, C. Penchenat, H. Ardhuin, R. Mamy, B. Raquet, M.D. Ortega, M. Goiran, A. R. Fert, and J. C. Ousset, Thin Solid Films, 1996. **275**: p. 129-132.

76. C. F. Majkrazak, *et al.*, Physical Review Letters, 1986. **56**: p. 2700.

77. S. S. P. Parkin, N. More, and K. P. Roche, Physical Review Letters, 1990. **64**: p. 2304.

78. S. S. Parkin, Physical Review Letters, 1991. **67**: p. 3598.

79. V. Bartenlian, P. Beauvillain, C. Chappert, C. Dupas, J. Ferre, M. Galtier, E. Kolb, M. Mulloy, J. P. Renard, and P. Veillet, Physical Review Letters, 1993. **71**(18): p. 3023.

80. P. Vruno, C. Chappert, Physical Review Letters, 1991. **67**: p. 1602.

81. S. S. P. Parkin, R. F. C. Farrow, R. F. Marks, A. Cebollada, G. R. Harp, and r. J. Savoy, Physical Review Letters, 1994. **72**(23): p. 3718.

82. Y. Roussigne, F. Ganot, C. Dugautier, P. Moch, and D. Renard, Physical Review Letters, 1995. **52**(1): p. 350.

83. J. Corno, M. Galtier, and D. Renard, Journal of Magnetism and Magnetic Materials, 1997. **174**: p. L10-L16.

84. V. Grolier, D. Renard, B. Bartenlian, P. Beauvillain, C. Chappert, C. Dupas, J. Ferre, M. Galtier, E. Kolb, M. Mulloy, J. P. Renard, P. Veillet, Physical Review Letters, 1993. **71**: p. 3023.

85. S. S. P. Parkin, Physical Review Letters, 1993. **71**: p. 1641.

86. A. Fert, I.A. Campbell, Journal of Physics, 1976. **F6**: p. 849.

87. I.-P. Renard, P. Bruno, R. Megy, B. Bartenlian, P. Beauvillain, C. Chappert, C. Dupas, D. Kolb, M. Mulloy, P. Veillet, and E. Velu, Physical Review B, 1995. **51**(18): p. 12821.

88. *Nanolithography - A Tool For The Production and Development Of NanoProducts*. 2004: The Institute of Nanotechnology.

89. T. E. Dinan, M. Matlosz, and D. Landolt, *Experimental Investigation of the Current Distribution on a Recessed Rotating Disk Electrode.* Journal of The Electrochemical Society, 1991. **138**(10): p. 2947.

90. Product Guide, JEOL JPS-9010 Photoelectron Spectrometers (XPS).

91. Q. Huang, E.J. Podlaha, Journal of The Electrochemical Society, 2004. **151**(2): p. C119-C126.

92. E. Chassaing, K. Vu Quang, and R. Wiart, Journal of Applied Electrochemistry, 1987. **17**: p. 1267-1280.

93. Mordechay Schlesinger, Milan Paunovic, *Modern Electroplating*. 2000. p. 35.

94. C.C.Lo, J.A.Augis, M.R. Pinnel, Journal of Applied Physics, 1979. **50**(6887).

95. F.B. Koch, Y. Okinaka, C. Wolowodiuk and D.R. Blessington, Plating, 1980. **67**(7): p. 43.

96. R. G. Craig, ed. Restorative Dental Materials. 9th ed., St. Louis:C. V. Mosby, 1993.

97. H. H. Chandler, R. L. Bowen, G. C. Paffenbarger, *Physical properties of a radiopaque denture base material.* Journal of Biomedical Materials Research, 1971. **5**(4): p. 335-357.

98. Q. Huang, D. Davis, and E. J. Podlaha, *Electrodeposition of FeCoNiCu Nanowires.* To be submitted to Journal of Applied Electrochemistry, 2004.

99. A. Blondel, J. P. Meier, B. Doudin and J. Ph. Ansermet, K. Attenborough, P. Evans, R. Hart, G. Nabiyouni and W. Schwarzacher, Journal of Magnetism and Magnetic Materials, 1995. **148**: p. 317.

VITA

Mr. Maoshi Guan was born in Shandong Province, People's Republic of China, in 1977. He was enrolled in University of Petroleum (East China) in 1995 and obtained the degree of Bachelor of Science in chemical engineering in 1999. In 2002, he came to Louisiana State University to pursue his master degree in chemical engineering, which will be conferred in May 2004.